Title
Advanced Image Sensing Methods for Traffic Surveillance and Detection

Author
MacCarley, Art

Publication Date
1999-03-01

CALIFORNIA PATH PROGRAM
INSTITUTE OF TRANSPORTATION STUDIES
UNIVERSITY OF CALIFORNIA, BERKELEY

Advanced Image Sensing Methods for Traffic Surveillance and Detection

Art MacCarley
California Polytechnic State University San Luis Obispo

California PATH Research Report
UCB-ITS-PRR-99-11

This work was performed as part of the California PATH Program of the University of California, in cooperation with the State of California Business, Transportation, and Housing Agency, Department of Transportation; and the United States Department of Transportation, Federal Highway Administration.

Report for MOU 211

March 1999

ISSN 1055-1425

PATH
California Partners for Advanced Transit and Highways

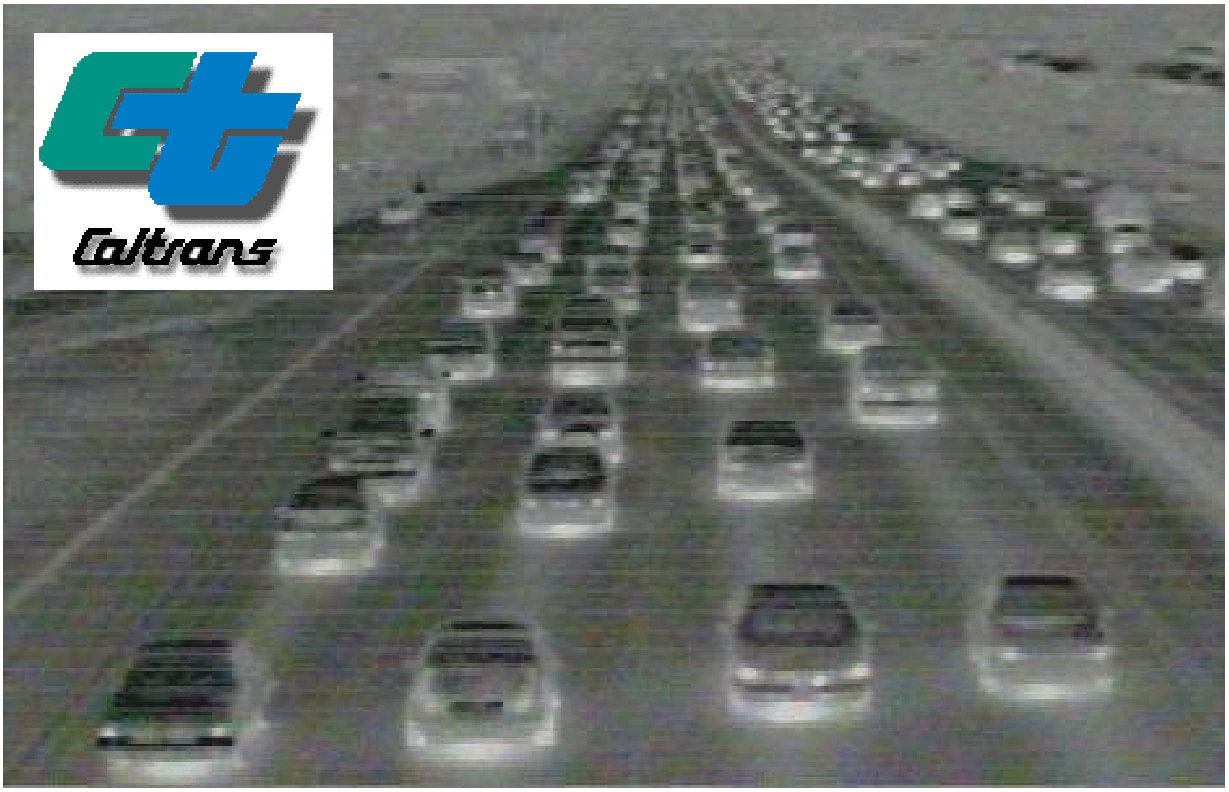

Final Report

Advanced Image Sensing Methods for Traffic Surveillance and Detection

Prepared for California PATH and the California Department of Transportation
by the Transportation Electronics Laboratory, Dept. of Electrical Engineering
California Polytechnic State University, San Luis Obispo, California
Caltrans/PATH MOU 211, Cal Poly Foundation Project Nos. 5916, 5859.
Document No. TEL5859F98
Revision History: June 30, 1998 (Rev 1), Novermber 13, 1998 (Rev 2).

Table of Contents

1 Abstract

This report describes the results of a PATH-funded study conducted by the Cal Poly Transportation Electronics Laboratory intended to assess advanced imaging technologies for potential application to roadway surveillance and detection. A major motivation for this study was the possibility of improved visibility under conditions of fog or dust using wavelengths longer than that of the visible spectral band. Technologies considered included ten types of infrared video cameras and one millimeter-wave still-frame imaging system. Evaluation criteria were structured to reflect the surveillance needs of traffic management center personnel and information needs of computer vision systems. The various imaging technologies are described in detail, and intrinsic merits and limitations of each are discussed. Field work is described in which video samples were acquired using each imaging technology. A pair of metrics of image information were developed and applied using computer image analysis to image sequences produced by each technology. Evaluation with respect to these metrics indicated that all of the advanced imaging technologies assessed generally provided less useful image information than conventional color CCD video cameras, except under conditions of very dense fog, in which some types of infrared imaging provided slightly more usable information. Overall conclusions were that advanced imaging methods appear to be justified only for selected roadway situations, such as recurrent fog in combination with hazardous traffic patterns.

Keywords: Video, detection, sensing, infrared, millimeter-wave, sensor, computer vision, image processing, traffic monitoring, transportation electronics, advanced traffic management, surveillance, monitoring, object identification.

2 Executive Summary

Existing electronic imaging methods utilize conventional video cameras, and rely on human perception of information in the visible 400-700 nanometer (nm) electromagnetic spectrum. This is adequate for most highway surveillance applications. A Traffic Management Center (TMC) operator may rely upon these video images for visually monitoring traffic conditions, or these video signals may be used by a computer vision system to detect traffic flow parameters.

Exceptions exist however: reasonably clear atmospheric conditions and an adequate level of natural or artificial visible-spectrum illumination are required. In conditions of dense fog, snow, rain or airborne particulates (smoke or dust), and at times of low natural illumination, visible light sensing methods may be inadequate. Yet, it is precisely in these low-visibility conditions that the greatest need exists for reliable traffic monitoring, especially if the objective is the recognition of impending dangerous traffic situations. Such special cases might include hazardous traffic patterns or detection of vehicles being operated unsafely in dense fog or at night. In addition, the information content of an image formed for radiation outside the visible spectrum is fundamentally different. Depending of the need, this information may be either superfluous or of significant value to a human or machine observer.

This project studies alternative imaging technologies for traffic surveillance and detection which have superior ability to "see through" fog and particulates, which do not depend on natural visible-spectrum illumination, and which may contain additional information of potential value in traffic management. The most probable candidates are infrared (IR) sensitive cameras and passive millimeter-wave radiometric imaging. While commercial product offerings for each of these technologies may be expensive at the present time, recent advances are expected to reduce system costs, possibly to the point of cost-effectiveness in specialized monitoring situations.

State-of-the-art examples of these alternative imaging technologies are evaluated in the context of traffic surveillance and detection applications. Evaluation criteria include: information content of image, standard video performance metrics, technical advantages and limitations, and human interface factors. Extensive field test data is acquired over a range of traffic and environmental conditions. A suite of metrics are developed for objective comparison of the image information content of traffic imagery acquired with each device. A suite of computer vision applications were developed and used to compare all videotaped or digitally-stored imagery from field work using these metrics. Results were ranked based upon spectral band, scene conditions, and individual camera.

Sensor fusion opportunities are identified based upon experience gained with each advanced imaging technology. The merits and limitations of advanced imaging sensors as inputs to traffic detection computer vision systems are discussed. Recommendations are made regarding the usability and cost effectiveness of these technologies for a range of traffic surveillance and detection applications.

3 Acknowledgements

The work was performed as part of the California PATH program of the University of California, in cooperation with the State of California Business, Transportation, and Housing Agency, Department of Transportation. This report was written by the project director C. Arthur MacCarley, with substantial contributions by consultant Lawrence A. Klein and research associate Brian Hemme.

The author wished to acknowledge the guidance and direction of the contract monitor, Robert Tam of PATH / U.C. Berkeley. Among the many research assistants that contributed to this work were Brian Hemme, Arash Behziz, Robert Fingerson, Sean Norris, Leonard Ponce, Adam Lang, Todd Eidson, Fingerson, Jan Nimick, Bryan Gray and Phillip Ng. Technical advice was provided by Joseph Palen of the California Department of Transportation, New Technology Division, and numerous colleagues working in the fields of atmospheric physics, advanced sensors, and infrared imaging systems. Lawrence Klein contributed much of the background material for this report. All computer image analysis programs were coded in Borland Builder Visual C++ by Brian Hemme.

4 Disclaimer

The statements and conclusions of this report are those of the authors, and not necessarily those of the State of California or the California Department of Transportation. The results described in this document are based solely upon tests conducted by the Cal Poly Transportation Electronics Laboratory, with the support of the California Department of Transportation and California PATH. This report does not constitute a standard, regulation or specification. The mention of commercial products, their sources, or their use in connection with materials reported herein is not to be construed as an actual or implied endorsement of such products.

5 Background

Improved management of traffic is necessary for alleviating present and future congestion and safety problems on U.S. highways. Remote traffic surveillance is an important component of operational strategies to improve the management of roadways. Video cameras are already in use in many locations, and have proven their value in monitoring of traffic flow for data collection, traffic management and incident detection. Video surveillance can serve as a valuable aid to human traffic control operators, extending their effectiveness in traffic monitoring and management tasks. Advanced computer vision methods may also be employed, in which computers monitor the traffic scenes, recording traffic data continuously, and alerting operators of situations requiring their attention only when necessary.

Over 30 million motor vehicles are registered in California. Traffic congestion and increased risk of traffic accidents have become accepted facts for users of California freeways. Caltrans has responded by using traffic management to improve the efficiency and safety of California highways. Within the next few years, existing and planned Traffic Operation Centers (TOCs) will be expected to monitor and manage an increasing level of traffic flow and congestion on California freeways and highways. The task of monitoring hundreds of miles of multi-lane roadways, to the extent necessary for effective flow management, is a formidable one.

It can be stated that "the better the information, the better the management". Previously, the primary sources of information available to traffic controllers in the TMC were provided by in-roadway inductive loop vehicle detectors, reports by law enforcement and Caltrans field personnel, and by driver phone calls. It is generally recognized that these sources of information alone do not provide the necessary level of information for the implementation of advanced traffic management strategies and rapid incident responses.

The increased deployment of video cameras at strategic locations along the freeway or highway network is expected to improve both the accuracy and immediacy of the traffic data available to TMC personnel. Intelligent management actions may then be engaged without the lag time associated with verbally reported data or the uncertainty associated with loop detector data. Possible actions include ramp meter rate control, driver advisement on Changeable Message Signs (CMS), and rapid deployment of emergency crews in response to traffic accidents or potential traffic hazards. Long-term data collection in support of improvements in management strategies is also enhanced. It is also possible to classify vehicles, monitor infrequently occurring events, and provide historical traffic data.
Conventional video cameras, utilizing visible spectrum radiation for image formation, are adequate in most traffic surveillance situations. However, special situations may exist that warrant more sophisticated image sensing technologies. Under conditions of limited visibility due to fog, rain, dust, smoke or glare, conventional video cameras provide little or no information. In darkness, only the headlight or tail light spots of vehicles are detectable. In the infrared and millimeter-wave bands, solar or artificial illumination is not required for visibility. Blackbody radiation alone provides “self-illumination” of vehicles on highways, especially when hot surfaces such as the engine or exhaust are exposed. Heat radiation from certain surfaces of commercial vehicles is indicative of possible equipment violations or overload conditions. Automatic detection of hazardous traffic situations at night by advanced computer vision and image understanding methods requires that the image clearly shows the entire shape of vehicles, not just the headlights. Infrared or millimeter-wave images have this potential, whereas visible spectrum images do not. Automated enforcement of High Occupancy Vehicle lanes and right-of-ways may best utilize non-visible spectrum image information. Image data fusion, in which synthetic images formed and analyzed in real time from sensors operating in multiple spectral bands, may provide the ultimate information for traffic management decision-making.

The ability of radiation outside the visible spectrum to penetrate the atmosphere under conditions that would obscure normal visibility is of particular interest for traffic safety. The dangerous combination of limited visibility and hazardous traffic patterns have accounted for many of the most serious highway accidents in recent years.

Almost nowhere in the nation are highways equipped to help drivers in fog or other blinding conditions. A few programs have been tried, such as warning signs and a variable speed limit relative to road conditions. There are no objective criteria for closing a road. According to CHP officers, "You have a real problem closing a freeway in this state unless something happens to warrant a closing". Traffic control and law enforcement rarely have sufficient information to justify such radical control actions. More information is needed in real-time conditions.

Various warning systems have been studied but their effectiveness has been limited by the nature of fog and dust storms. From a practical perspective, the existence of a limited visibility condition alone is insufficient to warrant radical corrective action. Travelers need to reach their destinations. However, intelligent detection of situations involving both limited visibility and dense or erratic traffic patterns may target the highest risk situations, allowing more efficient traffic management actions. We conclude that effective detection of visibility-related hazards requires the ability to detect the presence of the visibility condition, while retaining the ability to see complete vehicles in the traffic flow.

Advanced image sensing methods utilize areas of the electromagnetic spectrum outside of the visible (0.4 to 0.7µm) range, or they utilize additional information in the visible range (e.g., color information). Outside the visible spectrum, imaging methods have been demonstrated in the IR (1.5 to 20 μm) range, or in the microwave or millimeter-wave (35 to 94 GHz) range. IR imaging has been used for many specialized applications in military, mechanical engineering, satellite mapping, and energy efficiency testing. Millimeter-wave radiometric imaging has also been used in military and space applications. Of particular interest is the ability of these methods to "see through" fog, rain, snow, and dust to a greater extent than visible spectrum cameras. This capability motivates the investigation of these imaging methods for monitoring sections of highways particularly prone to visibility-related accidents.

6 Visibility and Traffic Safety

6.1 Phenomenology of Fog

Fog can be described as a cloud of small water droplets near ground level that is sufficiently dense to reduce horizontal visibility to less than 1,000 m (3,281ft). The word fog is also used to refer to clouds of smoke particles, ice particles, or mixtures of these components. Under similar conditions, but with visibility greater than 1,000 m, the phenomenon is termed a mist or haze, depending on whether water drops or solid particles cause the obscurity.

Fog is formed by the condensation of water vapor on condensation nuclei that are always present in natural air. This results as soon as the relative humidity of the air exceeds saturation by a fraction of 1 percent. In highly polluted air the nuclei may grow sufficiently to cause fog at humidities of 95 percent or less. Growth of the drops may be helped by the absorption of certain soluble gases, notably sulfur dioxide to form dilute sulfuric acid. Three processes can increase the relative humidity of the air: cooling of the air by adiabatic expansion; mixing two humid air streams having different temperatures; and direct cooling of the air by radiation.

The first process, adiabatic expansion, is responsible for the formation of clouds and plays a part in the formation of upslope fogs that are formed by the forced ascent of humid air up the sides of hills and mountains. The second process, mixing, is manifest when air that has been in contact with a wet ground or water surface having a different temperature from that of the air above is mixed with the dryer air from above.

The most stable fogs occur when the surface is colder than the air above, that is, in the presence of a temperature inversion. Fogs also can occur when cold air moves over a warm, wet surface and becomes saturated by the evaporation of moisture from the underlying surface. Convection currents, however, tend to carry the fog upward as it forms, and it appears to rise as steam or smoke from the wet surface. This is the explanation of steam fogs that are produced when cold Arctic air moves over lakes, streams, inlets of the sea, or newly formed openings in the pack ice; hence, the term Arctic sea smoke.

Fogs found over land are of two types, advective fog (formed by cool air passing over a colder surface) typical of coastal regions, and radiative fog (formed by radiative cooling of the earth’s surface below its dew point level) found in inland regions. Advective fogs contain a greater number of large water drops and generally higher liquid water content than radiative fogs [1]. When the size of a particle in fog, cloud, rain, dust, etc. is comparable to the wavelength of the incident energy, the phase of the wave is not uniform over the particle. These phase differences give rise to the observed scattering of energy.

Advection fog is formed by the slow passage of relatively warm, moist, stable air over a colder wet surface. It is common at sea whenever cold and warm ocean currents are in close proximity and may affect adjacent coasts. A good example is provided by the frequent dense fogs formed off the Grand Banks of Newfoundland in summer, when winds from the warm Gulf Stream blow over the cold Labrador Current. It also may occur over land, especially in winter when warm air blows over frozen or snow-covered ground. Advection fogs occur most readily with winds of about 5 m/s (10 mi/h), sufficiently light to maintain a temperature contrast between air and surface and not strong enough to produce turbulent mixing through a considerable depth of the atmosphere. Typical advection fogs extend up to heights of a few hundred meters and sometimes also occur together with radiation fogs.

Radiation fog forms over land on calm, clear nights when loss of heat by radiation cools the ground and chills the air in the lowest few meters to below the dew-point temperature. Once dense fog has formed, the top of the fog replaces the ground as the effective surface cooled by radiation, and the fog increases progressively in depth as long as there is sufficiently moist air above it. The development of a strong temperature inversion tends to stabilize the fog and suppress air motions, but slow, turbulent stirring motions usually are present and probably are important in maintaining the fog. They do so by replacing the air in the lowest layers, that is losing moisture by deposition on the ground, with more moist air from above. Typical inland radiation fogs reach to heights of 100 to 200 m.

Golding studied the influence of terrain and local winds on fog formation using a mesoscale numerical weather prediction model to simulate the development of fog at Perth, Australia [2]. The key aspects of his fog modeling were the need to parameterize vertical diffusion, incorporate longwave radiation, and incorporate shortwave radiation effects. The phenomena addressed in the fog development process noted that fog is produced after passage of a cold front or of a coastal trough and is almost always associated with a light southwesterly wind and high humidity. These conditions restrict downward turbulent transport of moisture. In valley situations, the development of nocturnal wind systems may have a considerable impact on radiation fog formulation. The importance of the local wind circulation in the simulations raises questions about radiation fog formation mechanisms in other areas that cannot be answered in the present study. It is well known that radiation fog often forms in hollows and that this is usually attributed to the presence of additional moisture or cooler air from drainage effects.

Inversion fogs are formed as a result of a downward extension of a layer of stratus cloud, situated under the base of a low-level temperature inversion. They are particularly prevalent off western coasts in tropical regions during the summer, when the prevailing winds blow toward the Equator and cause the upwelling of cold water along the coast. Air that passes over the cold water becomes chilled, its relative humidity rises, and it becomes trapped under the inversion. Subsequent nocturnal cooling may then cause a stratus layer to form and build down to the ground to form an inversion fog.

Frontal fog forms near a front when raindrops, falling from relatively warm air above a frontal surface, evaporate into cooler air close to the Earth's surface and cause it to become saturated.

When the air temperature falls below 0^{o}C (32^{o}F) the fog droplets become supercooled. At temperatures between 0 and -10^{o}C (32 and 14^{o}F), only a small proportion of the droplets freeze, and the fog is composed mainly or entirely of liquid water. However, at lower temperatures more and more droplets freeze, so that below about -35^{o}C (-31^{o}F) and certainly below -40^{o}C (-40^{o}F), the fog is composed entirely of ice crystals. The visibility in an ice fog is often considerably worse than that in a water fog containing the same concentration of condensed water.

Although it is convenient to classify fogs according to the physical processes that produce saturation of the air, it is difficult to apply such a schema. For example, multiple processes can act at the same time to produce a fog. The relative importance of each process varies from case to case and with time. Probably no two fogs are controlled by exactly the same combination of factors, a fact that makes forecasting the formation and dispersal of fog difficult.

In most areas subject to fog, the frequency and persistence of the fogs show a marked seasonal dependence. Conditions favorable to the formation of radiation fog, namely, clear skies and light winds, often occur in the central regions of anticyclones (see anticyclone) and ridges of high pressure, so that the advantages of dry, settled weather are often nullified by the occurrence of fog, especially in autumn and winter. Advection fog may occur in any season of the year and at any time of day or night and is not restricted to conditions of light winds and clear skies. Over land it is especially liable to occur in winter, when mild, damp air flows over a frozen or snow-covered surface. Over the coastal waters of the British Isles, it occurs chiefly in late spring and early summer when the sea is still cold.

Dense fog presents one of the greatest hazards to aviation and to nearly all forms of surface transportation. Modern aircraft generally are not allowed to take off or land if the visibility along the runway is less than 600 m. In many countries, especially those in temperate latitudes, fog causes widespread dislocation and delay in transportation systems on several days each year.

6.2 Rain and Drizzle

Drizzle consists of very small, numerous water drops that may appear to float while being carried by air currents; drizzle drops generally have diameters between about 0.2 and 0.5 millimeter (0.008 and 0.02 inch). Smaller ones are usually cloud or fog droplets, while larger drops are called raindrops. Drizzle often is accompanied by fog but differs from it because drizzle drops fall to the ground. Drizzle commonly falls from stratus clouds.

6.3 Prior Studies

A report prepared by F. D. Shepard [3] in 1996 documents the findings of a National Cooperative Highway Research Project performed by the Transportation Research Board to review the existing knowledge and practices used to manage traffic in the reduced visibility conditions found in fog. The project focused on the following three objectives:

1. meteorology of fog forecasting and detection,
2. state of knowledge regarding driver perception and behavior in fog, and
3. current state of fog countermeasures, including evaluations of those countermeasures for which information is available, along with a review of practices that have proved unsuccessful.

With respect to Objective 3, countermeasures implemented in California, Louisiana, South Carolina, New Jersey, New Mexico, England, and the Netherlands were reviewed.

Table 6.1 shows the international classification of visibility on fogs. Thick fog is more prevalent in coastal areas in the U.S. than in the center of the continent. Predicting fog can be very difficult because it can vary in density and location, move from on location to another (horizontally or vertically), develop or dissipate quickly, and encompass small or large areas.

Table 6.1 International Classification of Visibility.

Visibility	Description
Less than 40 m	Dense fog
40 - 200 m	Thick fog
200 - 1000 m	Fog
1 - 2 km	Mist (if mainly due to water droplets) Haze (if mainly due to smoke or dust)
2 - 4 km	Poor visibility
4 - 10 km	Moderate visibility
10 - 40 km	Good visibility
Over 40 km	Excellent visibility

Advective fogs occur primarily during the summer mornings along the California coast. Coastal fogs are produced when moist air is blown landward over an area of coastal upwelling. Upwelling is the process where cold, deep ocean water wells upward to replace surface water that has been driven offshore. The fog is blown onshore by NW winds that are lightest in the early morning hours and strongest in the afternoon hours. The afternoon hours correspond to the time of greatest temperature gradient between the coast and interior. To determine where the water in the coastal fog was originating, a study was performed to collect fog, rain, and groundwater for stable isotropic analysis on the Point Reyes Peninsula in California [4]. The study of the isotope concentrations in the water samples allowed the origins of fog water to be studied and provided a way to trace fog water through the hydrosphere.

6.4 Fog Sensors

Three types of fog sensors are presently available: transmissometers, backscatter sensors, and forward-scatter sensors.

A transmissometer contains a projector that transmits a known amount of light toward a detector usually set at a distance of 152 m (500 ft) from the projector. Primarily used at airports, these instruments are costly, heavy, and require a long and accurate alignment of projector and receiver.

With the backscatter sensor, the light source and receiver are pointed in the same direction and positioned so that the amount of light scattered back is measured. A large amount of backscatter indicates dense fog. A disadvantage of this device is the variation in the amount and direction of backscattered light (a function of the size of the scattering particles).

The forward-scatter sensor has a projector that transmits a beam of light. The amount of light scattered forward into a receiver is measured. This sensor is competitive in accuracy, reliability, and cost with the other types of sensors. Its compact size and light weight make it relatively easy to mount and it is fast becoming the predominant type of fog sensor.

During the winter of 1972-1973, Caltrans conducted a field test to evaluate the performance of the three types of fog warning sensors [5, 6]. Four sensors were selected, as shown in Table 6.2, and were connected to a changeable message sign on State Route 99 in San Joaquin County between Arch Road and Austin Road, a distance of 9.7 miles.

Table 6.2 Detectors Used in Caltrans Winter 1972-1973 Fog Detection Study (Operation Fogbound).

Characteristic	**Meteorology Research Fog Visometer[1] (Forward, side, and backscatter)**	**Kahl Scientific Videograph (Backscatter)**	**AeroVironment Model 150 (prototype) Highway Fog Monitor[2] (Forward scatter)**	**Lear Siegler SM4 (Transmissometer)**	
				Sender/Receiver	**Projector**
Visibility range	260 ft to 20,000 ft or 100 ft to 10,000 ft standard. Option to measure as low as 50 ft and 25 ft.	0.06 mi (316 ft) to 6 mi. At lower visibilities, readings are in increments of 100 ft since the Videograph is graduated in 0.05 mi. Above 0.20 mi visibility, graduations are in 0.1 mi increments.	At least 1000 ft	0.05 km (160 ft) to 5 km (16,000 ft)	*
Output signal	0 to 30 V	---	---	0-20 mA dc	Not applicable
Base	---	---	---	Large with rigid foundation	Large with rigid foundation
Calibration	---	---	---	Uses clear day conditions	Not applicable

[1] Measures scattering coefficient.
[2] Malfunctioned during test, but could not be replaced by manufacturer as this was the only prototype available.
* Baseline between sender/receiver and projector is 37 m. Device is not precise when visibility < 300 ft.

Two automatic fog detectors that were not tested, but show potential, were also mentioned [5, 6]. The first is a closed circuit television (CCTV) directed toward targets located at incremental distances along the roadway. The number of visible targets determines the existing visibility. The second is a small-sized backscatter device whose greatest dimension is of the order of 6 to 8 inches so that it can be mounted on a guard-rail post. Operated by a battery (that with present technology can be recharged through solar energy), it emits a low intensity light that is backscattered into the receiver portion of the instrument.

The SM4 transmissometer detector was made available by Lear Siegler of Colorado. The Fog Visiometer measures forward, sideward, and backscattered light and is manufactured by Meteorology Research, Inc. The Videograph measures backscattered light and is manufactured by Kahl Scientific. This device was not installed on the highway because it was only able to measure visibility over a minimum distance of 316 ft, whereas the requirement for a highway fog detector was a minimum range of 50 ft to a maximum range of 1000 ft with an accuracy of ±25 ft. Caltrans standards equate a ±25-ft change in visibility with a change in safe driving speed of ±3 mi/h on wet pavement in the 30 to 60 mi/h range. The Highway Fog Monitor measures forward scatter and is manufactured by AeroVironment, Inc. A CMS located alongside the road was used to notify drivers of fog conditions ahead. When the visibility dropped to 300 ft, the message "DENSE FOG AHEAD" was displayed.

The study found:

- The location and size of the sign (13-inch letters except the words "WRECK" and "FOG" which were 26 inches) were not effective enough to catch the attention of the driver. Signs should be placed on overhead structures or at more remote locations where other signs or highway features are not competing.
- There was no evidence that speed was reduced in the control zones while the signs were operating and warning of heavy fog ahead.
- In a permanent location, consideration should be given to using a microwave interconnect between sign and fog detector as telephone lines were too costly. (Current spread spectrum radio technology is another alternative.)
- A speed advisory system to warn drivers of the speeds of other vehicles that are beyond the driver's sight distance. These advisories could warn drivers of congestion and stoppages ahead.
- With any type of sensor, maintenance is critical and should be performed on a regular basis, especially at the beginning of the fog season.

6.5 Driver Behavior Under Reduced Visibility Conditions

A 1967 California study experimenting with variable speed signs found the following:

- Mean and 85th percentile speeds were reduced as much as 8 to 13 km/h (5 to 8 mi/h). Exceptions were noted for high-volume daytime and low-volume nighttime freeway operations, where very small reductions were noted.
- Generally, variability in speed was not reduced.
- Posted speeds on expressways caused further reductions in mean and 85th percentile speeds and also reduced speed variability. These reductions were not found for freeways.
- Posted speeds of less than 55 to 65 km/h (35 to 40 mi/h) has little additional effect in reducing speeds.
- Headways were not affected by fog or posted speeds.

Studies conducted in California in the 1960s found that at low posted speeds in very dense fog on freeways, there was an increase in variance of speeds between vehicles. Apparently, some drivers believed the reduced speed limit was warranted and slowed down, while others did not. The probability of accidents increased because one group of drivers slowed relative to the others. The drivers who did slow down did not reduce speed to the posted value. It was speculated that the drivers may discredit a warning sign that advises a speed significantly lower than that posted [3].

A 1978 Oregon research project used a test facility to make fog and derived the following findings:

- When a single advisory sign was posted well in advance of the fog zone, there was a noticeable change in flow stability and vehicle speeds. In general, the speed sign appeared to smooth out the mean speed by making the deceleration start earlier and become more gradual.
- The lower visibility condition resulted in lower speeds.
- The addition of a posted speed generally caused larger speed variation
- There was an optimum posted speed for producing the smoothest traffic flow for each visibility condition
- Signing was important both in advance of the fog and in the fog zone
- After a number of exposures to false or unrealistic information given by a system, drivers would no longer respond to the system
- Questionnaires revealed that:
    - 46 percent of the drivers preferred to follow another vehicle in fog
    - 29 percent preferred to follow pavement stripes whenever possible
    - 5 percent said they would pull off the road and stop in dense fog.

A 1979 Oregon study indicated that the use of a variable message warning sign on a fog-prone interstate did not necessarily lead to a decrease in speeds when the posted speed was lowered. Accident data did, however, indicate that the system substantially increased safety during periods of reduced visibility by reducing the number and severity of fog-related accidents [3].

Research in Virginia in 1977 investigated use of pavement inset lights during fog for improved motorist guidance. The following observations were noted:

- There was an increase in nighttime speeds and a decrease in daytime speeds after installation of the inset lights
- The lights caused an increase in speed variability for cars
- For all conditions before and after installation of the lights, the actual sight distances were less than the safe stopping distances
- Nighttime headways increased after the lights were installed.

These changes in traffic flow could be construed as producing an increase in the potential for accidents, while safety might be enhanced by the improved delineation the lights provided [3].

A presentation made by Rockwell to the National Transportation Safety Board in 1991 [3] noted that driver problems in fog included the following:

- restricted visibility
- speed election beyond available visibility
- drivers gain lateral tracking cues at the expense of close car following
- over response to velocity perturbations
- indecision in lane placement, speed election, whether to leave the roadway, and use of lights and hazard lights
- inability of driver to see far enough ahead to anticipate braking by lead car.

These situations produced drivers with different elected speeds and very short headways in fog leading to flow instability and accident-related problems. Rockwell also noted that signing research showed that a driver spends anywhere from 0.8 to 2.0 seconds to read a sign. In extreme cases, this does not allow a driver the desired response time. Therefore, a conclusion was reached that *signing must be paced prior to a known foggy area and not in it*.

March 20, 1992 - One person was killed and 64 were injured in an accident on Interstate 15 at Cajon Pass in the San Bernardino Mountains. One hundred vehicles were involved in a chain reaction accident in a heavy rain and fog condition. Visibility was reduced to 20 feet in some areas.

November 29, 1991 - 17 people were killed and 150 were injured in a 104-vehicle accident on Interstate 5 near Coalinga, about 160 miles southeast of San Francisco. A blinding dust storm was blamed.

December 11, 1990 - In a fog-related incident on I-75 near Calhoun, Tennessee on Dec. 11, 1990, visibility was reduced from several miles to a few feet within minutes in dense fog. Five minutes later, the first of 27 separate accidents occurred. Within 15 to 20 minutes, 99 vehicles collided in both the northbound and southbound lanes. Thirteen people were killed and at least 51 others required hospitalization. Investigators determined the accident was probably caused by drivers operating their vehicles at significantly varying speeds following sudden loss of visibility. A questionnaire survey of the drivers involved in the accident revealed that 18 estimated their speeds to have been between 24 and 81 km/h (15 and 50 mi/h) entering the fog, while 37 said theirs had been between 89 and 113 km/h (55 and 70 mi/h). The NTSB noted that the multiple-vehicle, rear-end collisions involved slowed or stopped vehicles. They also noted that the presence of light fog and fog warning signs should have been distinct clues to dense fog and hazardous driving conditions ahead. In short, some drivers slowed for the light fog, some slowed for the dense fog, some slowed only when they encountered vehicles that had slowed or stopped, and others never slowed and consequently collided with vehicles that did slow or stop. These actions lead the NTSB to question the credibility of warning signs. They recommended that the signs reflect actual conditions that would produce more uniform driver response and thus reduce variations in speed [7].

December 30, 1988 - Six people were killed and 18 were injured in a 23-car accident on Interstate 74 about 1,320 miles south of Chicago. Fog was blamed for the accident.

September 12, 1989 - Three people were killed and 12 were injured in a 15-car accident on Interstate 80 at Soda Springs, California. A hailstorm was blamed for the accident.

Over the last decade, close to 7,000 people have died in such accidents. The National Transportation Safety Board has sent investigators to these accident sites looking for common elements in the very uneven reactions of drivers to conditions of reduced visibility.

In a report prepared for Governor Wilson by the California Highway Patrol (CHP), Office of Emergency (OES) and Caltrans following the I-5 incident November 29, 1991, the relationship between visibility conditions and collision risk was addressed:

- Should I-5 have been closed before the collisions? CHP on the scene concluded that conditions did not exist to require closure.

- Did motorists have adequate information about road conditions? Yes, "...they had already driven through areas with blowing dust".

- Did motorists respond appropriately to reduced visibility conditions? Not entirely - some didn't reduce speed adequately.

In this and similar multi-car accidents, two factors were present: limited, but not necessarily blocked visibility, and erratic or otherwise potentially hazardous traffic patterns.

On March 20, 1995, in another fog-produced accident, 193 cars, trucks, and other vehicles collided over 12 minutes, as visibility dropped to between 20 and 30 feet along a two-mile stretch of the seven-mile bridge that spans Mobile Bay in Mobile, AL [8]. The first emergency call was received at 6:37 a.m. as the morning commute was getting underway.

In research in the Netherlands, measurements were made comparing actual visibility range against perceived range and against traffic speeds. Visibility ranges as low as 150 m (490 ft) were hardly reflected in the traffic speeds. At ranges between 50 and 150 m (160 to 490 ft) speeds decreased, but not to low enough levels. The researchers reasoned that the environment misleads drivers. In fog, the drivers' brains translate the vagueness as "far away." Thus the drivers felt they were driving slower than they were and any advice to drive slowly still lead to speeds that were too high. It was also noted that only with severe speed differences and traffic jams is there a real danger of severe accidents. If a message warning drivers of fog five miles ahead were given, it should be repeated every mile because drivers have difficulty estimating distances and may forget that they had seen the message to begin with (a message loses its effect in about a minute). One of the primary conclusions was that the solution was to detect traffic jams and slow traffic down. Once police were on site warning traffic to slow down, secondary accidents practically disappeared [3].

Additional results from the traffic flow in fog research conducted in the Netherlands were presented at the 1997 TRB meeting [9]. The data were obtained using an automatic fog signaling system composed of 20 sensors that were installed over a 10 km section to measure visibility range on the A16 freeway near Breda in the Netherlands. In November 1990, before the system was installed, there had been an accident that claimed 8 fatalities, 27 injured, and over 100 vehicles involved because of the occurrence of a fog bank. The A16 is a dual roadway, two-lane freeway in each direction with a relatively high proportion of heavy traffic (20 to 30%) and high traffic volumes of about 75,000 vehicles per day. The legal speed limit is 100 km/h.

There are 37 outstations on the experimental road section. The outstations are linked to matrix signs located at intervals of 700 to 800 m. In dense fog, they display a speed limit of 80 or 60 km/h. The 20 visibility sensors measure the visibility distance every minute. Each outstation has 1, 2, or 3 sensors assigned to it to measure visibility distance near or downstream of the outstation. The speed limit for each outstation is determined from the lowest visibility measurement from the sensors assigned to it according to the following rules:

visibility distance > 140 m	no speed limit shown (blank)
visibility distance between 70 and 140 m	80 km/h speed limit
visibility distance < 70 m	60 km/h speed limit

Later the capability was added to modify the posted speeds using information produced by an automatic incident detection system that was related to the traffic speed in the absence of fog.

The visibility sensors were named Present Weather Sensors and they measured the extinction coefficient in the visible spectrum. The extinction coefficient was converted into the visibility distance in meters by dividing 3 by the extinction coefficient [9].

During fog conditions, the system displayed a message on overhead matrix signs along with a maximum speed limit that depended on visibility. The evaluation of the system was made over a two-year period. On top of reduced mean speed due to visibility reductions detected by the driver, the sensor system produced an 8 to 10 km/h additional speed decrease. Other measures of driving behavior, such as following distance, time headway, and time-to-collision, showed small or no effects. When a model for the reduction of accidents with decreased mean speed is used [10], a reduction in speed of 5 km/h forecasts a reduction in accidents of approximately 15%.

One anomaly observed was that in extremely dense fog (visibility range < 35 m), the sensor system appeared to have an adverse effect on speed. Under these circumstances, without the system present, drivers reduced their speed to less than the 60 km/h that would have been displayed by the system. The general effect of the system in this case was to shift the speed toward the indicated limit. However, these visibility conditions were extremely rare during the test period, occurring less than 0.07% of the time on one or more sensors.

The standard deviation of speeds within a lane decreased somewhat due to the system, but this was deemed a minor effect. The difference in the mean speed between the two lanes decreased when the system was present. Therefore, a more uniform speed was obtained on the entire roadway.

The results of a Wyoming study published in 1992 indicated that during the preceding five years, 61.1% of the total yearly accidents on I-80 between Laramie and Cheyenne occurred during the relatively short time (9.8%) that the road and travel conditions were poor [11]. The existing remote weather information system (RWIS) data did not correlate well with the road conditions reported by road users or snow-plow operators. Wyoming currently maintains 26 RWIS, with plans to install 26 more when funds become available [12]. RWIS is also used in California, Florida, and South Carolina. The precipitation sensor on RWIS was used to assess visibility. Visibility was classified as poor if less than 600 feet (183 m) of sight distance was present.

An average speed model was developed [11] to reflect the observed driver speeds on I-80. It is based on visibility, pavement condition (favorable: dry or wet, slick in spots; poor: slushy, snow-packed, icy), wind (favorable: calm or poor: strong and gusty):

$$\text{Average speed} = 62.5083 - 8.9833\, V + 7.4583\, V\, W - 4.7417\, P, \qquad (6.1)$$

where

V = visibility (0 = favorable, 1 = poor)

W = wind (0 = favorable, 1 = poor)

P = pavement (0 = favorable, 1 = slick in spots, 2 = poor)

Summary - The above studies and opinions relative to driver behavior under reduced visibility conditions indicate that:

- motorists will not significantly alter their speeds until visibility in fog is below 150 m (490 ft)
- reductions in speed can be brought about through the use of signs, but drivers will still travel at a speed in excess of what is considered safe under conditions of limited visibility
- signs should be credible and specify desired speeds
- motorists travel too close to other vehicles
- variability in speeds is the factor common to most accidents
- there are questions concerning the use of signs in the fog zone.

6.6 Reduced Visibility Countermeasures

Although research on countermeasures for limited visibility has been ongoing for many years, the potential for more accidents is real and alarming. In part this is due to current highway speeds and increasing traffic volumes coupled with the reduced visibility conditions. Table 6.3 gives a summary of fatalities, injuries, and vehicles involved in fog-related accidents.

Table 6.3 Fog Related Accident Data.

State & Reporting Date	Fatalities	Injuries	Vehicles
California			
January 9, 1991	2	8	18
February 7, 1991	4	31	75
November 29, 1991*	17		364
Tennessee			
December 11, 1990	13	51	99
Utah			
January 2, 1991	3	19	55
Virginia			
April 20, 1991	2	45	54

* Due to dust storm visibility impairment

In 1991, an NTSB survey showed that 26 states had not identified a specific fog-related accident problem. A summary of the states that did report at least one fog-related, high accident location is given in Table 6.4 [3].

The effects of the reduced visibility countermeasures are described below.

Table 6.4 States Identified With Fog-Related, High-Accident Rate Locations.

Number of States Reporting Fog-Related, High-Accident Location	Number of Accident Locations	States
10	At least 1	Not available
3	2 - 3	Wisconsin, Texas, Wyoming
9	Several	Arkansas, California, Kentucky, Maine, Montana, New Jersey, North Dakota, Pennsylvania, Utah

6.6.1 Types of Highway Countermeasures for Visibility Hazards

Signs - Of the states that had identified one or more location as fog-prone accident sites, most had erected passive signs with fixed messages. Nine states were using changeable message signs and some had mobile signs.

Pavement Markings - Two states used pavement markings as countermeasures by incorporating pavement inset lights along the edge of the highway similar to airport running lights. Five states were planning the use of raised pavement markers and widening of lanes or edgelines. Four states said they used wider or closer spaced pavement markings.

Detectors - Some states were using fog detectors; however, problems were reported. Most states depended on personal observations by police and highway agency employees to detect reduced visibility conditions.

Using funding from FHWA, highway departments in Georgia and Utah will install and test experimental automated detection-and-warning systems [13]. Dense fog form in Georgia peat bogs adjacent to I-75 near Adel and quickly spreads over the highway. No mention is made of the particular technology to be tested.

Speed Limit Reductions - Four agencies reported use of speed limit reductions in fog areas. The most commonly used warning device was a passive sign, usually with a flashing beacon. Three agencies mentioned the use of convoys or restricted lanes of traffic.

Location of Countermeasures - The survey found that most of the countermeasures were used on interstate highways. Education of drivers was important, but little effort had been made to teach people how to drive in fog.

6.6.2 Countermeasures Used in California

California has approximately 966 km (600 mi) of freeways that traverse fog-prone regions. The Central San Joaquin Valley, which encompasses an area over 400 hundred miles in length including the Stockton and Fresno areas, is especially plagued with dense radiation fog during late night and early morning hours. Each year, mostly during December and January, this area experiences an average of 39 days of fog in which visibility is reduced to 0.4 km (1/4 mi) or less.

Because of these dangerous areas, California has been heavily involved in research related to countermeasures for reduced visibility. The number of accidents due to reduced visibility in from 1988 to

1991 averaged 1.3 collisions per reduced visibility day. After 1991, when countermeasures were introduced, the rate dropped to 0.2. Before countermeasures were introduced (1988 to 1991), speeding accounted for approximately 75 percent of the fog-related collisions. In the 1991 to 1992 period (after countermeasure were in place), excess speed accounted for only 33 percent of all fog-related collisions.

The California Department of transportation (Caltrans), and the California Highway Patrol (CHP) formed a partnership to reduce the number of limited visibility collisions. The mitigation strategies were to promote public awareness of the problem and to examine operational measures. The mitigation strategies included public awareness projects and operational measures. Public awareness included brochures and public service announcements, portable message signs, portable highway advisory radios, fog visibility test signs, and coordination of mitigation strategies through the Central Valley traffic operations center. Operational measures consisted of the PACE program, TARIF (Trucks at Rest in Fog) program and truck staging, truck metering, and truck convoying. The CHP PACE team used six units for patrol during commute hours on days when visibility was limited to less than 61 m (200 ft). The officer selected the safest speed for the conditions and paced all traffic at that speed before exiting the freeway and then re-entering it front of a different group of motorists to repeat the maneuver. The TARIF program encourages truck drivers to voluntarily wait out fog periods at staging areas or some other location [3].

In California, the fog conditions were categorized as:

♦ Critical fog	visibility < 61 m (200 ft)
♦ Dangerous fog	visibility 61 m to 152 m (200 ft to 500 ft)
♦ Light fog	visibility > 152 m (500 ft)

For critical fog visibility, the CHP PACE units were activated and Caltrans personnel were called to implement the other measures. California reported that the demonstration project achieved the principal objective, that of sharply reducing fog-related collisions on the test section of highway. The success of the project was attributed to the combination of public awareness, press conferences, and operational measures to assist motorists traveling on State Route 99.

Phase 1 of an advanced fog/dust automated warning system has been deployed in Caltrans District 10 (Stockton). Here an automatic fog detection and motorist alert system has been installed consisting of three major components: 9 CMS sites, 9 weather station sites, 36 speed monitoring sites, and a central monitoring and warning activation system. This system is referred to by Caltrans as the “Caltrans Automated Warning System (CAWS)”, and is currently being evaluated by the principle author of this report.

Each field station/CMS site includes a CMS, fog sensor, an open architecture transportation controller, communication devices, and a collocated substation site. All substation sites include a vehicle detector station composed of loop detectors in each lane, a controller, and communication devices. The communication system consists of 50-pair, direct-burial, twisted-pair cables and communication devices located at the field station/CMS and substation area. The PC-based central computer is located at District 10 headquarters in Stockton. The computer continuously monitors the system, providing information on messages and alarm conditions. It is also capable of inputting messages to each CMS. A satellite computer station at the CHP office in Stockton is used for monitoring purposes only.

6.6.3 Dissipation of Fog

Fog dispersal refers to artificial dissipation of fogs, usually by seeding or heating. It is done primarily at airports to improve visibility. Many attempts have been made to clear fogs at temperatures above freezing by seeding them with salt particles and by heating them with burners, but these techniques remain fairly undependable. Fog dispersal at temperatures below freezing, however, is regularly performed at many airports by seeding them with solid carbon dioxide or with propane gas sprayed from the ground.

6.6.4 Future Preventative Considerations

In Caltrans District 6 (Fresno), a weather monitoring station has also been proposed to provide motorists with real-time driving conditions to include advanced warning and monitoring of fog and other types of inclement weather. Pavement sensors, small weather stations with visibility sensors, and a processing unit are included in this system. A second similar system proposed for this area is a flow interruption monitoring system to provide real-time detection of traffic speeds and accidents. It consists of inductive loop detectors and CCTV. A separate CCTV monitoring system is also planned. It provides visual information to select appropriate CMS and HAR messages without the present delay in confirming the incident site's weather or traffic problems.

Another possible future fog countermeasure is the visual readout radar. The speed of a motorist is shown to him on the visual readout radar unit. A CMS located a short distance downstream indicates the visibility distance. Another monitor then measures the motorist's speed again to determine what effect the sign has. This system provides education, association of speed with visibility, perhaps makes motorists think about their driving behavior, and produces speed alteration.

7 Atmospheric Transmission for Selected Spectral Bands

Atmospheric attenuation is produced by two phenomena – absorption and scattering. Absorption is dependent on the frequency of operation and the gases and pollutants that are present. Scattering is dependent on the size, shape, and dielectric constant of the scattering objects and the wavelength of the energy that is being scattered. Atmospheric constituents such as oxygen, water vapor, and carbon dioxide play a dominant role in determining millimeter-wave and infrared attenuation. The internal energy states of these molecules define frequencies at which the molecules absorb energy, thus creating frequency bands of high attenuation. These regions of the electromagnetic spectrum may be used to broadcast short range communications that are intended to be difficult to intercept, and to gather information used for weather forecasting and cloud top location. Relatively low absorption exists at still other portions of the electromagnetic spectrum called windows. Sensors that operate at these frequencies can propagate energy over greater distances for long range target detection and for earth resource monitoring. Weather-related obscurants such as rain, snow, and fog add to the absorption and scattering experienced under clear weather conditions and further limit sensor performance. Models that adequately predict atmospheric absorption and scattering in the millimeter-wave and infrared spectra may be used when measured data are not readily available at specific frequencies or atmospheric conditions. A discussion of absorption and scattering phenomena is presented below.

7.1 Influence of Wavelength on Atmospheric Attenuation

Figure 7.1 compares the atmospheric attenuation of higher resolution IR and visible sensors to millimeter-wave sensors. The oscillatory curve with the peaks and valleys in attenuation corresponds to 1 atmosphere of pressure at a temperature of 20^{o}C and water density of 7.5 g/m^3. Window frequencies in the millimeter-wave spectrum, denoted by absorption minima, occur at approximately 35, 94, 140, 225, and 350 GHz. Sensors that detect and classify targets at long ranges are typically designed for operation at these windows. Peak absorption occurs in the microwave and millimeter-wave spectra at approximately 22, 60, 118, 183, and 320 GHz. Absorption at 60 and 118 GHz is due to oxygen, while absorption at the other frequencies is due to water vapor. The absorption frequency bands find use in sensors flown in weather satellites and applications that require secure communications.

The infrared absorption spectra are due to molecular rotations and vibrations that occur in atmospheric molecules. The near-infrared wavelength band extending from 0.77 to 1.5 μm is constrained at the upper end by water vapor absorption. The mid-infrared wavelength band from 3 to 5 μm is bounded on the lower and upper ends by water vapor absorption. An absorption peak in the middle of the band is due to carbon dioxide. The far-infrared band or thermal infrared extends from approximately 8 to 12 μm and beyond. The lower wavelength is restricted by water vapor and the upper by a combination of water vapor and carbon dioxide.

In moderate and heavier rain, millimeter-wave frequencies of 97 GHz and above are generally subject to similar attenuation effects as the near infrared as the rain rate curves of 4, 25, and 150 mm/hr show. At frequencies below 100 GHz, drizzle (0.25 mm/hr) produces less attenuation on millimeter-wave energy than on infrared. The final curve in Figure 7.1 illustrates that a fog with 0.1 g/m^3 liquid water content is a greater attenuator of infrared and visible spectrum energy than millimeter-wave energy.

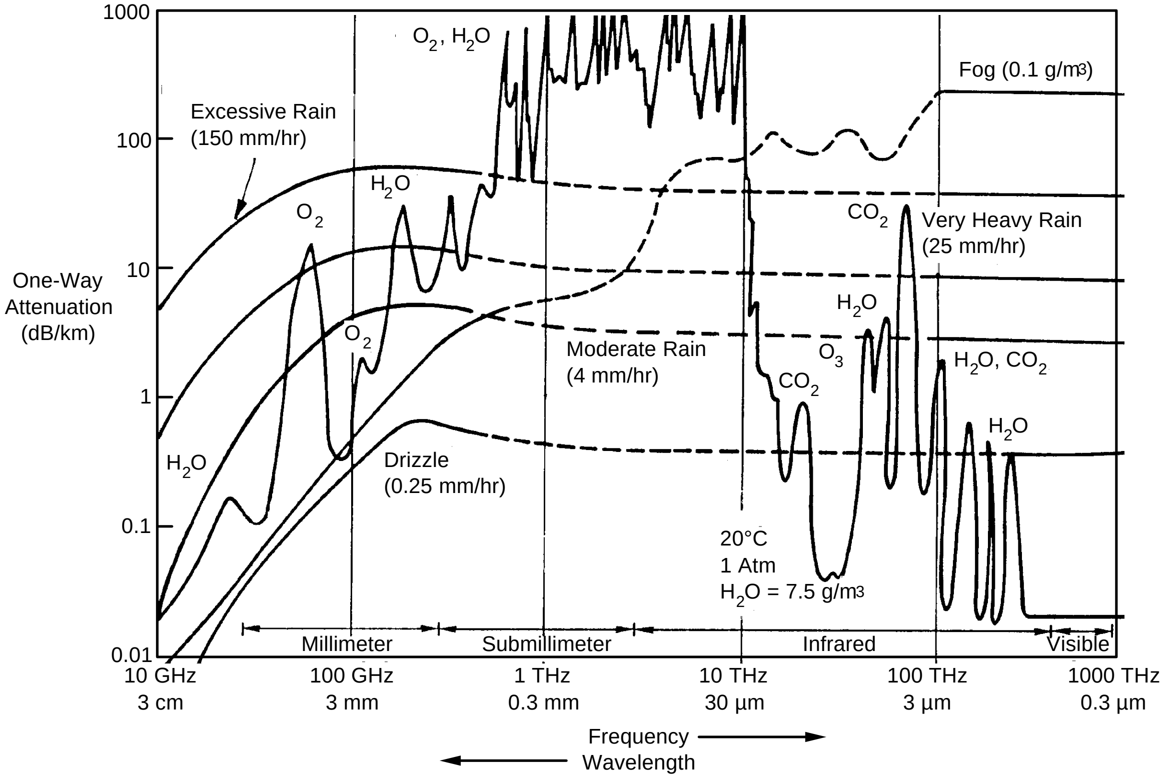

Figure 7.1 Atmospheric attenuation spectrum from 0.3 μm to 3 cm [14].

7.2 Absorption and Scattering of Electromagnetic Energy by Atmospheric Constituents

The transmittance of visible and infrared energy through a sea-level atmosphere is shown in Figure 7.2 [15]. Unlike the absorption data commonly quoted for radar transmission, these infrared data show the percent of energy transmitted. The principle permanent atmospheric constituents contributing to the absorption of energy at infrared wavelengths are carbon dioxide, nitrous oxide, and methane. Variable constituents that absorb infrared energy include water and ozone. In addition to absorption, infrared energy is scattered from molecules and aerosols in the atmosphere. Wavelengths less than 2 μm experience negligible molecular scattering. Scattering from aerosols is a function of the radius of the scatterer divided by the wavelength. Aerosol-type scatterers include rain, dust, fog, and smoke.

7.3 Micron-Wavelength Energy Propagation in Cloud, Fog, and Haze

One method of modeling the attenuation produced by fog is to treat clouds, fog, and haze as spherical water droplets using Mie scattering theory to compute backscatter coefficients and asymmetry parameters [16]. Water droplet diameters in clouds, fog, and haze range from 0.1 to 100 μm, density from 1 cm^{-3} to 10^3 cm^{-3}. The conclusions reached in this study were that extinction is small when the droplet diameter is much smaller than the wavelength of the transmitted energy. The extinction coefficient reaches a maximum when the water droplet diameter equals 16 µm. The backscatter coefficient fluctuates when the diameter reaches 3.8 µm (implication for 10.6-µm laser radar).

When the droplets are small (diameter ≤ 1 µm), absorption dominates as the scattering albedo, equal to the ratio of scattering coefficient to extinction coefficient, is also small. (The extinction coefficient is the sum of the absorption and scattering coefficients.) When the droplets become larger, scattering is more important. At approximately 10 µm, absorption and scattering have about equal effects.

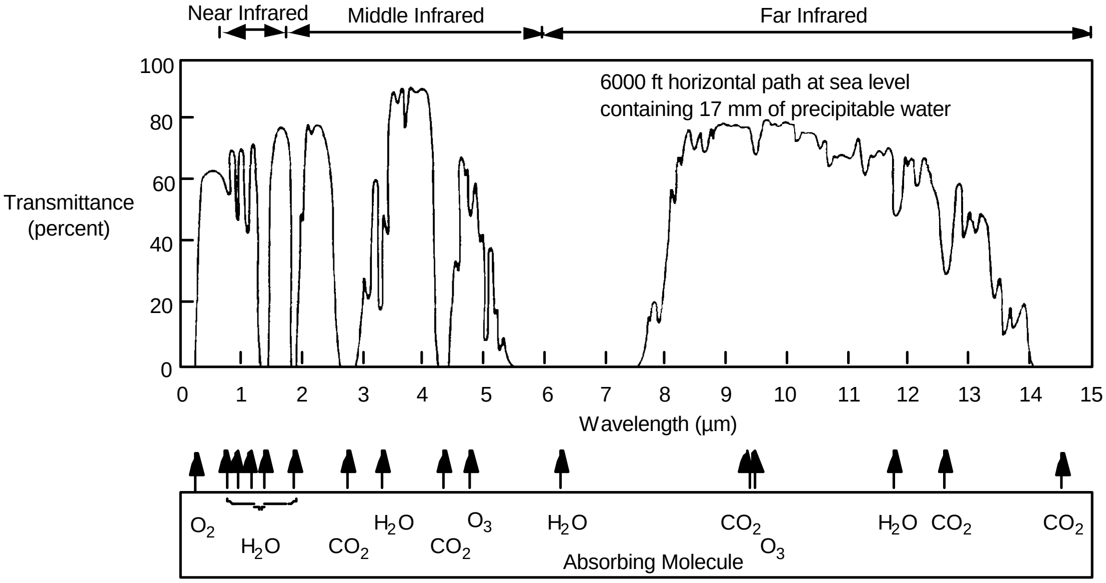

Figure 7.2 Infrared transmittance of the atmosphere. *Source:* Hudson, R.D., *Infrared System Engineering*, John Wiley and Sons, New York, 1969. Copyright © 1969 by R.D. Hudson. Reprinted by permission of R.D. Hudson.

When the droplet size and density are large enough (at some value greater than 5µm for droplet size), multiple scattering occurs as in thick clouds or heavy fog. Reflectance approaches a limiting value (dependent on droplet size) and does not increase further as distance increases.

7.4 LOWTRAN Atmospheric Attenuation Model

The extinction coefficient g(l) mentioned in Section 7.3 is a complex function of wavelength as may be inferred from Figure 7.2 and the expression in (7.1) for the average value of the transmission $\overline{\tau}_a$ over a wavelength band l $_1$ to l $_2$:

$$\overline{\tau}_a = \frac{1}{\lambda_2-\lambda_1}\int_{\lambda_1}^{\lambda_2} exp[-\gamma(\lambda)R]d\lambda \qquad (7.1)$$

Values for $\overline{\tau}_a$ are generally obtained from computer-hosted programs such as LOWTRAN [17, 18, 19], that covers a spectral range of 0 to 50,000 cm^{-1} (0.2 µm to infinity) with a resolution of 20 cm^{-1} full width at half maximum (FWHM). It models radiance from single and multiple scattering and path geometries from space-viewing ground-based sensors, air-to-air scenarios, surface point-to-point paths, and earth-viewing airborne sensors.

In LOWTRAN 7 (the most recent LOWTRAN code), the user specifies the geographical atmospheric model (from one of six defined in the LOWTRAN program or from user-generated input), the altitude- and seasonal-dependent aerosol profiles, and the extinction coefficients. The six program-defined atmospheric models are tropical, mid-latitude summer, mid-latitude winter, sub-arctic summer, sub-arctic winter, and 1976 U.S. standard. Each defines the temperature, pressure, density, and atmospheric gases mixing ratio as a function of altitude. Table 7.1 shows the rural, urban, maritime, tropospheric, and fog aerosol models that are available for the atmospheric boundary layer [17, 18]. Seasonal models for the aerosol profiles of the troposphere (2 – 10 km) and stratosphere (10 – 30 km), and transition profiles for the stratosphere up to 100 km are also available. Rain rate, cloud models, wind speed, and other atmospheric parameters can be varied to tailor the model to the conditions under which the atmospheric transmission is desired. The input parameters for executing LOWTRAN 7 are contained on five main cards and thirteen optional cards. The types of information contained on each card are summarized in Table 7.2 [19].

Table 7.1 LOWTRAN aerosol models for the atmospheric boundary layer.

Aerosol Model	Representative Region	Constituent
Rural (0 to 2 km altitude)	Continental areas not directly influenced by urban/industrial aerosol sources	Atmospheric gases and surface dust particles
Urban (0 to 2 km altitude)	Modifies rural background by adding aerosols from combustion products and industrial sources	20%/80% mixture of carbonaceous aerosols to rural type aerosols, respectively
Maritime (0 to 2 km altitude)	Aerosols of oceanic origin	Sea salt particles
Tropospheric (2 to 10 km altitude)	Troposphere with extremely clear conditions and uniform aerosol properties	Rural model constituents without large particles
Fog 1 (0 to 2 km altitude)	Advection fog	Default visibility = 0.2 km
Fog 2 (0 to 2 km altitude)	Radiation fog	Default visibility = 0.5 km

Table 7.2 LOWTRAN 7 Input Card Information.

Card	**Information**
1	Specifies one of six geographical-seasonal model atmospheres or user-specified model; horizontal, vertical, or slant atmospheric path; transmittance or radiance calculation; scattering option
2	Altitude and seasonal-dependent aerosol profiles and aerosol extinction coefficients, cloud and rain models, wind speed, altitude of surface relative to sea level
2A	Cirrus cloud altitude profile
2B	Vertical structure algorithm of aerosol extinction and relative humidity for low visibility or low ceiling conditions as occur with: (1) cloud/fog at the surface, (2) hazy/light fog, (2') clear/hazy, (3) radiation fog or inversion layer, (4) no cloud ceiling or inversion layer
2C	Additional data for user-defined atmospheric model (if selected on Card 1)
2C1	Additional data for user-defined atmospheric model (if selected on Card 1)
2C2	Additional data for user-defined atmospheric model (if selected on Card 1)
2C3	Additional data for cloud, fog, and rain user-defined atmospheric model (if selected on Card 1)
2D	User-defined attenuation coefficients for any or all four of the aerosol altitude regions (boundary layer, troposphere, stratosphere, above stratosphere to 100 km)
2D1	Conversion factor from equivalent liquid water content (gm/m^3) to extinction coefficient (km^{-1})
2D2	User-defined aerosol or cloud extinction coefficients, absorption coefficients, and asymmetry parameter
3	Geometrical path parameters
3A1	Solar/lunar scattered radiation
3A2	Additional parameters for solar/lunar scattered radiation
3B1	User-defined phase functions
3B2	Additional parameters for user-defined phase functions
4	Spectral range and calculation increment (frequency step size in cm^{-1})
5	Recycle parameter to iterate the calculations through the program so that a series of problems can be run with one submission of LOWTRAN

Figures 7.3 through 7.5 illustrate the extinction and absorption coefficients in Np/km as derived from aerosol models. The extinction coefficients have been normalized to unity at 0.55 μm. The clear atmosphere condition referenced in these plots is based on a visibility range of 23 km.

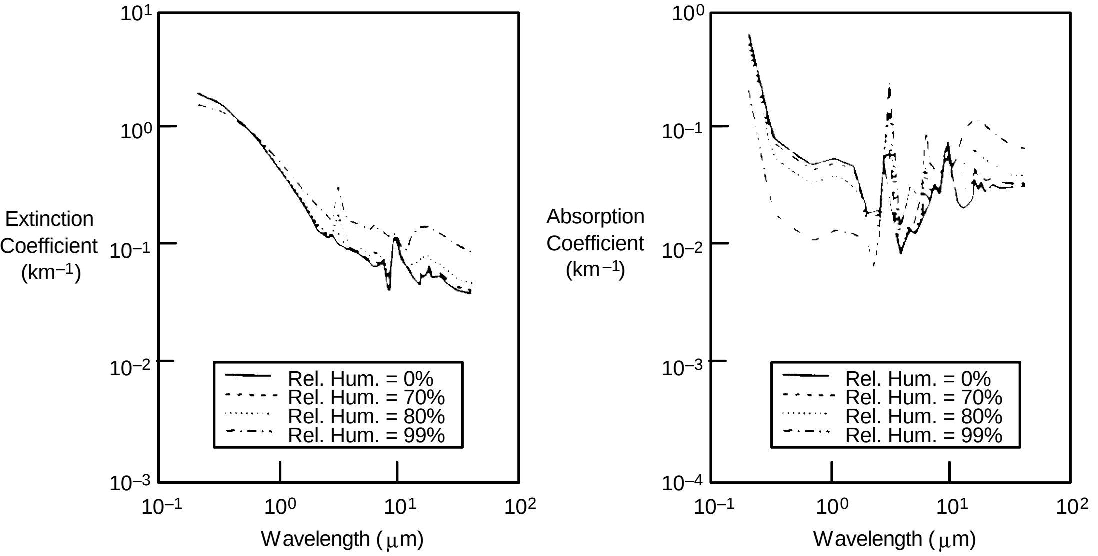

- Rural Model
  - Representative of continental areas not directly influenced by urban/industrial aerosol sources
  - Atmospheric gases and surface dust particles dominate model

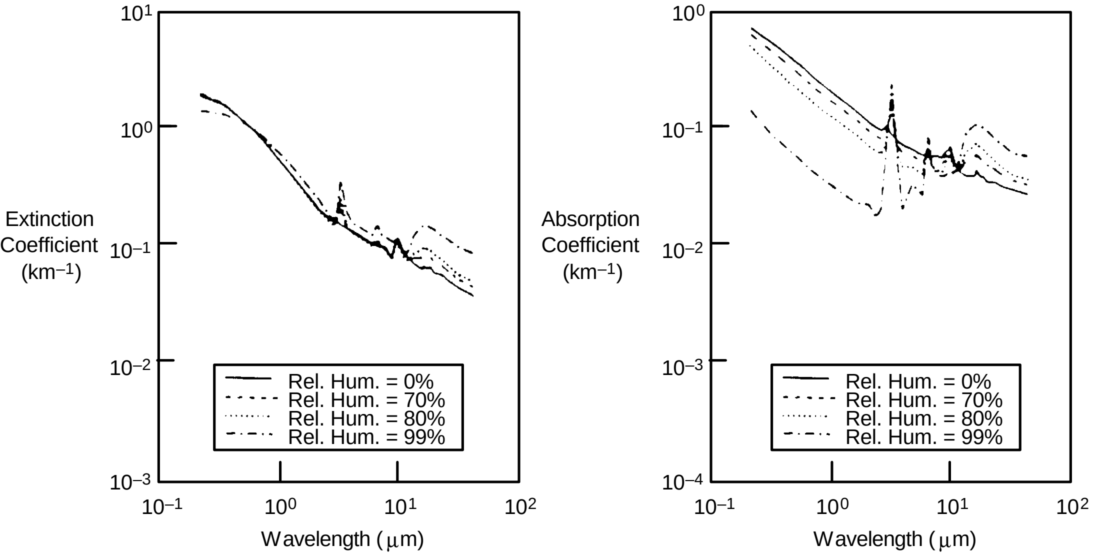

- Urban Model
  - Modifies rural background by adding aerosols from combustion products and industrial sources
  - 20%/80% mixture of carbonaceous aerosols to rural-type aerosols, respectively

Figure 7.3 Extinction and absorption coefficients in urban and rural aerosols as derived from LOWTRAN 5 model. *From:* Kneizys, F.X., *et al.*, *Atmospheric Transmittance/Radiance: Computer Code: LOWTRAN 5*, AFGL-TR-80-0067, AFGL, Hanscom AFB, MA 01731, 1980.

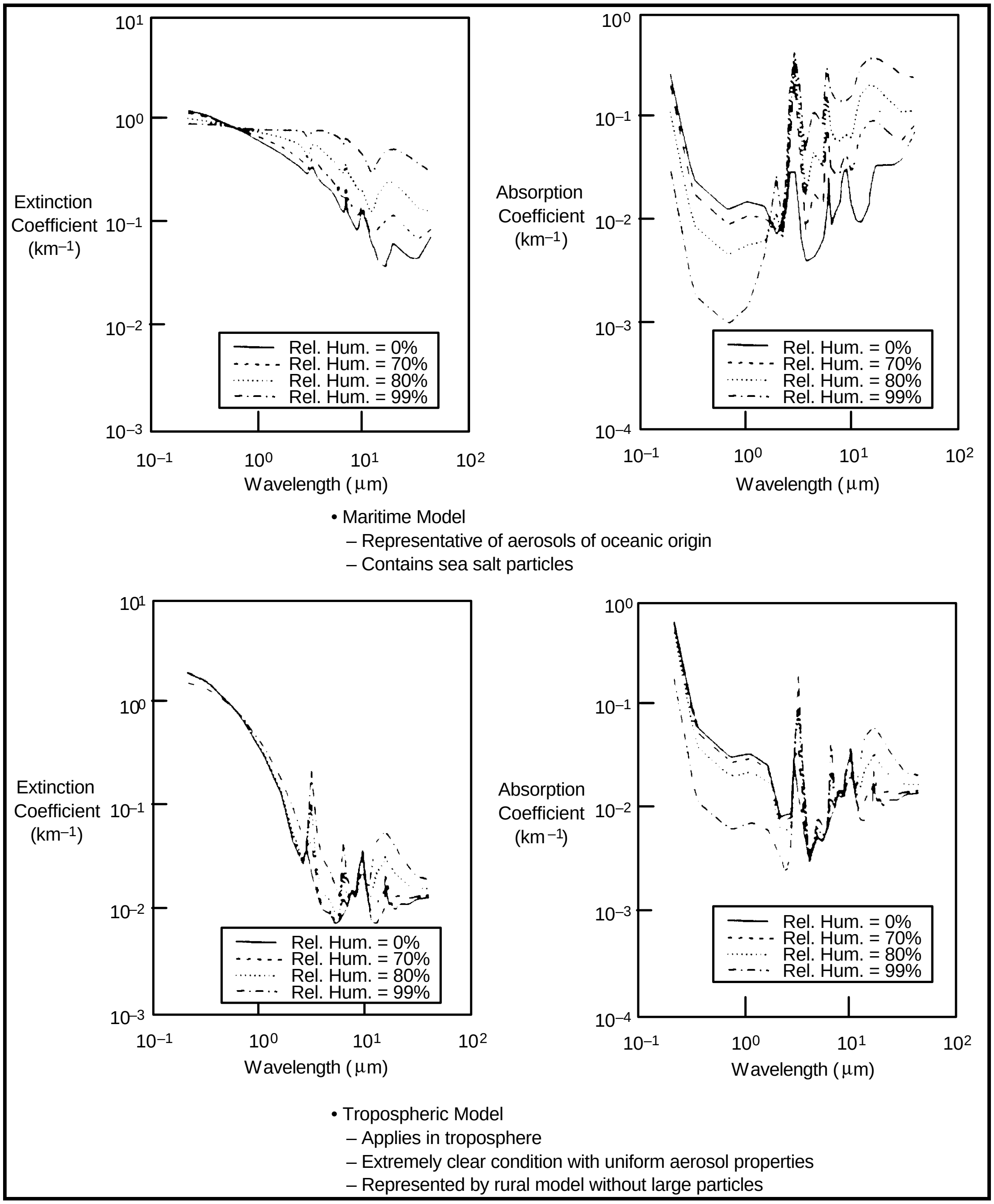

- Maritime Model
  - Representative of aerosols of oceanic origin
  - Contains sea salt particles

- Tropospheric Model
  - Applies in troposphere
  - Extremely clear condition with uniform aerosol properties
  - Represented by rural model without large particles

Figure 7.4 Extinction and absorption coefficients in maritime and tropospheric aerosols from LOWTRAN 5 model. *From:* Kneizys, F.X., *et al.*, *Atmospheric Transmittance/Radiance: Computer Code: LOWTRAN 5*, AFGL-TR-80-0067, AFGL, Hanscom AFB, MA 01731, 1980.

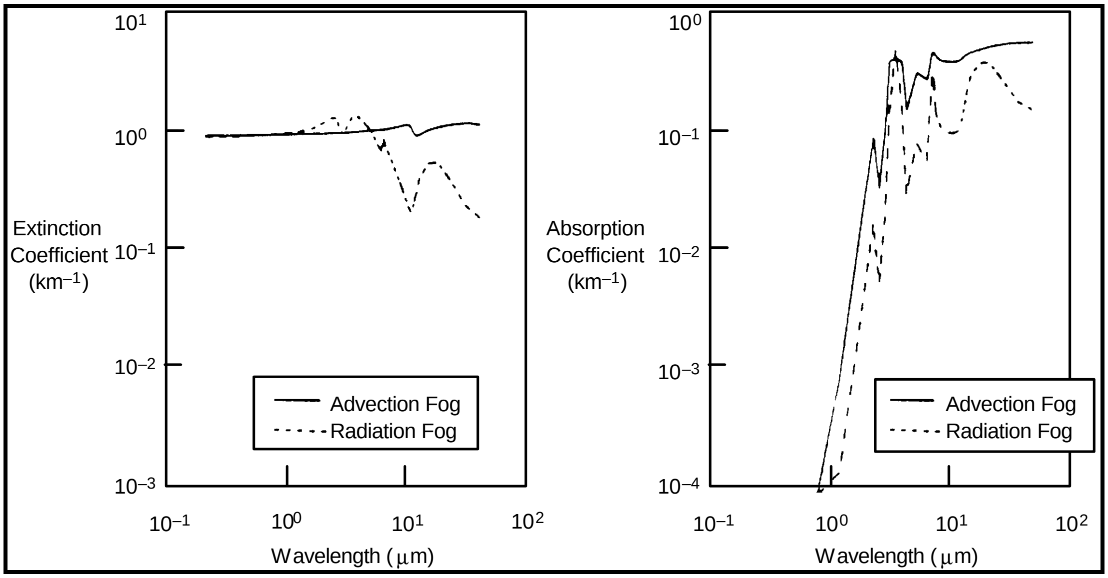

Figure 7.5 Extinction and absorption coefficients in advection and radiation fog from LOWTRAN 5 aerosol model. *From:* Kneizys, F.X., *et al.*, *Atmospheric Transmittance/Radiance: Computer Code: LOWTRAN 5*, AFGL-TR-80-0067, AFGL, Hanscom AFB, MA 01731, 1980.

Rain attenuates object-to-background contrast in infrared imagery in two ways, first by introducing an attenuation loss over the signal path to the receiver, and second by cooling the target [20]. A set of atmospheric transmission curves produced by LOWTRAN 6 for several values of rain rate is shown in Figure 7.6. Here wave number (in units of cm^{-1}) is defined as the reciprocal of wavelength, measurement path is 300 meters, surface and dew point temperatures are both equal to 10^{o}C, and the meteorological visibility range is 23 km in the absence of rain.

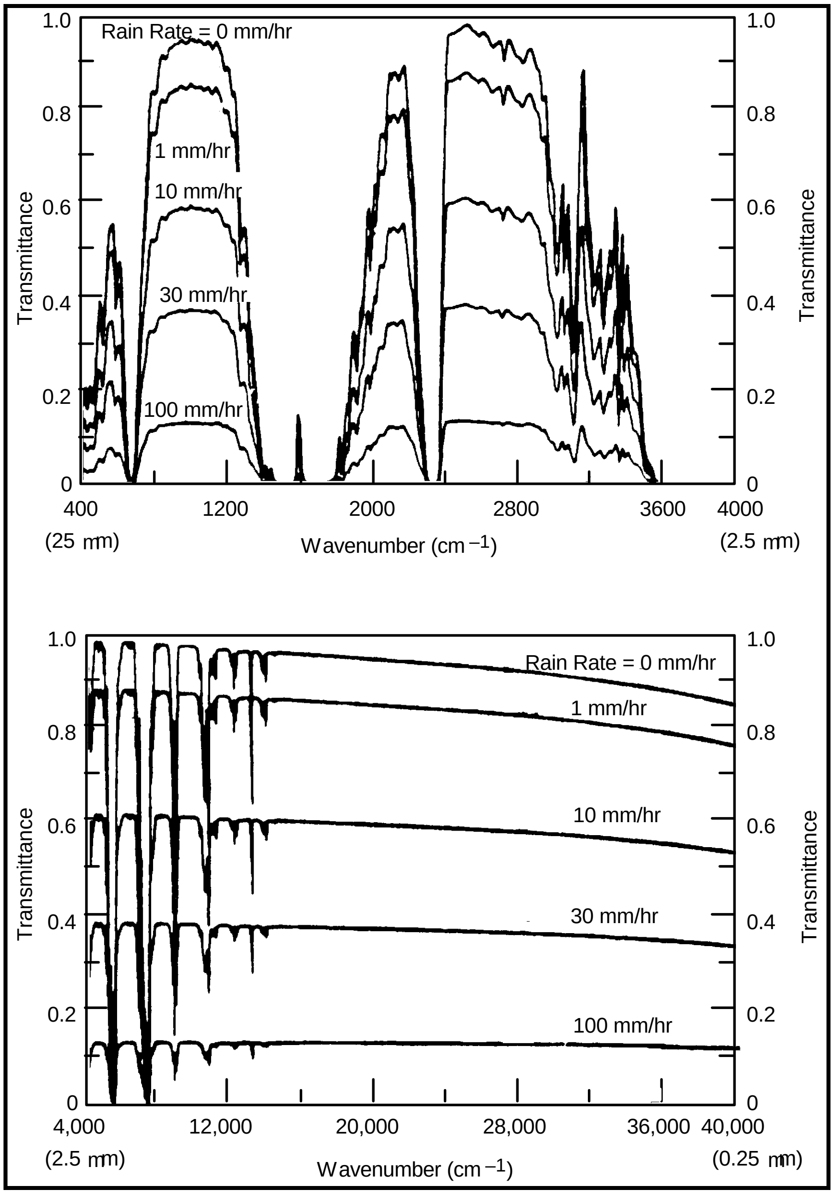

- Wavenumber = 1/wavelength
- Measurement path = 300 m
- Surface temperature = Dew point temperature = 10^{o}C
- Meteorological range = 23 km in absence of rain

Figure 7.6 Atmospheric transmittance in rain for 0.25 to 25 µm wavelength interval. *From:* Kneizys, F.X., *et al.*, *Atmospheric Transmittance/Radiance: Computer Code LOWTRAN 6*, AFGL-TR-83-0187, AFGL, Hanscom AFB, MA 01731, 1983.

In addition to LOWTRAN, there are other models available to assess the effects of weather on sensor systems. These include FASCODE and MODTRAN that are supported by the U.S. Air Force Geophysics Laboratory at Hanscom Air Force Base, Bedford, Massachusetts 01731 [21, 22, 23, 24, 25, 26]. FASCODE models very high altitude (>70 km) and very narrow spectral bands that are applicable to laser-line resolution. It is useful for extinction dominated by molecular absorption, improving upon the resolution offered by LOWTRAN in this region. MODTRAN was written for moderate resolution calculations that do not require FASCODE. Both programs are available from the Geophysical Laboratory.[1]

7.5 MODTRAN Atmospheric Attenuation Model

MODTRAN is a version of LOWTRAN 7 with six additional routines that increase the 20 cm^{-1} spectral resolution found in LOWTRAN to 2 cm^{-1} FWHM [22]. It also allows the modeling of molecular absorption of atmospheric molecules as a function of temperature and pressure and provides new capabilities for calculating three absorption band parameters for twelve LOWTRAN molecular species (water vapor, carbon dioxide, ozone, nitrous oxide, carbon monoxide, methane, oxygen, nitric oxide, sulfur dioxide, nitrogen dioxide, ammonia, and nitric acid). The absorption band parameters used in MODTRAN are temperature dependent and include an absorption coefficient, a line density parameter, and an average linewidth. LOWTRAN 7, on the other hand, uses only the absorption coefficient to define the absorption band. The increased resolution in MODTRAN applies to the 0 to 17,900 cm^{-1} spectral region.

The new MODTRAN subroutines are written in portable ANSI-standard FORTRAN and are constructed to minimize coding changes when they are interfaced with LOWTRAN 7. All the usual LOWTRAN options such as aerosol models, path selection, multiple scattering models, and user-specified profiles have been maintained in MODTRAN.

The input data sequence for MODTRAN is identical to LOWTRAN 7 except for two modifications, an additional parameter on Cards 1 and 4. A logical parameter MODTRN has been added to the front end of Card 1 such that the card data appear as

```
      READ(IRD, '(L1,I4,I2I5,F8.3,F7.2)')MODTRN,MODEL,ITYPE,IEMSCT,
     1    IMULT,M1,M2,M3,M4,M5,M6,MDEF,IM,NOPRT,TBOUND,SALB
```

The input to Card 4 has been changed to integer format with a resolution parameter IFWHM added such that the card data appear as

```
      READ(IRD,'(4I10)')IV1,IV2,IDV,IFWHM
```

The logical parameter MODTRN acts as a switch that, when set to F (false), causes the regular LOWTRAN 7 to execute. When set to T (true), it activates MODTRAN. The parameter IFWHM, that is only read if MODTRN is true, specifies the full width at half maximum of an internal triangular slit function.

7.6 Tactical Decision Aid Software Program

Battelle in Cambridge, MA has developed a Tactical Decision Aid (TDA) software program that evaluates the impact of adverse weather on sensor performance and provides assistance in selecting the appropriate sensor for a task.[2] The model has been validated for predicting the performance of television, infrared, non-imaging laser, and night vision goggles. A summary of the TDA capabilities is shown in Figure 7.7.

---

[1] The contact personnel are Gail Anderson: Ganderson@plh.af.mil and Jim Chetwynd: Chetwynd@plh.af.mil.

[2] The contact person for the TDA program is Dr. Jeffrey Everson, Battelle Cambridge Program Office, Three Cambridge Center, Suite 204, Cambridge, MA 02142, (617) 577-7250.

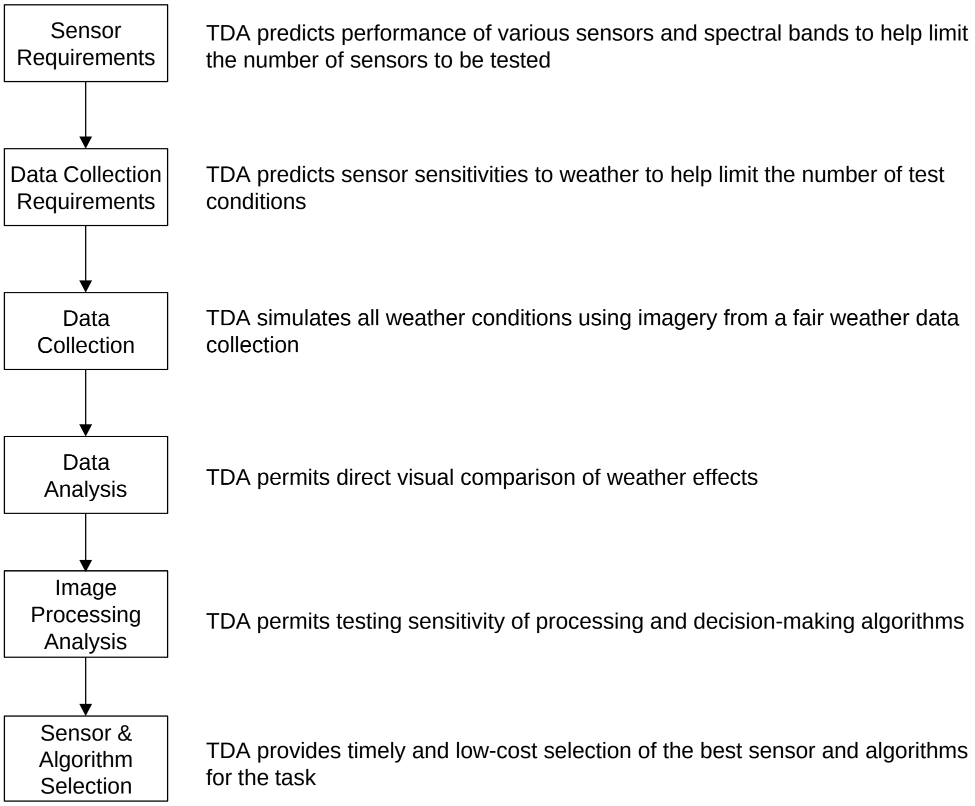

TDA predicts performance of various sensors and spectral bands to help limit the number of sensors to be tested

TDA predicts sensor sensitivities to weather to help limit the number of test conditions

TDA simulates all weather conditions using imagery from a fair weather data collection

TDA permits direct visual comparison of weather effects

TDA permits testing sensitivity of processing and decision-making algorithms

TDA provides timely and low-cost selection of the best sensor and algorithms for the task

Figure 7.7 Application of TDA Software Program

7.7 EOSAEL Sensor Performance Model

EOSAEL (Electro-Optical Systems Atmospheric Effects Library) is a comprehensive model for analyzing a variety of physical processes that affect the performance of millimeter-wave and infrared sensors, as well as those that operate in the visible, ultraviolet, and on 53 laser lines [27, 28]. It addresses the phenomena listed below that describe various aspects of electromagnetic propagation and scenarios of interest in defense applications:

- Spectral transmission and contrast transmission
- Multiple scattering
- Sensor performance
- Transport and diffusion
- Turbulence effects on imaging
- High energy laser propagation
- Radiative transfer
- Thermal contrast
- Generation of battlefield obscurants
- Climatology for 47 nonoverlapping climatic regions

The software consists of 26 modules that are divided into six categories: atmospheric gases, natural aerosols, battlefield aerosols, radiative transfer, laser propagation, and target acquisition and system performance. The modules are more engineering oriented than based on first principals. The EOSAEL development philosophy was to include modules that give reasonably accurate results, while minimizing computer time, for conditions that may be expected on a battlefield. The modules can be run under the control of an executive routine or executed in a stand-alone mode. Versions are available in FORTRAN 77 that allow the program to run on a variety of computers. The 26 EOSAEL modules and their functions are listed in Table 7.3. Three modules of particular interest are the previously discussed LOWTRAN and NMMW (both found in the gases category) and TARGAC. NMMW models the effects of atmospheric gases on millimeter-wave sensors. TARGAC, in the target acquisition and system performance category, is built into the FLIR performance model discussed in Section 5.3. Government agencies and organizations under contract to the U.S. government can obtain copies of EOSAEL from the U.S. Army Atmospheric Sciences Laboratory at White Sands Missile Range, New Mexico.

Table 7.3 EOSAEL modules and their functions.

Category	Module	Valid Range	Function
Gases	LOWTRAN	0.25 to 28.5 µm	Calculates atmospheric transmittance, radiance, and contrast due to specific molecules at 20 inverse cm spectral resolution on a linear wave-number scale
	LZTRAN	Visible to far IR (0.5 to 11.0 µm)	Calculates transmission through atmospheric gases at specific laser frequencies for slant or horizontal paths
	NMMW	10 to 1000 GHz (0.3 to 30.0 mm)	Calculates transmission, backscatter, and refractivity due to gaseous absorption, fog, rain, and snow
Natural Aerosols	XSCALE	0.2 to 12.5 µm	Calculates fog and haze transmission for horizontal or slant paths, and rain and snow transmission for horizontal paths
	CLIMAT	Not applicable	Provides values of meteorological parameters for select European, Mideastern, Korean, Alaskan, Scandinavian, Central American, Indian, SE Asian, South American, and Mexican locales
	CLTRAN	0.2 to 2.0 µm 3.0 to 5.0 µm 8.0 to 12.0 µm	Calculates slant path transmission through six cloud types
	COPTER	0.4 to 0.7 µm 3.0 to 5.0 µm 8.0 to 12.0 µm 0.3 to 30.0 mm	Calculates effects of looses snow or dust lofted by helicopter downwash
Battlefield Aerosols	COMBIC	0.4 to 1.2 µm 3.0 to 5.0 µm 8.0 to 12.0 µm and 94 GHz (3 mm)	Calculates size, path length, concentration, and transmission through various smokes and artillery or vehicular dirt and dust particles
	SABRE	Not applicable	Calculates effects of terrain on wind flow and smoke screens
	KWIK	Not applicable	Provides a placement and number of smoke munitions necessary to produce a screen that reduces the probability of target detection to a given level
	GRNADE	0.4 to 1.2 µm 3.0 to 5.0 µm 8.0 to 12.0 µm and 94 GHz (3 mm)	Models obscuration produced by tube-launched grenades used in self-screening applications
	FITTE	0.4 to 12.0 µm	Calculates dimensions of and transmittance through plumes from burning vegetation and vehicles
	MPLUME	Not applicable	Calculates performance degradation of target designation systems by missile smoke plumes

Table 7.3 EOSAEL modules and their functions (continued).

Category	Module	Valid Range	Function
Radiative Transfer	FCLOUD	Any wavelength included in the phase function file PFNDAT*	Calculates beam transmittance, path radiance, and contrast transmittance through a homogeneous ellipsoidal cloud
	OVRCST	Any wavelength	Calculates beam transmittance, path radiance, and contrast transmittance along an arbitrary line of sight under an overcast sky
	MSCAT	Any wavelength included in the phase function file PFNDAT	Calculates multiple scattering of a laser beam into a detector from an ellipsoidal aerosol cloud
	ASCAT	Any wavelength included in the phase function file PFNDAT	Calculates effects of multiple scattering for transmissometer and lidar configurations
	ILUMA	Photopic	Prediction of natural illumination under realistic atmospheric conditions
	FASCAT	0.55 and 1.06 µm	Determination of path radiance and contrast effects
	GSCAT	Visible	Determines path radiance effects
	LASS	Visible	Determines the effectiveness of smoke screens deployed against large fixed and semifixed installations
	REFRAC	≈0.4 to ≈20.0 µm	Calculates the amount of curvature a ray of light experiences as it passes over a complex terrain surface
Laser Propagation	IMTURB	<14 µm	Predicts the effects of laser propagation through optical turbulence in the weak fluctuation regime
	NOVAE	<14 µm	Calculates linear and nonlinear effects on high-energy laser beam propagation from clear air, smokes, and aerosols
Target Acquisition and System Performance	TARGAC	Visible to mid-IR	Evaluates the combined atmospheric and system effects to determine the range for target detection and classification
	RADAR	0.1 to 350 GHz	Calculates millimeter-wave system performance

* PFNDAT contains phase functions, extinction and scattering coefficients, and the single-scattering albedo for 38 natural and man-made aerosols at 16 wavelengths ranging from 0.55 to 12.0 µm.

7.8 Extinction Coefficients for Common Obscurants

Summary values for the extinction coefficients of atmospheric obscurants are shown in Table 7.4 for the visible, infrared, and millimeter-wave spectral bands [29]. These can be inserted into (7.1) to calculate the transmittance in the presence of the obscurant. As expected, the effects of the smokes and inclement weather are greatest at the shorter wavelengths.

Table 7.4 Extinction coefficients of atmospheric obscurants. *From: Smoke and Natural Aerosol Parameters* (*SNAP*) *Manual*, Joint Technical Coordinating Group for Munitions Effectiveness, Smoke and Aerosol Working Group, Report 61, JTCG/ME-85-2, April 26, 1985.

Approximate Ranges of Extinction Coefficients (Np/km)

Atmospheric Obscurant	**Spectral Region**				
	Visible **0.4 to 0.7 µm**	**Mid IR** **3 to 5 µm**	**Far IR** **8 to 12 µm**	**MMW** **(35 GHz) 8.6 mm**	**MMW** **(95 GHz) 3.2 mm**
Gases	Very low ≈ 0.02	Low/med 0.25 to 0.73	Very low/med 0.03 to 0.8	Very low 0.02 to 0.06	Very low/low 0.03 to 0.2
Haze	Low/med 0.2 to 2.0	Very low/med 0.02 to 1.0	Very low/low 0.02 to 0.4	Very low ≈ 0.001	Very low ≈ 0.001
Fog	High 2.0 to 20	Med/high 1.0 to 20	Med/high 0.4 to 20	Very low/low 0.001 to 0.1	Very low/low 0.01 to 0.4
Rain	Low/med 0.3 to 1.6	Low/med 0.3 to 1.6	Low/med 0.3 to 1.6	Very low/med 0.05 to 1.0	Low/med 0.3 to 2.0
Snow	Med/high 2.0 to 12	Med/high 2.0 to 12	Med/high 2.0 to 12	Very low/med 0.004 to 1.0	Very low/med 0.03 to 1.0
Dust	Low/high 0.2 to 4.0	Low/high 0.2 to 4.0	Low/high 0.2 to 4.0	Very low 0.0005 to 0.005	Very low 0.0005 to 0.005

Extinction Coefficient	**Descriptive term**	**Visual Range**
< 0.1 Np/km	Very low	> 30 km, very clear
0.1 to 0.5 Np/km	Low	6 to 30 km, clear to hazy
0.5 to 2 Np/km	Medium	2 to 6 km, hazy
> 2 Np/km	High	< 2 km, foggy

7.9 The Highway Environment

As discussed in Section 7.1, although the atmosphere is opaque over much of the electromagnetic spectrum from the infrared to the millimeter-wave, there are several windows of low attenuation where imagery of a scene is possible. Figures 7.8 and 7.9 show atmospheric transmissivity (the inverse of attenuation) as a function of the wavelength of the detected electromagnetic radiation for radiative and advective fog, respectively [30]. The standard fog models developed by the Air Force Office of Scientific Research (AFOSR), referred to as Fog 1 (advective fog with visibility equal to 0.2 km) and Fog 2, (radiative fog with visibility equal to 0.5 km) were used to generate these figures.

Each plot is the composite of many MODTRAN evaluations, in order to span three orders of magnitude in wavelength at adequate resolution. The entire range from the visible through millimeter-wave band is shown on each plot. In working with the simulation models, it was noted that the transmissivity is extremely sensitive to small changes in the water content of the fogs. These data represent typical atmospheric compositions. The actual attenuation in a fog bank encountered on a highway could differ from that predicted by the simulation, due to variations in the composition and heterogeneous distribution of the actual fog.

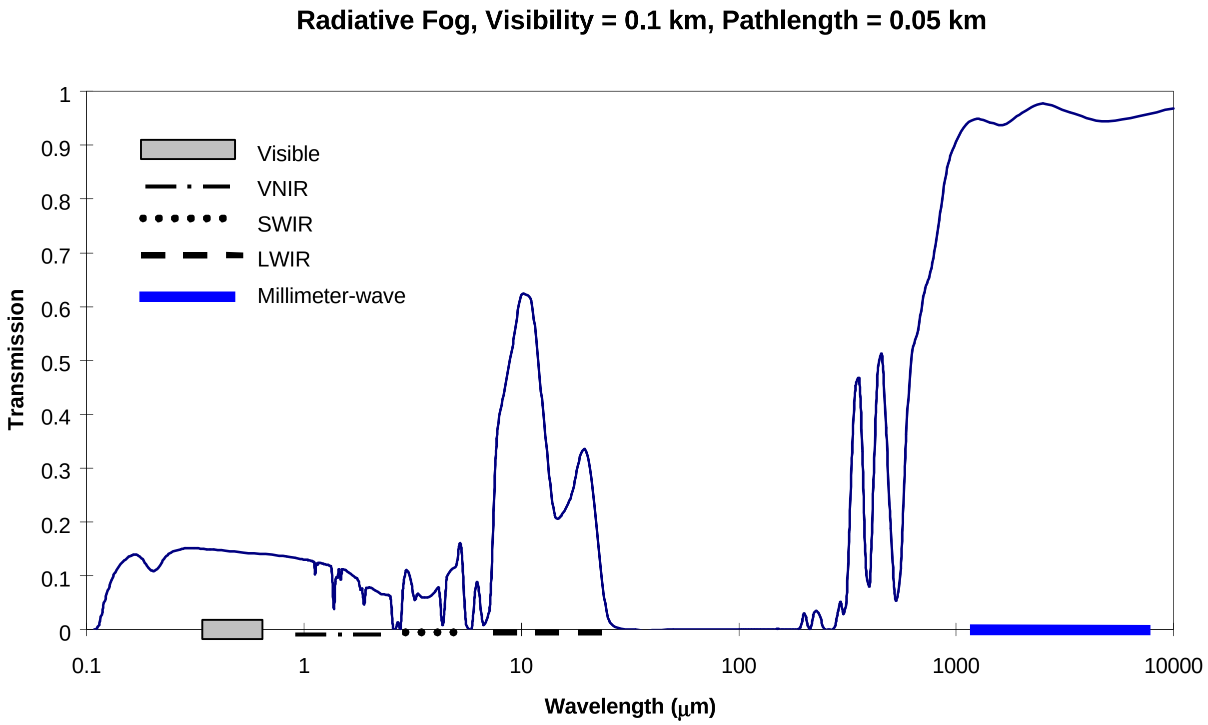

Figure 7.8 Atmospheric Transmission, Medium Density Radiative Fog.

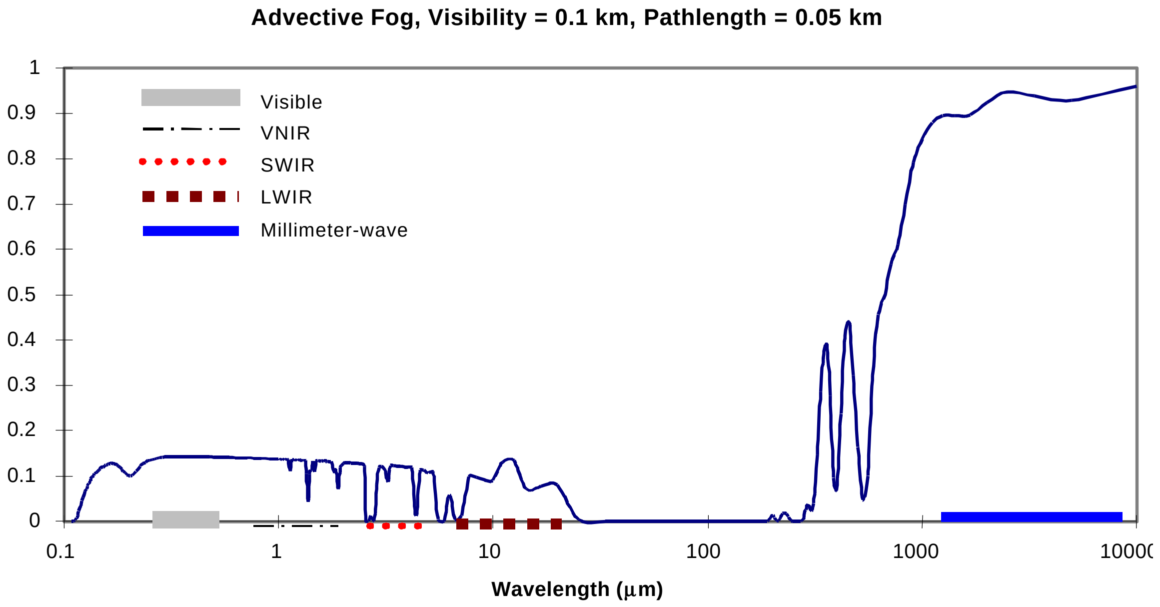

Figure 7.9 Atmospheric Transmission, Medium Density Advective Fog.

The radiation fog of Figure 7.8 is characteristic of valley fog common in central California formed when the temperature drops below the dew point in still air. Such effects often occur when heat is lost from ground radiation to the open sky. Radiative fog is unpredictable and transient and, hence, is a significant causative factor in visibility-related traffic incidents.

The advective fog characteristics shown in Figure 7.9 are common in coastal or mountainous areas of California. It is distinguished by wind transport of moist air and subsequent temperature drops caused by mixing with colder air and altitude change. Advective fog, while equally transient, appears to be less frequently associated with major traffic incidents.

The bands of low atmospheric attenuation (high transmissivity) can be associated with a detector technology and wavelength. For example, the long wavelength infrared band and the millimeter-wave band provide relatively low attenuation windows with which to penetrate radiative fog. The millimeter-wave band appears to provide the lowest attenuation window in advective fog. These results follow the trends shown in Figure 7.5 for the extinction coefficients, where the advective fog has the larger extinction coefficient (larger attenuation).

Using MODTRAN, we evaluated transmissivity as a function of fog density, over the range of wavelengths detectable by the commercial infrared cameras that we tested. For simulation purposes, a path length of 1.0 km was used. Figure 7.10 illustrates a baseline “clear” condition.

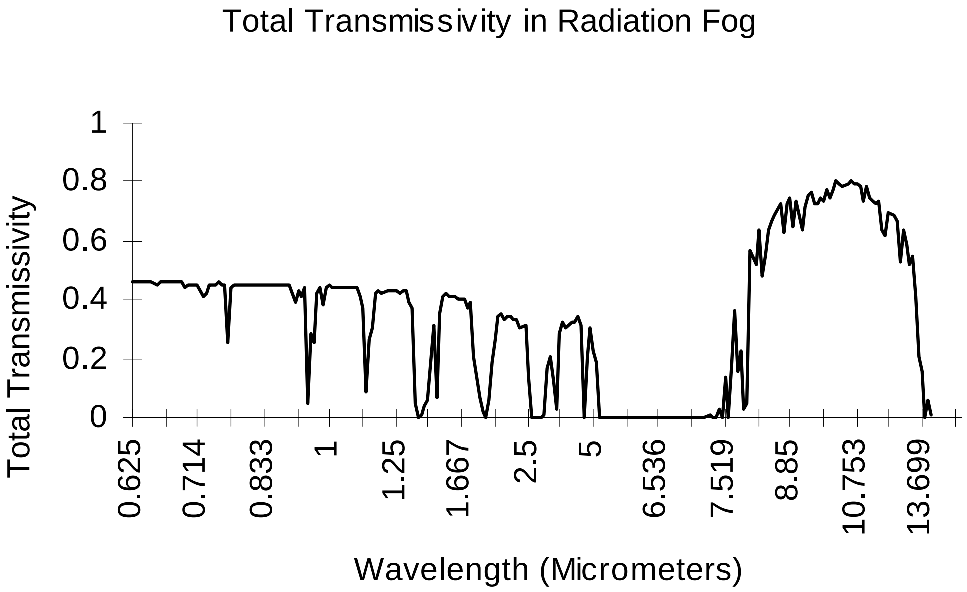

Figure 7.10 Visibility at 1 km through clear atmosphere, unlimited visibility.

Figure 7.11 shows the effect on visibility of radiation fog at a density such that an FAA visibility of 1.0 km would be reported. This would represent the official limit of visibility for usable perception of objects. Visibility is significantly attenuated in the visible through shortwave IR bands, while attenuation in the longwave IR band is minimal. Figure 7.12 shows the effect of very dense fog such that FAA visibility would be reported as 0.3 km. Over the 1.0 km path length, almost no visible and very little shortwave IR radiation arrives unscattered. Longwave IR penetrates under these conditions to an acceptable degree for useful perception. These results predict the superiority of longwave IR for vision in fog. However, energy emanating from the scene in the longwave IR band is generally less than in other bands, and is almost entirely attributable to blackbody emissions with negligible solar reflection.

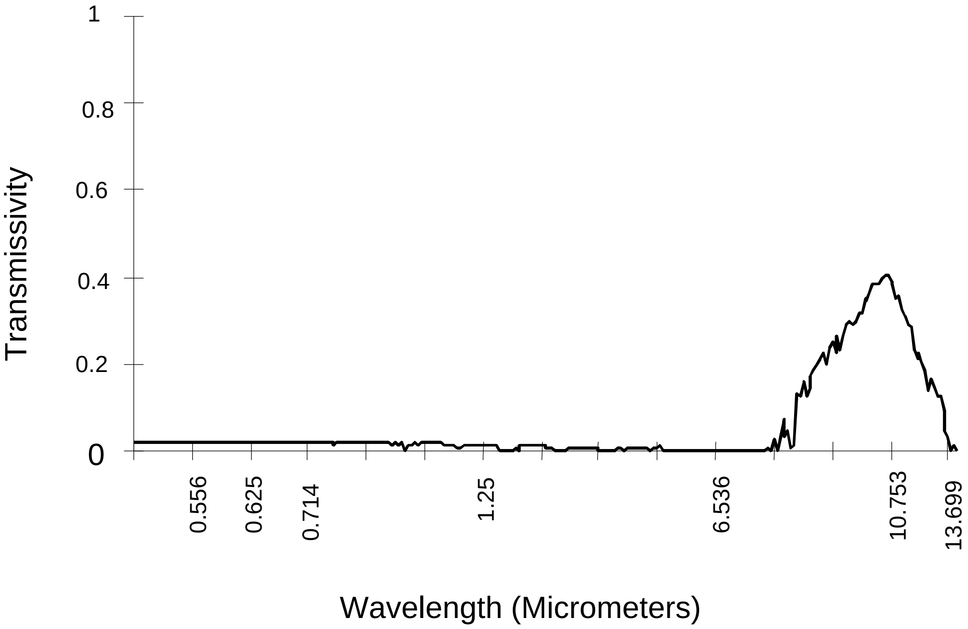

Figure 7.11 Visibility at 1 km Through Radiation Fog, 1 km Visibility.

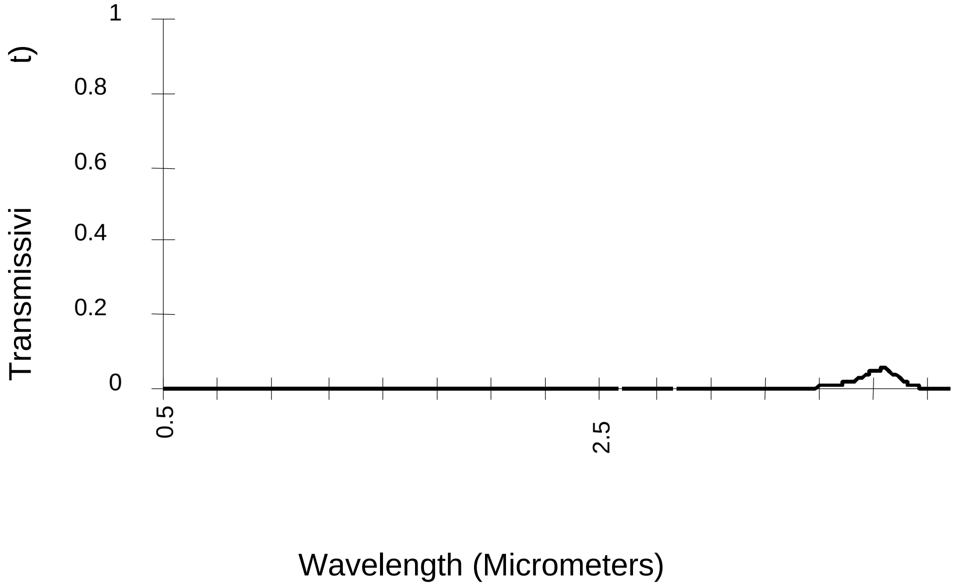

Figure 7.12 Visibility at 1 km Through Radiation Fog, 0.3 km Visibility.

8 Advanced Video Imaging Technologies

8.1 Visible Spectrum Imaging

A comprehensive study of closed-circuit television (CCTV) technology for highway surveillance was completed in 1990-1992 by the authors at the Transportation Electronics Laboratory, California Polytechnic University at San Luis Obispo, CA [31]. This study had five primary objectives:

- Assembly of a database of all commercial manufacturers and vendors of CCTV cameras suitable for traffic surveillance
- Establishment of test and evaluation criteria
- Video camera acquisition for testing
- Conducting of laboratory an field tests
- Data reduction.

One hundred eleven vendors were contacted and twenty-two monochrome and ten color camera were obtained for use in the project. Laboratory tests measured camera resolution, gray-scale reflectance, windows, linearity, registration, color calibration, sensitivity (signal-to-noise ratio), and blooming. Day and night field tests were conducted to qualitatively measure a CCTV camera's performance relative to other CCTV cameras and 35-mm photographs of the same scene viewed by the CCTV cameras under test. The photographs provided a standard against which all the CCTV cameras could be compared.

The most important performance factors for cameras used in highway surveillance are the resolution, sensitivity, and vertical smear. The horizontal resolution generally correlates with the amount of detail resolvable from the video signal generated by the camera. Vertical resolution is fixed by the Electronic Industry Association (EIA)32 or International Radio Consultative Committee (CCIR) specifications. Greater resolution implies that either (1) for a given angular resolution requirement, a larger area may be imaged, or (2) for a given image area requirement, a finer grain image may be discerned.

Sensitivity and dynamic range control the ability of the camera to detect objects under very low illumination conditions and the range of light levels than may be distinguished. Sensitivity is more important if features in the vehicle images must be discerned during nighttime conditions. Low sensitivity cameras will only be able to recognize headlights, whereas higher sensitivity cameras will be able to pick out the hood, roof, fender, and truck areas as well, for example.

Vertical smear causes a bright light source to drive the CCD into saturation. The result is a vertical white bar extending across the entire image. Therefore, the bright vertical rays from many headlights can potentially wash out an entire image.

The annual introduction of new camera models and improved specifications may have caused the two cameras recommended in this study to have been superceded by newer models or better performing, lower-cost units. Be that as it may, the monochrome camera highly recommended in 1992 was the Burle TC301 and the color camera highly recommended was the Cohu 8215.

8.2 CCTV Deployments as Aids to Traffic Management

Table 8.1 contains a list of states and cities that are currently using CCTV to support traffic management. Clearly, the use of CCTV for traffic management is increasing. The cameras are used to verify incidents, identify the assistance required to clear an incident, or operate in conjunction with video image processors to measure traffic flow parameters.

Table 8.1 Incident Management Programs that Use CCTV [33, 34, 35]

Location	Year Started	CCTV Status	Program	Number of Cameras
Statewide				
Arizona	1993	♦		No data
California	1970s	♦		No data
Connecticut	1992	♦		No data
Florida	1980s	♦	SMIS on I-4 near Orlando	No data
Maryland	1980s	♦	CHART	No data

Table 8.1 Incident Management Programs that Use CCTV (continued).

Location	Year Started	CCTV Status	Program	Number of Cameras
Missouri	1990s	♦		No data
New Jersey	1976	♦		No data
NJ Turnpike Authority	1996	♦		4
Pennsylvania	1997+	❑		5
Rhode Island	1997+	❑		No data
Virginia	1980s	♦		No data
Metropolitan Areas				
Atlanta	1990	♦		No data
Albuquerque	1997	❑	I-25/I-40 Interchange	*
Boston	1993	♦	I-93 SE Expressway, Central Artery/Tunnel	72
Charlotte	1991	♦		No data
Chicago	1960	♦	I-90/I-94 & CCTV Expansion Projects	13+
Dallas/Fort Worth	1970s	♦		No data
Denver	1991	♦		No data
Detroit + 3 counties	1992	♦		145
Fort Worth	1992	♦	Tarrant County	No data
Los Angeles	1970s	♦		≈100
Minneapolis/St Paul	1974	♦	Freeway Operations Program	181 now, 240 by 2000
Montreal	1994	♦	Montreal Freeway System	45
New York City	1985	♦		No data
Ottawa	1997	♦	Queensway Freeway	7
Phoenix	1997	♦	AZTech Model Deployment	55+
Sacramento	1993	♦		No data
Salt Lake City	1994	❑		No data
Seattle	1990s	♦	Northwest Region Traffic Map	35
Spokane	1997	❑	I-90	No data
Toronto	1985	♦	QEW Burlington Freeway	14
Toronto	1975	♦	QEW Mississauga Freeway	18
Toronto	1990	♦	Highway 401	59
Vancouver, B.C.	2001	❑	South Coast Region	63
Washington, D.C.	1989	♦		No data

♦ Current ❑ Planned * To be spaced at 1-mile intervals

8.3 Infrared Imaging

8.3.1 Energy Emission by Blackbody Objects in the Infrared Spectrum

The Planck radiation law describes the emission of energy at all wavelengths by blackbody (ideal emitter) objects with a temperature greater than absolute zero. In infrared applications, the emitted radiation may be calculated in terms of the spectral radiant excitance $M(\lambda,T)$ as a function of the wavelength at which the energy is measured and the temperature of the blackbody. In radiometric units of Watts per square centimeter of area and micrometer of wavelength, $M(\lambda,T)$ is a measure of the radiant flux or power density emitted by a surface and is given by [36]

$$M(\lambda,T) = \frac{2\pi hc^2}{\lambda^5(e^{hc/\lambda k_B T}-1)} \quad \frac{\mathrm{W}}{\mathrm{cm}^2\,\mu\mathrm{m}} \tag{8.1}$$

where

λ = emitted wavelength in μm,

T = absolute temperature of the blackbody in K,

h = Planck's constant = 6.6256176 x 10^{-34} W sec^2 or J sec,

c = speed of light = 3 x 10^{10} cm/sec,

and

k_B = Boltzmann's constant = 1.380662 x 10^{-23} J K^{-1}.

The total flux density over a wavelength interval λ_1 to λ_2 is obtained by integrating (8.1) over the interval as

$$\int_{\lambda_1}^{\lambda_2} M(T)\,d\lambda = \int_{\lambda_1}^{\lambda_2} \frac{2\pi hc^2}{\lambda^5(e^{hc/\lambda k_B T}-1)}\,d\lambda \quad \frac{\mathrm{W}}{\mathrm{cm}^2}. \tag{8.2}$$

Substituting

$$c = \lambda f \tag{8.3}$$

and

$$d\lambda = \frac{-\lambda^2 df}{c} \tag{8.4}$$

allows the emitted power density given by (8.1) to be rewritten as a function of frequency in Hz as

$$M(f,T) = \frac{2\pi hf^3}{c^2(e^{hf/k_B T}-1)}. \tag{8.5}$$

The minus sign in (8.4) reflects the usual inverse relation between wavelength and frequency.

The exitance expressed by (8.1) is plotted in Figure 8.1 for several blackbody temperatures. Cooler objects such as those at room temperature maximize their emitted power in the far infrared as illustrated in the figure. As the temperature of the object increases, the emitted power peaks at shorter wavelengths.

For a given blackbody temperature, the wavelength at which maximum power is emitted is found by differentiating (8.1) with respect to wavelength. This operation leads to

$$e^{hc/\lambda_m k_B T}\left(1-\frac{hc}{5\lambda_m k_B T}\right)=1. \qquad (8.6)$$

One solution of (8.6) is $hc/\lambda_m k_B T = 0$. But this implies that $\lambda_m T$ equals infinity and hence is of no practical interest. Returning to (8.6) and solving for its other solution leads to

$$\frac{hc}{k_B \lambda_m T} = 4.965. \qquad (8.7)$$

Upon inserting the values for h, c, and k_B into (8.7), we get Wein's displacement law for the wavelength at which the maximum power density occurs as

$$\lambda_m T = 2897.8\ \mu\text{m K}. \qquad (8.8)$$

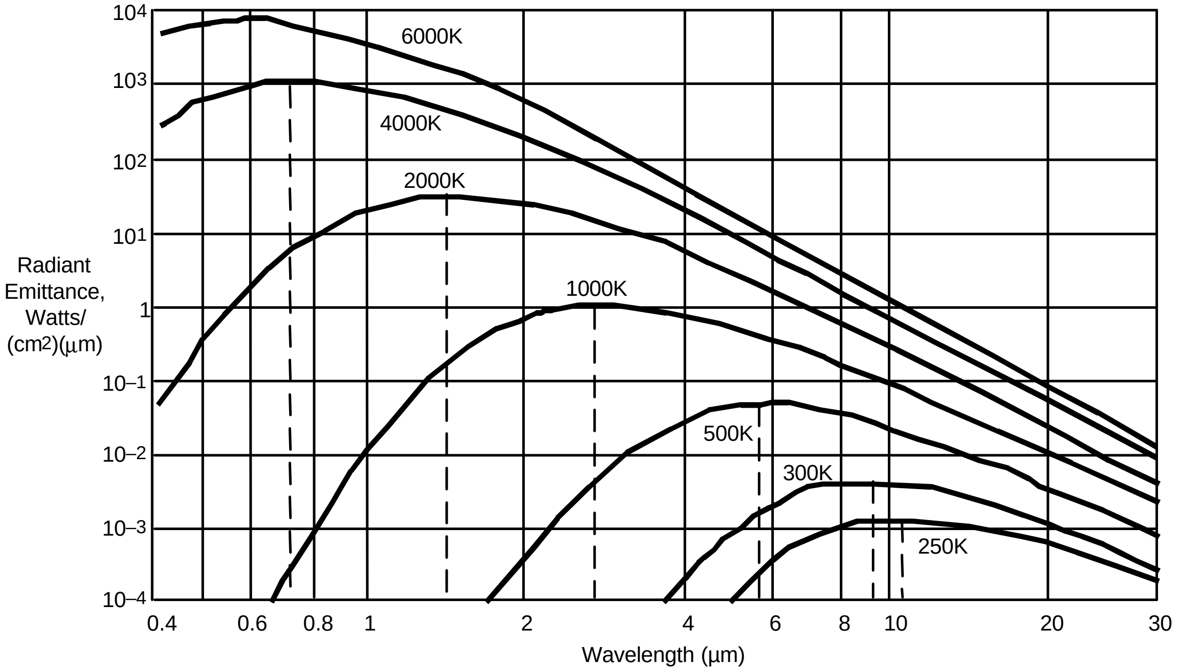

Figure 8.1 Blackbody emittance as predicted by Planck's radiation law.

Thus signatures from hot exhaust gases from vehicles peak in the near to mid infrared, while thermal emission from sunlight-loaded surfaces and surfaces indirectly heated by hot internal combustion engines peak in the far infrared.

In the millimeter-wave spectrum where

$$h\,f << k_B T, \qquad (8.9)$$

(8.5) reduces to the Rayleigh-Jeans law given by

$$M(f,T) = \frac{2pf^{2}k_{B}T}{c^{2}}\ \frac{\mathrm{W}}{\mathrm{cm}^{2}\mathrm{Hz}}. \qquad (8.10)$$

This expression is explored further in this section in conjunction with millimeter-wave radiometer imaging. There the units of the emitted radiation are given in terms of energy per unit volume per unit frequency interval, rather than power density per unit surface area per frequency interval.

The difference between visible wavelength sensors that detect light reflected from objects and infrared wavelength sensors that detect energy emitted by objects is illustrated in Figure 8.2. The upper part of the figure shows how an object uses sunlight to reflect energy and create a visible image that is seen by a human eye. The lower part of the figure depicts blackbody emission of energy by a "warm" object. The emitted energy is a function of the surface temperature of the object and its emissivity. This type of energy can be detected by an infrared sensor. Since an ideal blackbody emitter radiates energy at all frequencies, a portion of the emitted energy can also be detected by millimeter-wave radiometers, as was demonstrated with the 94 GHz Multispectral Scanner described later in this report.

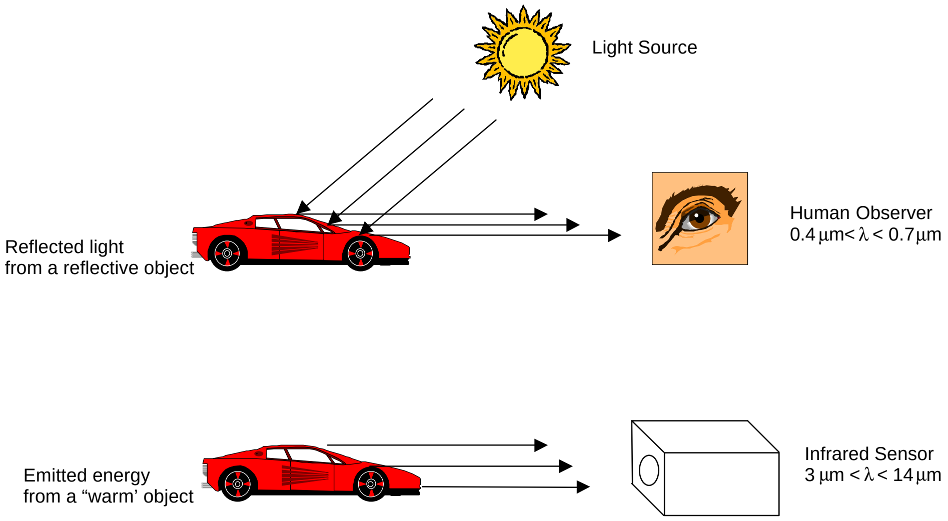

Figure 8.2 Detection of visible and infrared energy with appropriate sensors.

8.3.2 *Infrared Detection*

Passive infrared (IR) sensors detect energy emitted from targets, backgrounds, and the atmosphere in applications that include military surveillance, missile guidance and target detection, crop and forest management, weather forecasting, and vehicular traffic management. One class of infrared sensor, the forward-looking infrared (FLIR), provides high-resolution real-time imagery of a scene that has been historically displayed on a monitor. FLIR imagers employ either mechanically raster scanning or two-dimensional arrays of pixels (picture elements) having a small instantaneous field of view (IFOV). FLIR imagers have traditionally been used in support of security and surveillance, military target detection and classification, and false target and countermeasure rejection. FLIRs may have the potential to support traffic management by supplying operations personnel with imagery about traffic flow under conditions when visible spectrum CCTV may be ineffective, such as in poor visibility conditions.

Another class of sensor, the infrared search and track (IRST), locates and tracks objects by capturing the energy emitted within the field of view of the sensor. This is not an imaging sensor. IRST sensors are designed to operate with a small noise-equivalent temperature difference (NEΔT) so that small target-to-background contrast temperatures can be detected. Therefore, their performance is enhanced with designs that incorporate a large instantaneous field of view (since NEΔT is inversely proportional to IFOV). IRSTs often scan a 360-degree hemisphere in azimuth and 50 to 90 degrees in elevation for some airborne systems. Therefore, their total search area can be much larger than for FLIRs. The large number of scene pixels encountered by an IRST device requires computer-controlled data processing to separate the large number of false targets from the true targets.

A third class of infrared sensors is the infrared radiometer. It combines the functional attributes of FLIR and IRST sensors in that it may provide imagery of a scene containing small noise-equivalent temperature differences. By using filters to channelize the received energy into narrow wavelength bands, weather phenomena such as the altitude of cloud top heights can be determined from radiometers onboard space-based satellites. Still other space-based hyperspectral radiometer sensors divide the visible and infrared spectrum into hundreds of 10 nm to 20 nm narrow spectral bands. These sensors employ signal processing that combines the narrow spectral band data to aid in identification of geologic, ocean, soil, vegetation, atmospheric, and snow/ice boundary features.

Generally, the operating spectral band is chosen in a wavelength region where a strong image signature exists, although consideration must also be given to interfering background and atmospheric radiation and absorption that may be present. Infrared transmission bands that have relatively small atmospheric attenuation were shown in Figure 7.2. They include the short-wavelength infrared (SWIR) typically extending from 0.87 to 1.5 μm, mid-wavelength infrared (MWIR) from 3 to 5 μm, and long-wavelength infrared (LWIR) from 8 to ≥12 μm. The band limits are often adjusted for specific applications. Focal plane detector selection is usually based on the specific detectivity of the detector material (which is inversely proportional to noise equivalent power), cooling temperature required to achieve a satisfactory signal-to-noise ratio, cost of the array material, and the number and size of the pixels in the array needed to meet the resolution, spatial frequency, and field of view requirements of the application. Signal processing is driven by the required level of target discrimination. As object discrimination increases from detection through identification, more pixels must intercept the target or the signal-to-noise ratio must be increased to keep the probability of correct discrimination the same. The system design process is an iterative one where the goals are compared with the performance of the hardware and signal processing and the sensor cost.

In the generalized IR sensor block diagram of Figure 8.3, incident IR energy is shown entering through a window on the left. The window material is selected to transmit the wavelengths of interest and withstand the environment in which the sensor operates. The optics consist of one or more lenses that focus the energy onto the focal plane. Lower cost IR sensors generally have fewer optical elements in the lens subassembly.

The optics may be coated with spectral filters to restrict transmission of unwanted wavelengths or the filters may be located on the focal plane. In some semiconductor sensors, the detector array is mounted on a cooled focal plane to improve the signal-to-noise ratio by decreasing the electronic noise. Multiplexers may also be placed on the focal plane to minimize the number of connections leaving the focal plane.

In Figure 8.3, the detector output data are analyzed in a digital signal processor where the detection, classification, identification, and tracking information for an object are extracted. When used as part of a multiple sensor system, processed IR sensor data may be input to a data fusion algorithm where they are combined with data from other sensors to improve detection probability, classification, or tracking.

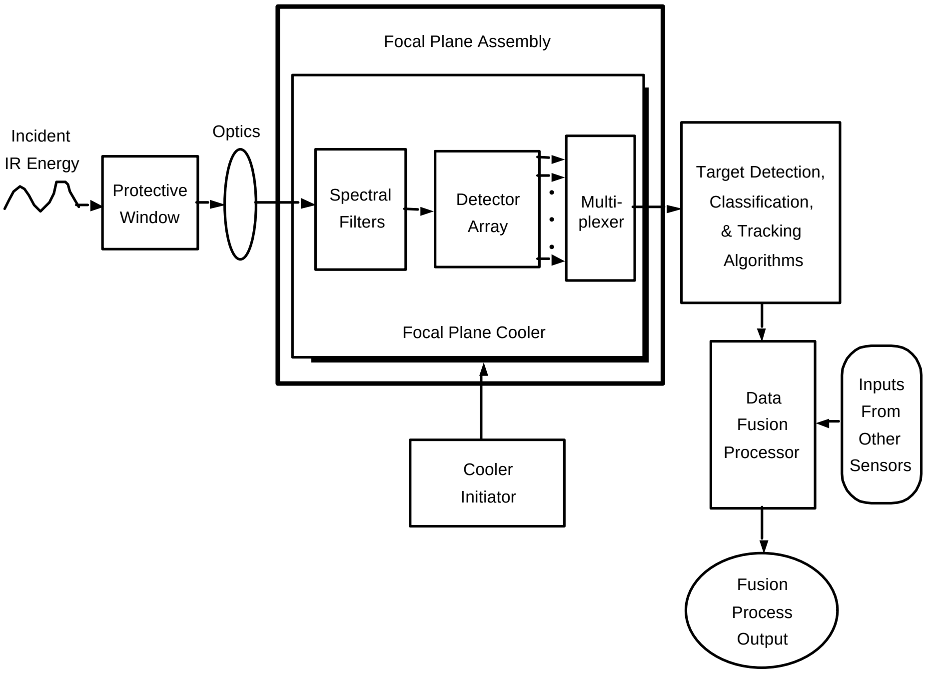

Figure 8.3 Passive infrared sensor (notional).

Commercially available imaging IR sensors fall into the FLIR and radiometer classes described above. An electronic signal representative of an image can be transduced by focusing, with appropriate optics, the IR image upon a rectangular array of detector elements. Mechanizations of this type are known as "staring arrays" or "Focal Plane Arrays". Focal plane array imagers operate in basically the same manner as conventional visible spectrum CCD video cameras. Figure 8.4 below illustrates the principle of operation of an IR focal plane array imager.

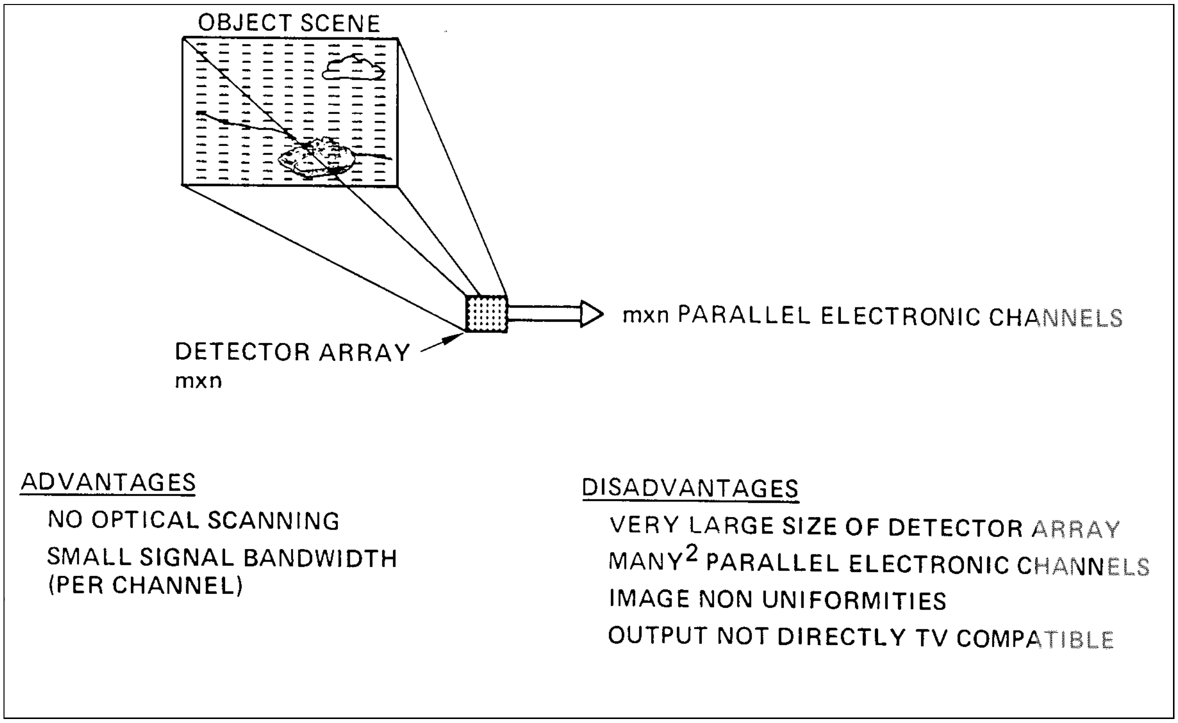

Figure 8.4 Principle of Operation, Infrared Focal Plane Array (Courtesy of Hughes Missile Systems Division).

The other method used in commercially available IR imagers is the mechanical scanning of a focused image upon a single detector element or a linear array of elements. Piezo-electric driven high-speed mirrors or rotating optical elements are used to focus a moving point in the image upon the fixed detector element. In this study, we refer to imaging devices that operate in this manner as "mechanically-scanned" imagers. Figure 8.5 illustrates the principle operation of a mechanically scanned IR imager.

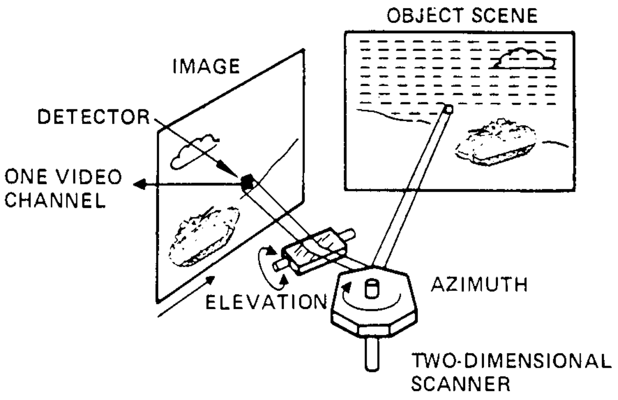

ADVANTAGES
- SMALL APERTURE SCANNER, DEWAR, DETECTOR
- MINIMUM NUMBER OF ELECTRONIC CHANNELS
- IMAGE UNIFORMITY, REFERENCE LEVEL
- OUTPUT DIRECTLY TV COMPATIBLE

DISADVANTAGES
- HIGH SCAN SPEED
- LARGE SIGNAL BANDWIDTH

Figure 8.5 Principle of Operation, Mechanically Scanned Infrared Imager (Courtesy of Hughes Missile Systems Division).

Another, and possibly the most important division of technologies with respect to practicality for highway use, is the operational temperature requirement for the focal plane on which the detector array is mounted. Some IR imagers must operate their focal planes at cryogenic temperatures, typically 77 degrees Kelvin, while others can operate at room temperature (≈ 298 degrees Kelvin). Generally, the noise performance of cooled sensors is superior to that of uncooled sensors. The cryogenic cooling requirement, however, makes camera technologies based upon cooled sensors much more expensive and much less reliable in terms of the mean time between failures (MTBF). The cooling requirements for several common semiconductor detectors and their operating principles are discussed below.

A wide range of semiconductors are capable of detecting radiation in various IR bands. Except for very early experimental devices, all state-of-the-art detectors operating beyond the near-IR band are composed of compound semiconductors, which are alloys of elements found in Periodic Table of Elements columns 3 and 5. While it is beyond the scope of this report to fully describe the operational principles of each type of detector, summary descriptions of several are provided below.

8.3.3 Quantum Detectors

Quantum detectors are found in a wide variety of military applications because of their relatively high sensitivity to thermal energy, which is greater than that of the bolometers and pyrolectric detectors dicusssed later in this section. Quantum detectors include photoemissive, photoconductive, and photovoltaic materials. Since photon energy is inversely proportional to wavelength, the minimum photon energy required to produce a charge carrier determines the maximum wavelength to which a quantum detecor will respond. Response to minimum wavelengths (higher energy photons) is limited by the ability of the detector material to absorb or stop the photons. The maximum and minimum constraints on the wavelengths absorbed by a quantum detector restrict quantum detector operation to a relatively narrow spectral region.

Photoemissive devices require photons to possess sufficient energy to produce free electrons that escape from the material. They are typically enclosed in a vacuum tube and respond to relatively high energy photons at visible and ultraviolet wavelengths.

Photoconductive (PC) detectors are high impedance semiconductors whose conductance is increased when absorbed photons produce free charge carriers in the material. Photoconductive quantum detectors can be intrinsic or extrinsic devices. Intrinsic PC semiconductors absorb photons with enough energy to cause an electron to jump from the valance band, across the bandgap, and into the conduction band. These photons generate both free electrons and holes. Intrinsic detectors require materials to have the proper bandgap for the desires spectra response. Extrinsic photoconductors are majority carrier devices that are doped with an element that creates an ionization level that lies in the bandgap between the valance band and conduction band. Photons with energies greater than the ionization level of the impurity are absorbed, creating one free carrier (either an electron or a hole) and an ionized impurity site (either a bound hole or a bound electron). Since the ionization energy is less than the bandgap energy, less energetic photons can be absorbed by extrinsic materials. This shifts their operation to longer wavelengths.

Photovoltaic (PV) detectors are low impedance, intrinsic semiconductors that do not require an external bias voltage to operate. As with a photoconductor, the spectral sensitivity of a PV detector is determined by the energy levels in the semiconductor material [14].

Mercury Cadmium Telluride

Mercury-cadmium-telluride (HgCdTe) is a tertiary compound quantum detector that is most often operated at 77 K. It has a relatively small time constant that enables it to respond to the rapidly changing temperatures of objects in its field of view or to be used in scanning sensors. By varying the relative proportions of the elements in the detector material, it is possible to tailor the wavelength at which the peak spectral response occurs to either the MWIR or LWIR. Most often HgCdTe is used at LWIR wavelengths. HgCdTe is produced in large arrays that make it suitable for starring sensor applications. The commercial cameras with HgCdTe arrays evaluated as part of this project were the AGEMA Thermovision, Inframetrics 600 LWIR band, and the Inframetrics 760. A summary of the HgCdTe operating characteristics is given in Table 8.2 as are those of the other materials discussed below.

Included in the table is the specific detector detectivity, D_d*. It is one of the primary parameters used to characterize detector materials. Detector detectivity is equal to the reciprocal of the noise equivalent power (NEP) of the detector. NEP is the incident power at the detector input required to produce a root mean square signal-to-noise ratio of unity at the detector output for a specified frequency bandwidth. The specific detector detectivity is equal to the detector detectivity normalized to the detector area (usually assumed to be 1 cm^2) and electrical bandwidth of the processing electronics (usually assumed to be 1 Hz in the specifications).

Table 8.2 Operating parameters (typical) of selected intrinsic quantum detectors [37].

Material	Operating Mode	Focal Plane Temp. (K)	Time Constant (µs)	Peak Wavelength (µm)	Usable Wavelength Region (µm)	D_d* at 500 K (cm Hz$^{1/2}$ W^{-1})
PbS	PC	300	>100	2.4	1.1 to 3.5	10^{11}
PbS	PC	195	500	2.8	No data	$\approx 5 \times 10^{11}$
PbSe	PC	300	1 to 5	3.9	1 to 5.0	$\approx 10^{10}$
PbSe	PC	195	10 to 40	4.8	2 to 5.0	3.5×10^{10}
PtSi	Schottky barrier	<90	$\approx 10^3$	0.9	0.8 to 5	2×10^9
InSb	PV	77	0.1 to 2	4.9	2 to 5.5	7×10^{10}
HgCdTe	PV	195	≈ 2	4.5	1 to 5.5	4×10^{10}
HgCdTe	PC	77	0.1 to 2	10.5	8 to 14	2.5×10^{10}

Platinum Silicide

Platinum silicide (PtSi) is a MWIR material used most frequently to produce low, cost high performance starring arrays for military applications. The detector material is cooled to <90 K to achieve optimal operation. Arrays of 490 x 650 pixels have been produced. The commercial PtSi cameras evaluated during this project were the Mitsubishi M300 (256 x 256 pixels), FSI Prism DS (320 x 244 pixels), Inframetrics 600 MWIR wavelength band, and Inframetrics InfraCam (256 x 256 pixels). Another Mitsubishi model with a 512 x 512 PtSi array is also manufactured.

Indium Antimonide

Indium antimonide (InSb) is another MWIR material used frequently in MWIR military starring array applications. It achieves optimum operation at temperatures approaching 77 K. Some commercial IR cameras use InSb arrays. These include the Cincinnati Electronics IRRIS-256ST (256 x 256 pixels) evaluated as part of this project and cameras manufactured by Amber (that were not available during the period this project was conducted).

Lead Salts

The lead salts include lead sulfide (PbS) and lead selenide (PbSe). They are MWIR materials that have relatively high sensitivity at room temperature. PbSe has a smaller time constant than PbS and can, therefore, respond to more rapidly changing scene temperatures or be used in scanning applications.

8.3.4 Microbolometers

Microbolometers are a relatively new type of imaging array made of silicon that requires no cooling [38]. This lower-cost technology is expected to result in new applications such as fog detectors. Unlike imaging arrays that are based on photon detection and require cooling for optimum performance, the bolometer array consists of pixels that measure temperature changes induced by incident thermal radiation. The temperature is sensed by the strong temperature dependence of the bolometer's electrical resistance. The sensitivity band can be maximized to long wavelength infrared (8 to 14 µm) by properly coating the window through which energy is transmitted to the focal plane array.

Honeywell developed the bolometer technology in the early 1990s. The Boeing North American (formerly Rockwell) Electro-Optical Center (EOC) licensed this technology from Honeywell and makes a commercially available microbolometer focal plane on a merchant supplier basis. The focal plane output can be externally controlled to comply with both U.S. and PAL television synchronization standards.

The noise equivalent temperature difference (NEΔT) is the performance measure most often used to compare photon detector arrays with bolometer arrays. NEΔT is the temperature difference between an object and the background that will produce a signal-to-noise ratio of unity. NEΔT is directly proportional to the f-number (hence, inversely proportional to the speed of the optics). With f/1 optics, the current generation of microbolometer arrays has NEΔTs of approximately 0.1 K at 30 frames/s. NEΔT is expected to decrease to 0.03 to 0.05 K as newer technology advances are incorporated into the arrays. By comparison a cooled PtSi array has a NEΔT of 0.05 K and a cooled HgCdTe or InSb array a NEΔT of 0.025 K. However, the NEΔT of the microbolometer is sufficiently low for many applications such as surveillance, night vision, fire fighting, and detection of vehicles in fog.

Because microbolometer technology is monolithic, unlike laminated or bump-bonded photon arrays, it is rugged. The microbolometer technology has been subjected to forces exceeding 10,000 g with no adverse effects on performance. Improvements in microbolometer technology are expected to bring increased sensitivity (lower NEΔT) or lowered cost by keeping the current sensitivity and using less expensive f/2 optics.

We tested only one camera based upon bolometer technology, the GEC/Marconi Sentry IR20, a handheld camera with a PAL video output format. The GEC/Marconi Sentry IR20 contains an uncooled focal plane with an effective 200 x 200-pixel array that covers the 8-14 μm spectral region. The detector material used by GEC/Marconi was modified lead zirconite (PbZr). A 100 mm lens, having an 5.65-deg x 5.65-deg field of view, was used with the camera.

8.3.5 Pyroelectric Detectors

Possibly the most practical among current technology longwave IR cameras are classified as pyroelectric sensors. These are uncooled imaging detectors that operate by measuring the change in the polarization of the detecting material that is induced by the change in the power incident on the detector from the observed scene. Pyroelectric detectors consist of a thin layer of ferroelectric material sandwiched between two electrodes to form a capacitor. Since ferroelectric materials exhibit a spontaneous polarization that is temperature sensitive, the pyroelectric detector functions as a temperature-sensitive capacitor. Pyroelectrics do not require a bias voltage. They produce an output voltage proportional to the time rate of change of the temperature and not to the temperature itself. The response of pyroelectrics can be faster than that of bolometers. A comparison of several properties of bolometers and pyrolectrics in given in Table 8.3. Note that the time constant is now in milliseconds rather than microseconds as with the quantum detectors. Also, the D_d* value is generally smaller than that found in the cooled focal plane quantum detectors. The pyroelectric cameras used in this project were the Insight StarSight 8-14 μm and the TI Nightsight C100 8-14 μm.

The Insight IR camera is manufacturered in England, and appeared to no longer be in production or supported by the manufacturer. We therefore could only obtain limited specifications for it from the operator's manual. Texas Instruments (TI) of Dallas TX. in cooperation with Hughes Aircraft Company of Los Angeles, CA uses a barium strontium titanate (BST) focal plane to manufacture the Nightsight Camera. The focal plane contains 80,000 pixels (245 x 328) in the 8 to 14 μm band. Two versions of this camera was used in the project: one a military-issue device and later commercial model.

Table 8.3 Operating parameters (typical) of bolometer and pyroelectric detectors [37].

Material	**Focal Plane Temp. (K)**	**Time Constant (ms)**	**Usable Wavelength Region (μm)**	**D_d* at 500 K (cm $Hz^{1/2}$ W^{-1})**
Bolometers	300	1 to 100	0.8 to 40	<1.5 x 10^9
Pyrolelectrics	300	0.1 to 100	0.6 to 35	≤8 x 10^8

8.4 Millimeter-Wave Imaging

Imaging at radio frequencies is a more recent innovation, although the basic phenomena has been understood for decades. Passive millimeter-wave (MMW) sensors receive energy that is emitted or transmitted from other sources. In space exploration projects, they find use as receivers for collecting radiation and signals from distant stars and galaxies. Radiometers operating in the microwave and millimeter-wave spectrum are placed on weather satellites to provide atmospheric temperature and water vapor profiles. These data find use in weather forecasting for civilian and military applications. In transportation applications, they are used to detect and provide imagery of vehicles. Their long wavelength (as compared to infrared radiation) allows the reception and identification of energy emitted by a vehicle in clear and inclement weather, including fog.

Images can be formed using natural emissions from scenes at radio, microwave, and millimeter wavelengths, in a manner highly analogous to a CCD camera operating in the visible range. Radiation from the scene nay be either mechanically raster scanned or focused on a focal plane array by an optical element, which may be either a parabolic reflector (as in a reflector-type optical telescope) or a transmissive optic, which functions exactly the same way as a lens. Because of the differences in wavelength, different materials are used to make the lens than would be the case for optical radiation. At 94 GHz, for example, typical lens materials are Teflon and Rexolite, the former being opaque and the

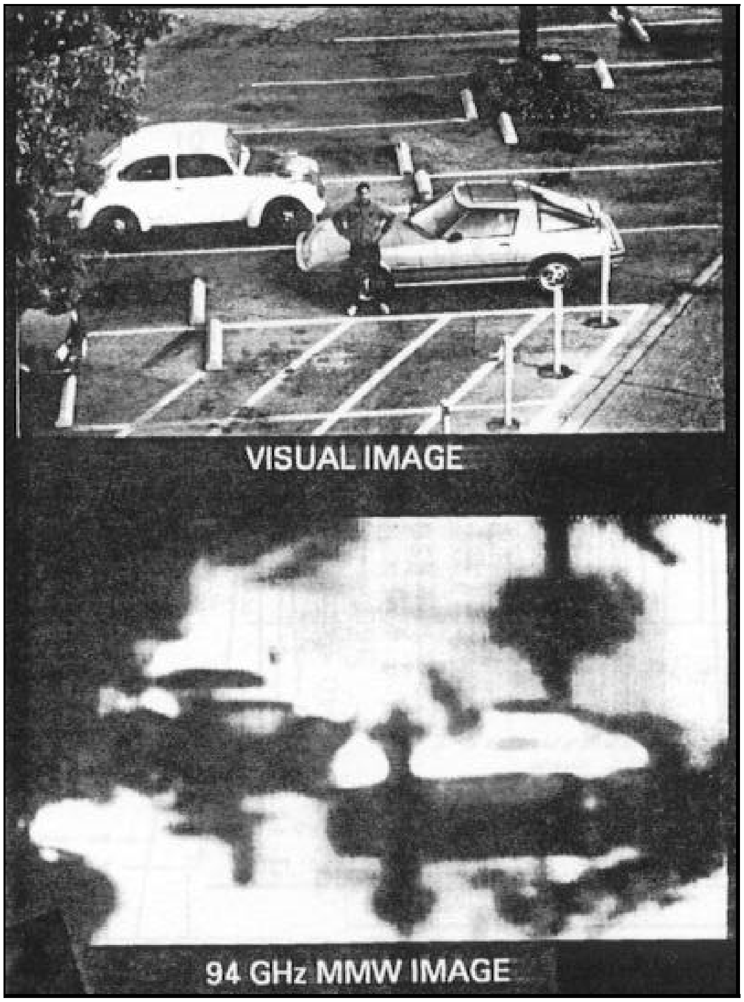

Figure 8.6 Passive 94 GHz Millimeter Wave Static Image of Vehicle and Person Against Asphalt Background, Taken with TRW Multispectral Scanner.

latter translucent to visible radiation. The signal generated by each detection element(s) represents the intensity for a single pixel in the image. When these intensities are displayed on a video monitor, a visual-like, literal image appears which is easily interpreted by an untrained observer.

Figure 8.6 shows a static image of an automobile and person from a distance of approximately 25 meters, created with the TRW Multispectral Scanner operated at 94 GHz. The resolution limitation is obvious.

Of primary concern in this study is the ability to penetrate atmospheric conditions that would otherwise obscure visible imaging. If the wavelength of observation for the millimeter wave camera is chosen to correspond to on of these windows of high atmospheric transmission (for example, at 35 or 94 GHz) the images have the striking characteristics shown in Figure 8.7, an airborne image of Long Beach Harbor, taken with the TRW Multispectral scanner by TRW personnel.

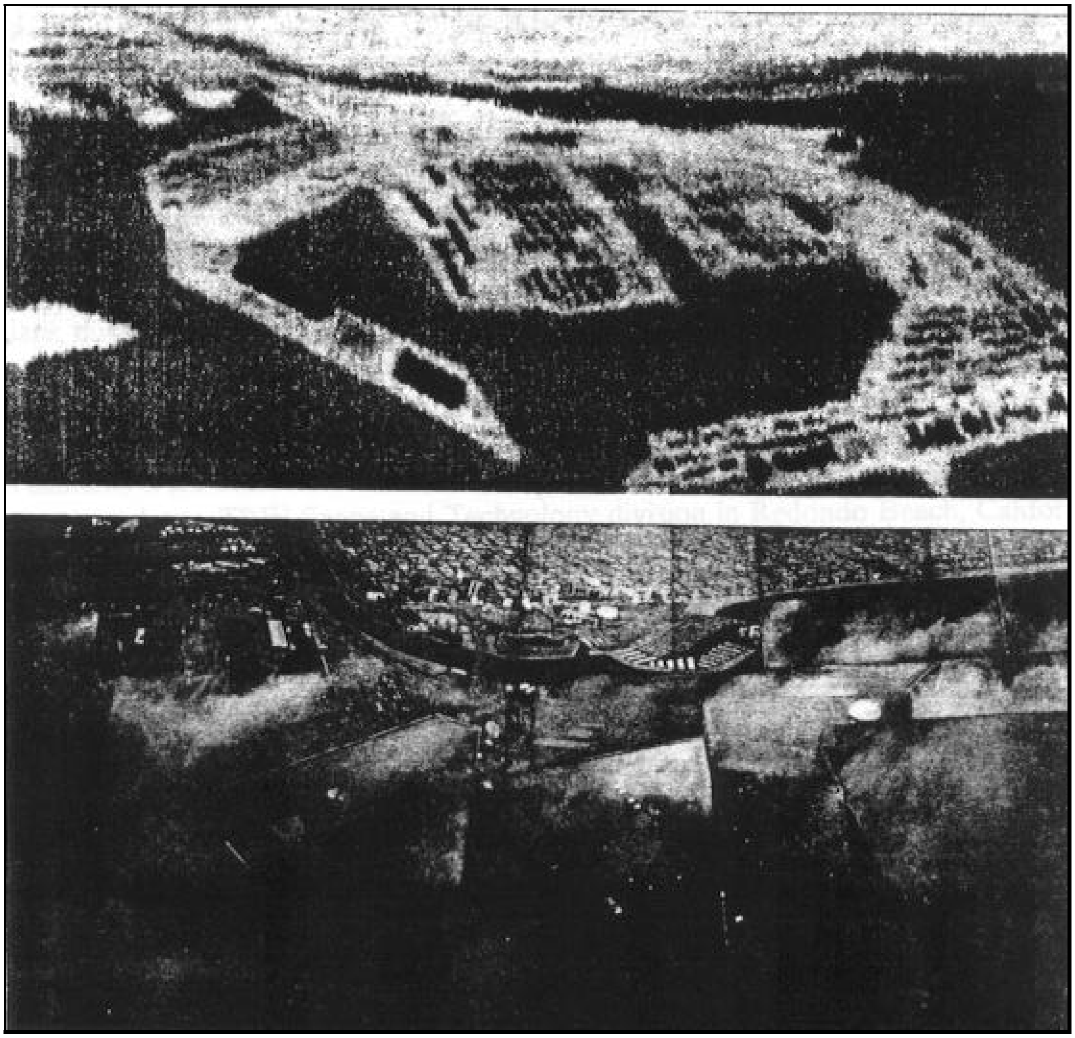

Figure 8.7 Airborne Millimeter Wave Image (above) and Visible Spectrum Image (below) of Long Beach Harbor, both Composites of Several Scans Taken with TRW Multispectral Scanner at 94 GHz.

Metallic objects (buildings, ships, freight containers, spatially resolved vehicles) stand out as dark objects against a bright background, and the clutter present in a visible image of the scene (bottom) is absent.

This happens because the metallic objects specularly reflect the sky into the sensor. At 94 GHz, the sky temperature is typically a few tens of degrees Kelvin. Rough, natural background textures tend to be highly emissive, and radiate energy at an effective temperature of about 300 K, thus appearing to be much "hotter" than the metallic objects. Water, which is intermediate in reflectivity, appears as an intermediate shade of gray. Further, since the wavelengths are long compared with the size of suspended water droplets or other aerosols, the 94 GHz image is unaffected by the presence of the clouds in the image. Phenomenology and image properties are essentially unchanged for daytime or nighttime viewing.

The simple nature of these images makes them particularly suitable for automated feature extraction/image interpretation. It should be pointed out, however, that the contrast between metallic objects and their background depends on the shape of the object and the angle of the line of sight from nadir. For horizontal viewing, vertical surfaces are harder to see than surfaces inclined at a slight angle, which will reflect a higher angle view of the sky.

Disadvantages for this kind of imaging system include the physical size of the scanner, or for a focal plane array, the optics required for imaging. To produce a 94 Ghz diffraction limited image with a 2 foot resolution at 100 feet requires a lens (or reflector) diameter of about 6 inches.

A second disadvantage is the relative immaturity of the sensor hardware. TRW and Hughes Aircraft have been developing these sensors over the last several years and have progressed from the initial capability, which used a single detector string which is mechanically scanned to image slowly moving scenes, to small staring arrays which can image small area (or low resolution) scenes at near-video refresh rates. Recent developments using GaAs MIMIC (Millimeter/Microwave Integrated Circuit) technology has shown that it is possible to fabricate each receiver chain on a few (typically three) integrated circuits which are combined in a fine-line configuration to produce a lower cost pixel. This new MIMIC configuration has an additional advantage since it directly amplifies the incoming radiation using a 94 Ghz LNA. The earlier configurations, embodied by the TRW Mulspectral Scannner used in our tests, used heterodyne mixing to convert the incoming signal to the few Ghz range where conventional LNAs are available. Thus the new configuration avoids the complexity of the local oscillator bank required for the earlier configurations.

The passive millimeter wave sensors under development to date have been in support of applications which are more tolerant of high sensor costs than are transportation systems. These arrays, at production rates expected for these low volume markets, are expected to cost in the low tens of dollars per pixel. Given time, a significantly larger market, and an increased focus on cost reduction, it is expected that the cost of a large pixel-count focal plane array (the dominant cost component in wide field passive millimeter wave cameras) will become more cost competitive with more mature imaging systems.

8.4.1 Planck Radiation Law

Blackbody objects (i.e., perfect emitters of energy) not at absolute zero emit energy *E* per unit volume and per unit frequency at all wavelengths according to the Planck radiation law given by

$$E = \frac{8\pi h f^3}{c^3} \frac{1}{exp(\frac{hf}{k_B T}) - 1} \; \frac{\mathrm{J}}{\mathrm{m}^3\ \mathrm{Hz}}, \qquad (8.11)$$

where

h = Planck's constant = 6.626 x 10^{-34} J-sec,

k_B = Boltzmann's constant = 1.380662 x 10^{-23} J/K,

f = frequency at which radiation is measured in Hz,

c = speed of light = 3 x 10^8 m/sec,

and

T = temperature of radiating object in K.

Using the exponential series expansion for the exponential term in the denominator allows (8.11) to be rewritten as

$$E = \frac{8\mathrm{p}hf^3}{c^3} \frac{1}{\frac{hf}{k_B T} + (\frac{hf}{k_B T})^2 + ...} \ \frac{\mathrm{J}}{\mathrm{m}^3\ \mathrm{Hz}} . \qquad (8.12)$$

When only the linear term is retained, as when the operating frequency f is less than $k_B T/h$ ($\approx$ 6 x 10^{12} Hz), the Planck radiation law reduces to the Rayleigh-Jeans law given by

$$E = \frac{8\mathrm{p}f^2 k_B T}{c^3} \ \frac{\mathrm{J}}{\mathrm{m}^3\ \mathrm{Hz}} . \qquad (8.13)$$

Here temperature is directly proportional to the energy of the radiating object, making calibration of the radiometer simpler. With perfect emitters, or blackbodies, the physical temperature of the object (T) is equal to the brightness temperature T_B that is detected by a radiometer. However, the surfaces of real objects do not normally radiate as blackbodies, i.e., they are not 100% efficient in emitting the energy forecast by the Planck radiation law. To account for this, a multiplicative emissivity factor is added to represent the amount of energy that is radiated by the object, now referred to as a gray body. The emissivity is equal to the ratio of T_B to T.

Radiometers that detect objects measure the apparent temperature difference between the object and the background. Apparent temperature includes the energy emitted by a gray body object (one that is not a perfect emitter of energy at all frequencies), effects of antenna gain and side lobes, energy added by antenna self emission caused by losses, and noise reflected back into the receiver by mismatches in impedance between sensor components. In its simplest form, a radiometer receiver is similar to a pulse or frequency modulated continuous wave radar, with the exclusion of the transmitting components. It contains a low loss, narrow beam width antenna whose side lobes are minimized to restrict the energy that enters the receiver from areas other than the main beam; low noise figure mixer; wide bandwidth intermediate frequency amplifier; a second detector (also called the video detector); and a low-pass video amplifier that provides integration of the signal.

In traffic management applications, millimeter-wave radiometers can be used to detect metal vehicles such as automobiles and trucks. Their operating wavelengths make them suitable for detecting vehicles (e.g., the beam widths are appropriate to the vehicle size and the frequency can be chosen at an atmospheric window where emitted energy received from surface-based objects is maximized and emitted energy from the atmosphere is minimized) and for packaging within acceptable sized enclosures. In the millimeter-wave spectrum, atmospheric windows exist at 35, 94, 140, 225, and 350 GHz as shown in Figure 8.8. Because transportation vehicles are predominantly composed of metal, their emissivity is small and they reflect the downward emitted sky radiation. Since the sky radiation is generally less than the radiation from a road surface, a contrast exists between the energy sensed by the radiometer from the vehicle and road, making vehicle detection possible. The detected signal can be analyzed for features such as an intensity greater than a clutter-adaptive threshold, a pulse width corresponding to the vehicle size, or ratios of the above discriminants.

8.4.2 Vehicle-to-Road Surface Contrast

Passive millimeter-wave sensors use a low-noise, heterodyne receiver to measure the energy emitted by objects in the field of view of the sensor. They do not transmit energy of their own. The source of the emitted energy is gray body radiation due to the non-zero temperature of emissive objects as illustrated in Figure 8.9. When a vehicle enters the field of view, the change in emitted energy caused by the presence of the vehicle is used to detect the vehicle.

An equation can be written for the difference in energy corresponding to a road without vehicles and one with vehicles in the radiometer's field of view. The emissivity of the vehicle and road surface in the wavelength region of interest are denoted by e_V and e_R , respectively, and their surface temperatures in degrees Kelvin by T_V and T_R. The brightness temperature T_B of the vehicle, as sensed by the radiometer, is

$$T_B(q,f) = e_V T_V + (1 - e_V)\, T_{Sky} \tag{8.14}$$

assuming the vehicle fills the field of view of the antenna.

T_{Sky} is the sky temperature and is a function of atmospheric, cosmic, and galactic emission. The cosmic temperature, attributed to the background radiation produced when the universe was formed, is independent of frequency and viewing angle and is equal to 2.735 K. The galactic temperature is due to radiation from the Milky Way galaxy and is a function of viewing direction and frequency. Above about 10 GHz, it can be neglected in comparison with atmospheric emission. Atmospheric emission is affected by clouds, water vapor, rain, and certain gaseous components as shown in earlier diagrams. q and f are the incident angle with respect to nadir and the angle in the plane of the road surface (the *x*-*y* plane), respectively.

One can write a similar expression for the brightness temperature of the road surface as

$$T_B(q,f) = e_R T_R + (1 - e_R)\, T_{Sky} . \tag{8.15}$$

By subtracting the brightness temperature of the vehicle from that of the road, one gets an expression for the temperature difference $\Delta T_B(q,f)$ sensed by the passive radiometer when a vehicle passes through its field of view. Thus,

$$\Delta T_B(q,f) = (e_R - e_V)\, (T_R - T_{Sky}), \tag{8.16}$$

when $T_R = T_V$.

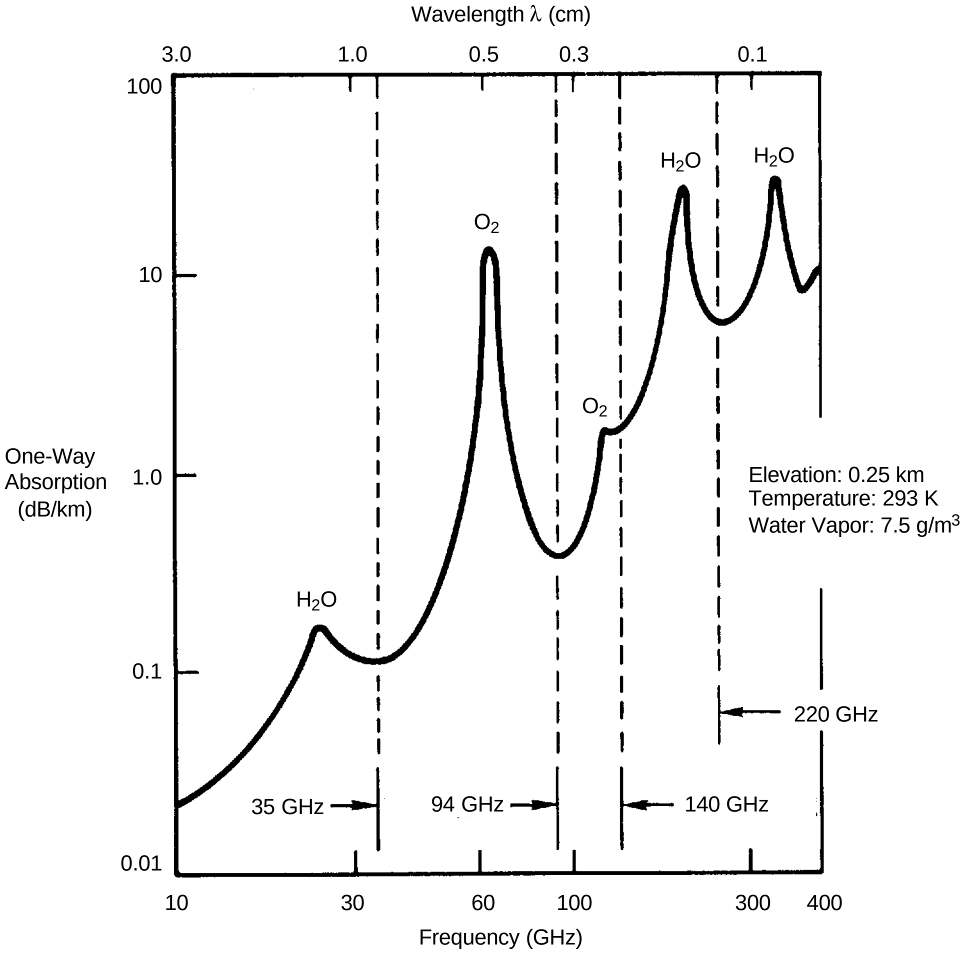

Figure 8.8 Regions of minimum and maximum atmospheric absorption in the MMW spectrum. Attenuation values are based on measured data [39, 40].

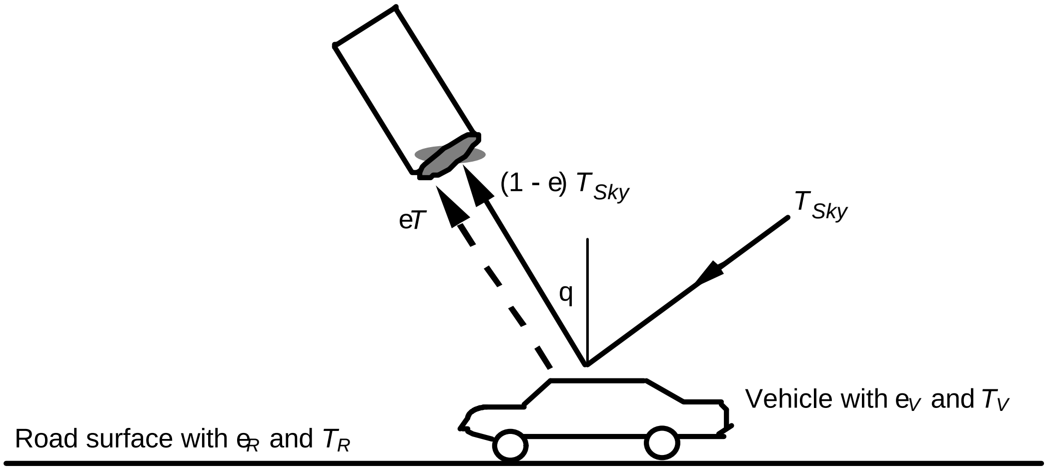

Figure 8.9 Emission of Energy by Vehicle and Road Surface

Hence, a vehicle generates a signal proportional to the product of the difference in emissivity between the road and the vehicle and the difference between the absolute temperature of the road surface and the sky temperature. On overcast, high humidity, and rainy days, the sky temperature is larger than on clear days and the signal produced by a passing vehicle decreases. This, in itself, may not pose a problem to a properly designed passive radiometer operating at a window frequency, especially at the relatively short operating ranges required for traffic management applications.

If the radiometer is not properly designed to minimize antenna side lobes or the ground footprint of the main lobe is larger than the vehicle, then extraneous energy from objects other than the vehicle of interest will enter the radiometer receiver. This energy will compete with the energy from the road or vehicle and will reduce the sensitivity of the radiometer to energy changes that occur when vehicles appear in the footprint of the antenna main lobe. Similarly, energy emitted by internal lossy receiver components and energy reflected between receiver components when impedance matches are not ideal will also reduce receiver sensitivity. However, even with all of these restrictions, radiometers can be designed to operate at millimeter wavelengths to detect vehicles on road surfaces.

One of the first millimeter wave “cameras” ever successfully operated is the TRW multispectral scanner which we tested in the present study. It is a passive millimeter-wave camera that can produce crude single-frame images, each requiring approximately 2 minutes to form, using a mechanically-scanned antenna [41]. A two-view diagram of this instrument is shown in Figure 8.10.

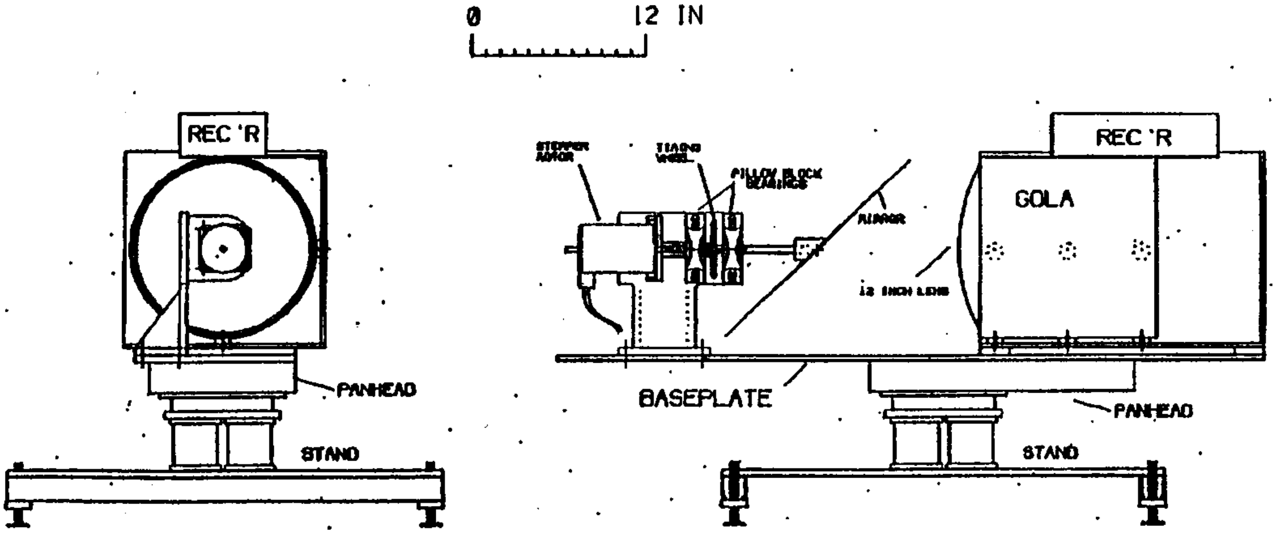

Figure 8.10 TRW 94 GHz Multispectral Scanner, As Tested in this Study.

The resolution and noise performance of this experimental imaging apparatus is understandably very poor, since it was designed for concept validation rather than high performance. A sense for these limitations is illustrated by Figure 8.11, which is a group photograph of Caltrans and Cal Poly personnel taken in the Transportation Electronics Laboratory during a December 1994 seminar and demonstration of advanced imaging technologies, conducted as one of the deliverables of this project. Nine standing persons are shown, although it would be impossible to recognize this from the image alone.

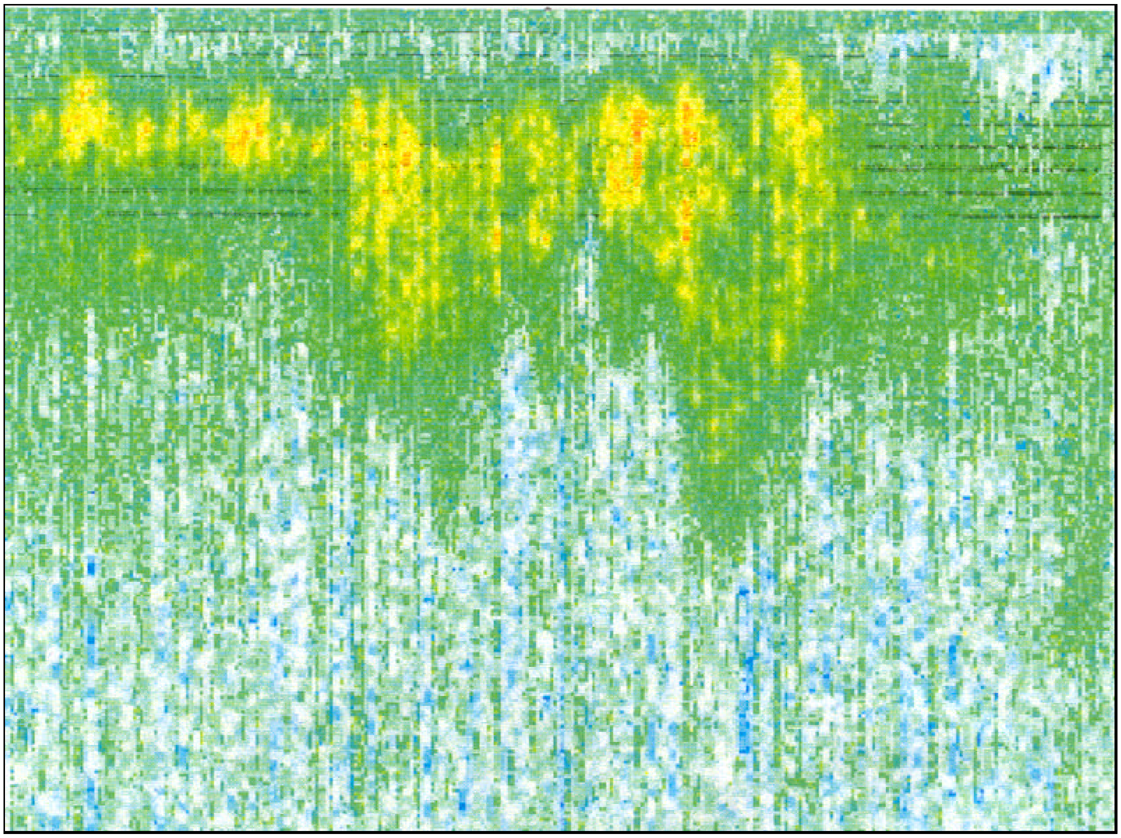

Figure 8.11 Group Photograph of Caltrans and Cal Poly Personal Taken with 94 GHz TRW Multispectral Scanner at Cal Poly, December 1994.

TRW is currently under contract to the DOD to produce a focal plane array millimeter wave camera, with the objective of imaging in real time through fog, smoke, and clouds as an airport landing aid [42]. The camera will operate at a center frequency of 90 GHz. The focal plane array of the camera will contain 1,040 monolithic millimeter-wave integrated circuit (MMIC) receiver chips, creating an 80 x 52 pixel image. Aperture deconvolution algorithms help display an image that refreshes 17 times a second and is equivalent to an effective aperture of 24 inches instead of the actual 18 inches. In aeronautical applications, the pilot sees an image of the forward scene raster scanned on a head-up display with overlays of flight guidance cues.

8.4.3 Absorption and Attenuation of Millimeter-Wave Energy by the Atmosphere

The major atmospheric effect on the performance of millimeter-wave sensors is attenuation due to absorption. Figure 8.8 shows the millimeter-wave window frequencies corresponding to relative absorption minima and the frequencies at which maximum absorption occurs. In addition to absorption, millimeter-wave propagation through the atmosphere is affected by forward and backward scattering, atmospheric ducting, and atmospheric turbulence. The magnitude of the latter are dependent on frequency, polarization, and operating range. Ducting in the ionosphere is usually associated with radar transmission over long ranges and is not of concern in the short range, passive radiometer application [43, 44].

Curves that give the one-way absorption coefficients (in dB/km) for millimeter-wave propagation through rain and fog are shown in Figure 8.12 [45, 46, 47, 48]. For two-way backscatter radar applications, the absorption coefficient is doubled and then multiplied by the range between transmitter and target to calculate the absorption in dB by which the energy reaching the sensor is reduced. Figure 8.12a shows measured values of the absorption coefficient for 15.5, 35, 70, 94, 140, and 225 GHz as a function of rain rate. Measured absorption data in fog are difficult to gather because of the nonsteady-state character of a fog. The measured absorption coefficients in rain are predicted from the theoretical model data shown in Figure 8.12b by the solid curves. The modeled value of absorption is obtained from the Laws and Parsons [49] drop size distribution corresponding to the rain rate. This distribution contains the number of droplets with radii in specific size ranges per unit volume as a function of rain rate. Crane [48, 50] found that differences between calculated values of absorption obtained from the Laws and Parsons drop size distribution and from a large number of observed drop size distributions were not statistically significant for frequencies up through 50 GHz. At higher frequencies, the drop size distribution measurement errors in the small drop size range affected the accuracy of the absorption versus rain rate relationship. Therefore, effects produced by different droplet size models could not be differentiated from effects due to absorption at these frequencies. The agreement of the modeled data with measured values allows the prediction of atmospheric absorption in rain over large regions of the millimeter-wave spectrum and rain rate variation when measured values are lacking. The data in Figure 6.12b may by interpolated to obtain absorption for other values of precipitation [47].

Optical visibility is commonly used to characterize fog for millimeter-wave attenuation measurements. However, the measurement of visibility is adversely affected by the Mie scattering[3] of light from droplets in the fog, which does not occur at millimeter-wave wavelengths. Although water density appears to be a more precise measure to characterize fog, the transient nature of a fog makes it difficult to obtain this measure. Hence the optical visibility characterization persists since the degree of attenuation in fog is commonly used in performance comparisons of millimeter-wave and infrared systems. Because droplet diameters in fog are small compared with millimeter wavelengths, scattering losses are negligible when compared to absorption of millimeter-wave energy by a fog.

---

[3] Mie scattering theory gives the general solution for the scattering of electromagnetic waves by a dielectric sphere of arbitrary radius. Rayleigh scattering, a limiting case of Mie scattering, applies when the wavelength is much larger than the scatterer's diameter [40].

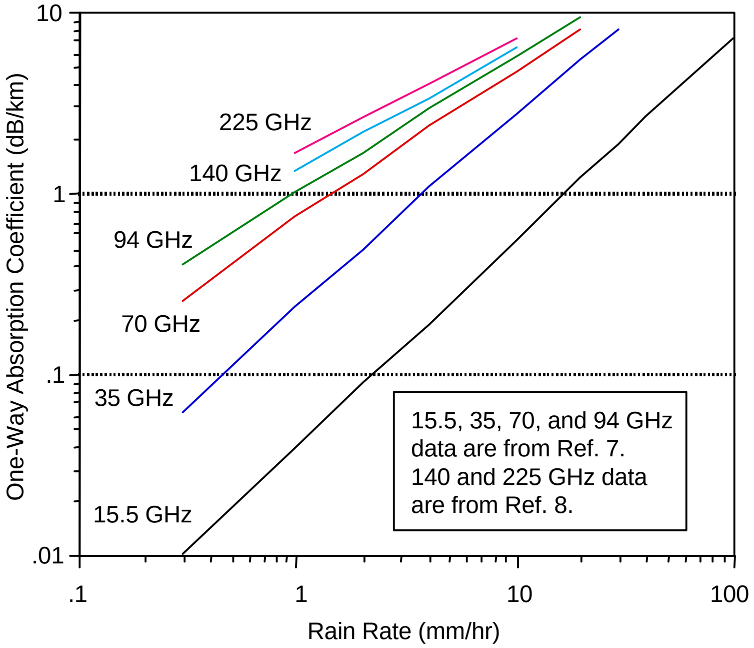

15.5, 35, 70, and 94 GHz data are from Ref. 7.
140 and 225 GHz data are from Ref. 8.

(a) Measured data

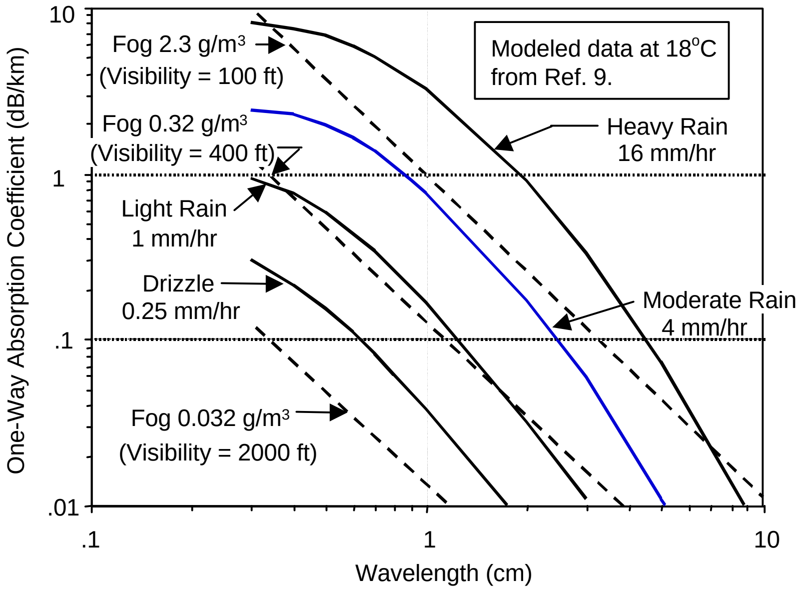

Modeled data at 18°C from Ref. 9.

(b) Modeled data

Figure 8.12 Absorption coefficient in rain and fog as a function of millimeter-wave frequency and rain rate.

The one-way absorption coefficient in fog has been modeled as a function of the volume of condensed water in the fog and the operating wavelength of the sensor [47]. The model gives the absorption K_a as

$$K_a = \frac{0.438 M_W}{l^{2}} \text{ dB/km} \tag{8.17}$$

where

K_a = one-way absorption coefficient,

M_W = mass of condensed water per unit volume of air in gm/m^3,

and

l = sensor wavelength of operation in cm.

Equation 8.17 is accurate within 5 percent when 0.5 cm $\leq l \leq$ 10 cm and when the droplets are extremely small with diameters of the order of 0.001 to 0.005 cm. A value of M_W = 1 g/m^3 represents about the maximum water content of most fogs, with the possible exception of heavy sea fogs. In most fogs, M_W is much less than 1. The FASCODE-1 weather model developed by the U.S. Air Force Geophysics Laboratory simulates two heavy fogs with liquid water contents of 0.37 and 0.19 g/m^3 and two moderate fogs with liquid water contents of 0.06 and 0.02 g/m^3 [51]. For both types of simulated fog, the condensed water mass is less than 1. The modeled absorption data for fog, shown in Figure 8.12b by the dashed lines, are plotted from (8.17).

Ryde and Ryde, as reported by Goldstein, have given an empirical relation between an average $\overline{M_W}$ and optical visibility in fog, namely [47]

$$\overline{M_W} = 1660 V_l^{-1.43} \tag{8.18}$$

where V_i is the optical visibility in feet and $\overline{M_W}$ is such that in 95 percent of the cases, M_W lies between $0.5M_W$ and $2M_W$. Such a relation may be useful when more precise values of M_W are not available.

Therefore, when the ratio of particle size to wavelength approaches unity, the energy attenuation increases. Thus, attenuation of shorter wavelengths (higher frequencies) can be greater in advective fogs because of the greater number of large particles and also because of the larger liquid water content of the fog. Calculations made by Richard [52] show that there can be a difference of 8 dB/km in attenuation at 140 GHz between advective and radiation fogs at 0.1 km visibility. Earlier measurements by Richer at the Ballistic Research Laboratories found a maximum one-way attenuation of 23 dB/km at 140 GHz during a 30-second time period, that returned to a lower value of 15 dB/km during the following 30-second interval. The change in attenuation was not accompanied by an appreciable change in visibility. The measured 8-dB variation was attributed to an increase in fog density beyond the limits of human visibility or to the condensation of fog into rain along the propagation path [53].

8.4.4 Prior and Current Applications

Gilnes reviewed the history of millimeter-wave sensors as airplane landing aids in inclement weather [54]. The applications are summarized in Table 8.4. A prototype sensor from each of the manufacturers was due to be delivered in about one year from the date of the article (1990). The use of image enhancement techniques to improve resolution was anticipated at the time this article was written. Indeed, this concept is to be used in the anticipated TRW MIMIC focal plane array.

Table 8.4 Summary of Millimeter-Wave Sensors for Use as Landing Aids in Inclement Weather

User/Manufacturer	Year	Frequency	Operating Mode
Air Force	circa 1977	35 GHz	Radar (active) with 60-inch antenna
Joint Air Force/FAA Program:	1990		
Martin Marietta		35 GHz	Radar (active)
Lear		94 GHz	Radar (active)
TRW		94 GHz	Radiometer (passive)

The focal plane array imaging radiometer is currently being readied for production by TRW, and is intended to produce images in near-real time (up to 15 video frames per second) through fog, smoke, and clouds [42, 55]. The camera operates at a center frequency of 90 GHz. The focal plane array of the camera contains 1,040 monolithic millimeter-wave integrated circuit (MMIC) receiver chips, creating an 80 x 52 pixel image. Aperture deconvolution algorithms help display an image that refreshes 17 times a second and is equivalent to an effective aperture of 24 inches instead of the actual 18 inches. In airplane applications, the pilot sees an image of the forward scene raster scanned on a head-up display with overlays of flight guidance cues. The image may be fused with infrared or visible images to enhance the information content and resolution of the image.

9 Field Evaluation of Available Advanced Technologies

We attempted to study the characteristics and performance of examples of every advanced imaging technology currently available which could potentially be used for highway surveillance or automated detection. A comprehensive survey of available literature and other information resources was conducted. Manufacturers, developers and vendors of equipment capable of real-time non-visible spectrum imaging were identified and contacted. The project director traveled to development laboratories for Infrared and millimeter wave imaging technologies, and attended the 1994 and 1995 IVHS America (now ITS America) Conferences, to be aware of the most current products and research developments in this area.

After negotiations resulting in various loan, rental, lease and subcontract arrangements, ten infrared cameras were obtained from manufacturers, vendors or system owners. A $20,269 subcontract was let to TRW Space and Technology division in Redondo Beach, California, to supply their experimental 94 GHz millimeter-wave imaging scanner for evaluation under this study. A VNIR camera was fabricated by modification of a conventional silicon CCD monochrome video camera, as described later. A $600,000 supplemental insurance policy was required to cover possible damage or loss of the systems.

Each imaging system was tested under a range of atmospheric, illumination, and scene conditions [30]. The imaging systems tested are listed in Table 9.1. Manufacturer's literature and specifications for each imaging system are included in the Appendix. Purchase prices for the cameras that we tested ranges from a low of $8,000 for the Texas Instruments NightSight, to a high of $100,000 for the Agema Thermovision 1000. The scope of this study was restricted to technical considerations, however, so that cost information is not stated for specific camera models. Manufacturer's literature and vendor contacts for each system are included in the Appendix.

We are aware of other infrared cameras currently being manufactured, which we could not negotiate access to, and were therefore not evaluated as part of this project.. These include the Amber Sentinel having a 320 (W) x 240 (H) uncooled microbolometer focal plane operating in the 8 to 12 μm wavelength band. The Amber Radiance Camera, another of the commercially available IR cameras not available for this study, has a 512 (W) x 512 (H) cooled InSb focal plane that operates in the 3 to 5 μm wavelength band with an integral Stirling closed-cycle cooler. The Argus Falcon surveillance system adds a weather-proof pan and tilt enclosure to the Radiance 1 camera and expands the operating temperature range to -

20^oC to $+60^oC$. The spectral band is optimized to 3.8 to 4.2 μm to eliminate the CO_2 absorption band above 4.2 μm. Uncooled, low-cost infrared cameras are also manufactured by Alliant Techsystems in Minnetonka, MN.

Table 9.1 Imaging Systems Tested

Company and Product	Received Wavelength Band (μm)	Focal Plane Temperature and Cooler Type	Detector Type	Array Size (pixels)
AGEMA Thermovision	8 to 12	77 K Sterling	HgCdTe	5 elements, X-Y mechanical scan
Cincinnati Electronics IRRIS-256ST	3 to 5	77 K Sterling	InSb	256 x 256
FSI PRISM	3.6 to 5	77 K Sterling	PtSi	320 x 244
GEC/Marconi Sentry IR20	8 to 14	Ambient	Microbolometer	200 x 200
Inframetrics 600	3 to 5 and 8 to 12	77 K Cryogenic	PtSi and HgCdTe	1 element, X-Y mechanical scan
Inframetrics 760	8 to 12	77 K Sterling	HgCdTe	1 element, X-Y mechanical scan
Inframetrics InfraCam	3 to 5	75 K Sterling	PtSi	256 x 256
Insight/Starsight	8 to 14	Ambient	Pyroelectric BST	256 x 256
Mitsubishi IR-M300	3 to 5	77 K Sterling	PtSi	256 x 256
TI Nightsight	8 to 14	Ambient	Pyroelectric BST	256 x 256
TRW Multispectral Scanner	94 GHz (millimeter-wave)	Ambient	HEMT*-heterodyne	1 element, X-Y mechanical scan

* HEMT = high electron mobility transistor

10 Metrics for Image Information Content

10.1 Object Discrimination

Johnson's [56] early investigations helped to determine the number of pixels that must be resolved on a target or object in order for a human observer to know either that it is present (detection), its symmetry and orientation (orientation), the class to which it belongs (classification), or its description up to the limit of the observer's knowledge (identification). These discrimination levels and their interpretations are summarized in Table 10.1. The ability of the observer to interpret an image in these quantum steps is a function of the contrast and brightness of the object, properties of the specific intensifier device used to enhance the image, and the physiological response characteristic of the human eye-brain interface. Contrast is a function of the image signal-to-noise ratio, while brightness is determined by the luminance of the target.

Table 10.1 Object discrimination levels.

Discrimination Level	Interpretation
• Detection	• Object or target is present
• Orientation	• Object is approximately symmetric or asymmetric and its orientation is discerned
• Classification (sometimes called recognition)	• Class to which object belongs is discerned (e.g., house, automobile truck, tank, man)
• Identification	• Target is described to the limit of the observer's knowledge (e.g., motel, Honda Accord, pickup truck, T-62 tank, soldier)

In the experimental procedure used by Johnson, the ability of a human observer to discern a bar pattern of a given resolution was correlated with the discrimination level (detection, orientation, classification, or identification) for an object. The range was increased until the object was just barely detected, or its orientation determined, or classified, or identified by the observer. Then a U.S. Air Force standard tri-bar chart, scaled to the image, was placed in the field of view. The standard tri-bar chart contains resolutions from 0.25 to 14.3 lines per mm. The number of resolved line pairs per foot [1 line pair equals 2 television lines or two picture elements (pixels)] needed by the observer for each level of discrimination was recorded. This value varied with the dimensions of the targets. When the number of resolved line pairs was referenced to the minimum dimension of the target, as indicated on the left of Figure 10.1, the variability was reduced such that the maximum difference in the number of line pairs needed at all levels of discrimination among the test targets was not more than 25 percent. The resolution required for discrimination was therefore set equal to the number of dark and light line pairs subtended by the object's minimum dimension. Johnson's experiments were limited to broadside views of the targets. He also noted that the bar pattern must have the same contrast as the internal contrast of features in the target. While the level of discrimination of the targets themselves is range dependent, the discrimination level represented by the given number of resolved line pairs is independent of distance. Higher target discrimination levels occur at closer ranges for a given sensor design and object-to-background contrast.

Table 10.2 shows the results of Johnson's experiments. On the average, 2 pixels (1 line pair) must be resolved within an object's minimum dimension for detection, 2.8 pixels (1.4 line pairs) for orientation, 8.0 pixels (4.0 line pairs) for classification, and 12.8 pixels (6.4 line pairs) for identification. The increased number of line pairs needed for each higher discrimination level is illustrated on the right side of Figure 10.1. Johnson's original findings apply to first-generation FLIR sensors with one-dimensional detector arrays and a scene scanning mechanism. Two-dimensional arrays require fewer pixels to be resolved over the target area as will be discussed later. The number of line pairs required for a particular discrimination level assumes that adequate image signal-to-noise ratio (image contrast) exists. Even when these conditions are met, only a 50 percent target discrimination probability is guaranteed by the numbers of line pairs in Table 10.2. To increase the probability, either the number of pixels that subtends the minimum dimension of the target, i.e., sensor resolution, or the signal-to-noise ratio must increase.

Johnson later extended his work to relate any value for the probability of discrimination to the number of line pairs that can be resolved across the minimum dimension of a target. He defined the target transform probability function (TTPF) that correlates the discrimination probability to the ratio of the actual number of line pairs resolved across the target's minimum dimension to the standard number given by the Johnson criteria in Table 10.2 [57, 58, 59, 60]. A plot of the TTPF is shown in Figure 10.2 as the desired discrimination probability versus the ratio of the number of resolvable cycles across the minimum dimension of the target to the standard number.

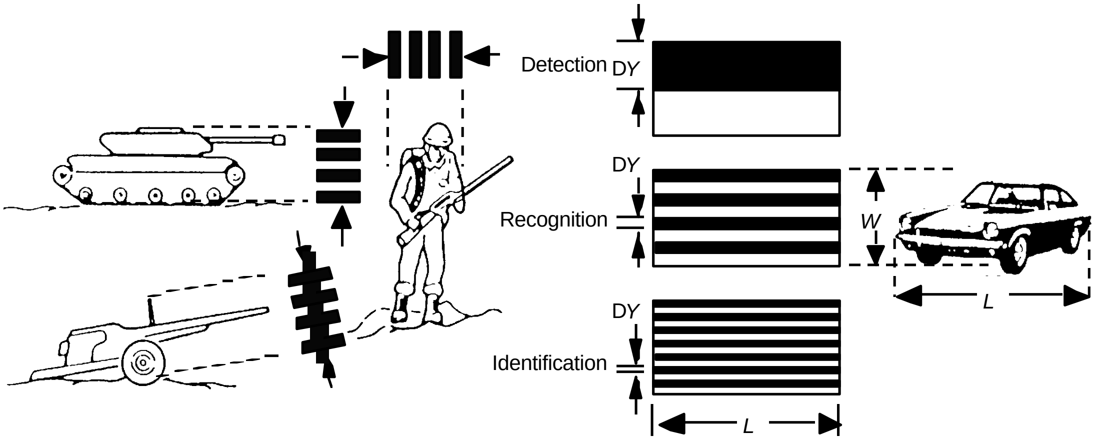

Figure 10.1 Correlation of a target object's minimum dimension with the spatial frequency of a bar pattern. *From*: Johnson, J., "Analysis of Image Forming Systems," *Image Intensifier Symposium*, Fort Belvoir, VA, Report AD-220160, Oct. 1958, pp. 249-273.

Table 10.2 Johnson's object discrimination criteria for one-dimensional arrays. *From*: Johnson, J., "Analysis of Image Forming Systems," *Image Intensifier Symposium,* Fort Belvoir, VA, Report AD-220160, Oct. 1958, pp. 249-273.

Target (Broadside View)	**Resolution per minimum dimension in line pairs**			
	Detection	**Orientation**	**Classification**	**Identification**
Truck	0.90	1.25	4.5	8.0
M-48 tank	0.75	1.20	3.5	7.0
Stalin tank	0.75	1.20	3.3	6.0
Centurion tank	0.75	1.20	3.5	6.0
Half track	1.00	1.50	4.0	5.0
Jeep	1.20	1.50	4.5	5.5
Command car	1.20	1.50	4.3	5.5
Soldier (standing)	1.50	1.80	3.8	8.0
105 howitzer	1.00	1.50	4.8	6.0
Average	1.0 ± 0.25	1.4 ± 0.35	4.0 ± 0.8	6.4 ± 1.5

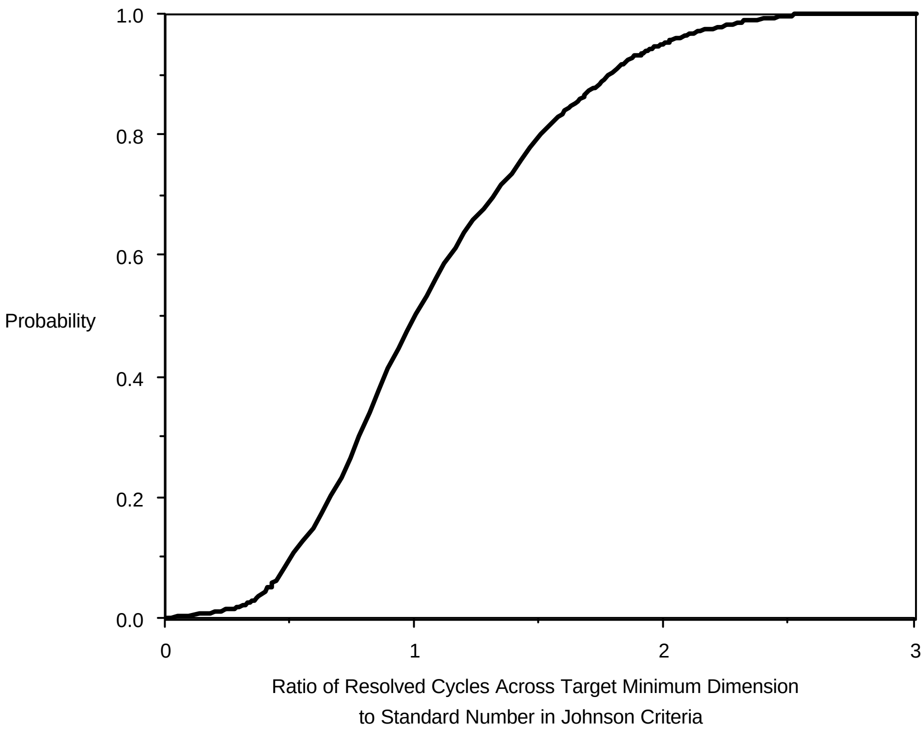

Figure 10.2 Target transform probability function.

The truck data in Table 10.2 provide an example of how to apply Johnson's criteria to calculate the resolution required to detect and classify a truck. Table 10.2 specifies that 1.8 pixels (0.90 line pairs) are needed across the minimum (height) dimension for detection. If the height is 3.3 m, the resolution of each pixel must be 3.3 m/1.8 = 1.8 m. For classification, 9.0 pixels (4.5 line pairs) are required, implying a pixel resolution of 3.3 m/9.0 = 0.37 m.

Rosell and Willson [60] have confirmed Johnson's results for object detection, classification, and identification, and Schmieder and Weathersby have confirmed the results for detection [61]. Rosell and Willson superimposed transparencies of vehicles on transparencies of one of four background regions, namely a uniform white background, a road, grass, and grass among trees. The vehicle images used in the classification experiments were of a tank, a van truck, a half track with top-mounted radar antenna, and a tracked bulldozer with a derrick. The vehicle images used in the identification experiments were of M-47 Patton, M-48 Centurion, Panther, and Stalin tanks. The transparencies of the vehicles were made from photographs taken at a 45-degree depression angle, perpendicular to the vehicle's longitudinal axis, such that the sides and tops of the vehicles were imaged. The vehicle types and video signal-to-noise ratio were randomly varied and the probabilities of classification and identification were determined.

Table 10.3 shows that target classification becomes more challenging with added background clutter typical of a realistic environment. On the average, a 30 percent increase in image signal-to-noise ratio was needed before the observers could classify the targets in the clutter backgrounds as compared to the uniform white background with the same sensor resolution. In the uniform background, 1 pixel was needed across the target's minimum dimension to *detect* it when the image signal-to-noise ratio was 2.8, 8 pixels were needed across the target's minimum dimension to *classify* it when the image signal-to-noise ratio was 2.5, and 13 to *identify* it when the image signal-to-noise ratio was 3.0 at the 50 percent probability level. These results are in general agreement with Johnson's. In the clutter background, 2 pixels were required for detection with an image signal-to-noise ratio of 2.5. For classification in clutter, the same 8 pixels were required, but with an increased image signal-to-noise ratio of 3.4.

Table 10.3 Increase in image signal-to-noise ratio required for classification in clutter as compared with a vehicle in a uniform white background. *From:* Rosell, F.A. and Willson, R.H., "Recent Psychophysical Experiments and the Display Signal-to-Noise Ratio Concept," Chapter 5 in *Perception of Displayed Information*, Ed.: Biberman, L.M., Plenum Press, NY, 1973.

Background	**Increase in Image Signal-to-Noise Ratio**
• Road	15%
• Grass	24%
• Grass among trees	52%
• Clutter average	30%

The results of the Rosell and Willson classification experiments were re-plotted by Gordon, *et al.*, as given in Figure 10.3, to illustrate the probability of classification as a function of signal-to-noise ratio with a constant 4 line pairs (8 pixels) per minimum object dimension, and as a function of the number of line pairs with the signal-to-noise ratio fixed at 2.8 [62]. The dashed curve with the signal-to-noise ratio variable shows that the 50 percent probability of classification occurs with a relatively small signal-to-noise ratio of 2.8 and 4 line pairs resolved across the target's minimum dimension. The solid curve indicates that approximately 7.5 line pairs are required to achieve a 90 percent probability of classification at the same signal-to-noise ratio.

The Schmieder and Weathersby [61] detection results for targets viewed in synthetically generated clutter are shown in Table 10.4. In this experiment, observers were placed in front of a television monitor and had unlimited viewing time to detect the targets. Tree, road, and grass clutter were synthetically generated in the 8 to 12 micrometer wavelength band. Three different shaped targets were used: a Soviet T-10 tank, a U.S. Army jeep with canvas-enclosed cab, and a U.S. Army 2-1/2 ton truck with a canvas top. The signal-to-clutter ratio was varied by adjusting the target signal relative to a given set of clutter statistics in a given scene. Target and scene resolution were controlled using a two-dimensional Gaussian filter as a point spread function.

The signal-to-clutter ratio (*S*/*C*) is defined for positive or negative contrast targets as

$$S/C = \frac{\left|\text{Maximum target radiance} - \text{Mean background radiance}\right|}{\text{RMS clutter radiance}} . \qquad (10.1)$$

The RMS clutter radiance is computed as the average of the standard deviations s_i of the radiance of the N clutter cells in the scene. Thus,

$$\text{RMS clutter radiance} = \left(\sum_{i=1}^{N} \frac{s_i^2}{N} \right)^{1/2} . \qquad (10.2)$$

The data in Table 10.4 below demonstrate the expected results, namely that as the signal-to-clutter ratio increases, fewer line pairs need be resolved on the target to achieve a given detection probability. The Johnson results that require an average of one line pair to achieve a detection probability of 0.5 are confirmed for a broad range of signal-to-clutter ratios between 1 and 10.

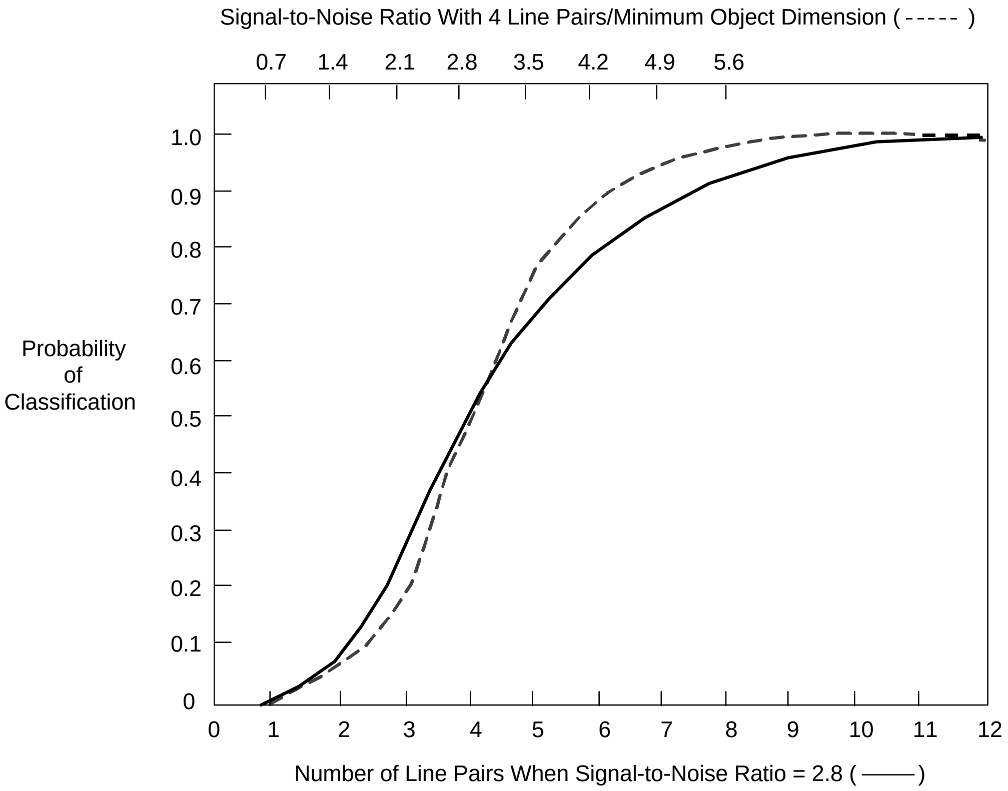

Figure 10.3 Probability of classification as a function of signal-to-noise ratio and resolution. *Source*: Gordon, G.A., Hartman, R.L., and Kruse, P.W., "Imaging-Mode Operation of Active NMMW Systems, " Chapter 7 in *Infrared and Millimeter Waves, Vol. 4: Millimeter Systems*, Ed.: Button, K.J. and Wiltse, J.C., Academic Press, NY, 1981. Reprinted with permission.

Table 10.4 Detection criteria for broad categories of clutter. *Source*: Schmieder, D.E. and Weathersby, M.R., "Detection Performance in Clutter With Variable Resolution," *IEEE Vol. AES-19*, No. 4, Jul. 1983, pp. 622-630.

Detection Probability	**Number of Line Pairs/Target**		
	Low Clutter (S/C>10)	**Moderate Clutter (1≤S/C≤10)**	**High Clutter (S/C<1)**
1.0	1.7	2.8	–
0.95	1.0	1.9	–
0.90	0.9	1.7	7.0 (estimated)
0.80	0.75	1.3	5.0
0.50	0.5	1.0	2.5
0.30	0.3	0.75	2.0
0.10	0.15	0.35	1.4
0.02	0.05	0.1	1.0
0.00	0.0	0.0	0.0

With the advent of two-dimensional detector arrays, the original CNVEO target classification model was revised to take into account the number of pixels resolved within the boundaries of an objet, rather than the number of line pairs across tits minimum dimension. The 1990 and 1992 advanced FLIR sensor performance models apply to both first- and second generation FLIRs. The eye-brain interface has been updated, as have various measures of performance for evaluating imaging and tracking infrared sensors [63, 64].

10.2 U.S. Weather Bureau Meteorological Range Metric

The quantitative meteorological range metric reported by the U.S. Weather Bureau for many localities can be used to estimate the visual range. It is based on the reduction of apparent contrast produced by atmospheric attenuation at 0.55 μm [65]. The apparent contrast C_x of a radiation source when viewed at a distance x is defined as

$$C_x = \frac{R_{sx} - R_{bx}}{R_{bx}} \tag{10.3}$$

where R_{sx} and R_{bx} are the apparent radiance or radiant emittance of the source and background when viewed from a distance x. The units of R_x are power per unit area. The distance at which the ratio

$$\frac{C_x}{C_o} = \frac{(R_{sx} - R_{bx})/R_{bx}}{(R_{so} - R_{bo})/R_{bo}} \tag{10.4}$$

is reduced to 2 percent is defined as the meteorological range or sometimes the visual range. Equation 10.4 is usually evaluated at λ = 0.55 μm. The subscript *o* refers to the radiance measured at the source and at the background, i.e., $x = 0$. Using V to represent the meteorological range allows (10.4) to be rewritten to define the meteorological range as

$$\frac{C_{x=V}}{C_o} = 0.02 \tag{10.5}$$

If the source radiance is much greater than that of the background for any viewing distance such that $R_s >> R_b$ and the background radiance is constant such that $R_{bo} = R_{bx}$, then the meteorological range can be expressed in terms of the apparent radiance as

$$\frac{C_{x=V}}{C_o} = \frac{R_{sV}}{R_{so}} = 0.02 \qquad (10.6)$$

or

$$\ln\left(\frac{R_{sV}}{R_{so}}\right) = -3.91 \qquad (10.7)$$

The Lambert-Beer law for atmospheric transmittance $\tau_a(\lambda)$ (discussed in Section 7) can be used to relate the extinction coefficient (that includes both absorption and scattering effects) to the meteorological range. Thus, the atmospheric transmittance is written as

$$\tau_a(\lambda) = \left(\frac{R_{sV}}{R_{so}}\right) = \exp\left[-\gamma(\lambda)\, x\right] \qquad (10.8)$$

where

γ = extinction coefficient or power attenuation coefficient in nepers (Np)/km,

and

x = path length in km.

Multiplying the attenuation coefficient in dB/km by 0.23 converts it into Np/km.

Upon taking the natural log (ln) of both sides of (10.8) and using (10.7), we find

$$\gamma(\lambda) = 3.91/V \text{ at } \lambda = 0.55\ \mu\text{m}. \qquad (10.9)$$

Thus, the meteorological range is related to the extinction coefficient through the multiplicative constant of 3.91. This is sometimes referred to as the Koschmieder formula [66].

10.3 Qualitative Visibility Metrics

Visibility is a qualitative measure of distance. It is defined as the greatest distance at which it is just possible to see and identify with the unaided eye: (a) in the daytime, a dark object against the horizon sky and (b) at night, a known moderately intense light source [65]. Its measurement is subjective.

If only the visibility metric observed by a human, V_{obs}, is available, the meteorological range V is estimated as

$$V = (1.3 \pm 0.3)V_{obs} \qquad (10.10)$$

10.4 Applying Fuzzy Logic to the Definition of Visibility in Fog

A fuzzy set is a set whose boundaries are not defined precisely, such as the visibility estimated by motorists. In fact, most motorists describe the visual range using intervals of visibility such as: “I believe the visibility is about 200 m, certainly more than 150 m and less than 300 m.” If a series of intervals can be provided for the degree of credibility between 0 and 1, than a membership function, whose value is between 0 and 1, can be defined. This approach is used by Boreux and Duckstein to estimate the relationship between the horizontal visibility (as estimated by an expert) and the extinction coefficient of fog, taking into account the vagueness of the data and the psychophysical human processes [67].

Three methods are presented to calculate the value of the constant k used to define visibility V in the form

$$V = k/g, \tag{10.11}$$

where

g is the extinction coefficient of the aerosol.

1. $V = 3.9/g$ under the following idealized conditions:

    (a) perfect observer under daylight conditions defined by the condition when the minimum level of contrast that a normal human eye can distinguish (often called the threshold of brightness contrast) = $e = 0.02$

    (b) perfect black target defined by the condition when the intrinsic contrast C_0 of the object against the background = -1

    (c) homogeneous atmosphere, i.e., g is constant along the sight path

    (d) horizontal viewing, earth without curvature, cloudless sky, i.e., luminance of the background is the same at any distance

    (e) aerosol particles scatter light individually, i.e., multiple scattering effects are ignored.

2. A Fuzzy Hyperbolic Model

    $$V = 4.19/g \tag{10.12}$$

    This model minimizes the distance between the estimated visibility and the corresponding measured fog extinction coefficient.

3. Treating the Constant k as a Fuzzy Number

    $$V = 4.30/g \tag{10.13}$$

    This model calculates a fuzzy estimate of k as the product of fuzzy estimates of the extinction coefficient and the visibility. The model then calculates a point value for k by defuzzification.

Both Fuzzy models incorporate the maximum uncertainties in the fog extinction coefficient and the estimated visibility. The two fuzzy approaches yield results that are consistent. The authors recommend using the k result from the second fuzzy model because this analysis applies defuzzification at the end of the calculation rather than at the beginning.

11 Development of an Improved Metric For Highway Visibility

This section describes a spectrum-independent metric designed specifically to quantify the visibility-reducing potential of fog or dust as perceived by vehicle drivers on highways. Like conventional sight-distance metrics, it includes the effects of transmission and absorption by the fog, and adds the backscatter of light from the driver's own headlights as well as other light sources. These effects are represented in Figure 11.1 which shows hypothetical leading and following vehicles, and define the transmittance t_a, and absorption K_a (or equivalently the emission), forward scatter K_s, and backscatter K_B coefficients of the fog or intervening atmosphere.

The eye of the driver in the following vehicle receives energy emitted by the vehicle or scene in front as attenuated by the absorption and scattering effects of the fog. In addition, if the trailing vehicle's headlights are on, light from the headlights is backscattered toward the driver. Backscatter is a volumetric effect. Hence, the backscattered energy E_B is proportional to the product of the variable distance R of the fog droplet scatterers from the vehicle and the cross-sectional area represented by the field of view of the driver or measuring instrument. Thus,

$$E_B \, \alpha \, K_B V_c \qquad (11.1)$$

where

α = proportionality symbol,

K_B = backscatter coefficient in m^2/m^3,

V_c = volume of resolution cell in m^3

$= (R) (\pi/4) (Rq_a) (Rq_e)$, (11.2)

and

q_a, q_e = azimuth and elevation angular subtense of the human eye or viewing instrument in radians.

Since the backscatter coefficient varies with distance, the total energy is found by integrating (11.1) over the distance d between the leading and following vehicles. Thus,

$$E_B \, \alpha \int_0^d K_B V_c \, dR \, . \qquad (11.3)$$

The units of d and R in the above equations are meters since K_B is expressed in m^2/m^3.

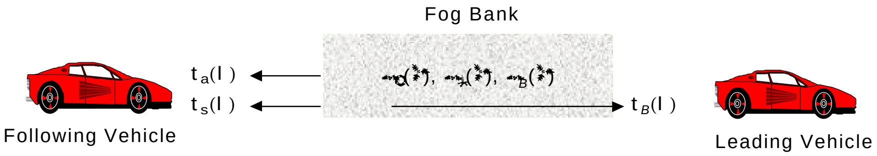

$t_a(l)$ = transmittance due to absorption of visual image presented to the driver in a following vehicle

= exp [-[illegible]R]

$t_s(l)$ = transmittance due to forward scattering of visual image presented to the driver in a following vehicle

= exp [-[illegible]R]

$t_B(l)$ = transmittance due to backscattering of light from the following driver's own headlights

= exp [-[illegible] A_c R]

A_c = cross-sectional area represented by the field of view of the driver or measuring sensor instrument

Figure 11.1 Transmission and backscatter of light in a fog scenario

Atmospheric transmittance $t_a(l)$ is modeled by the Lambert-Beer Law as [68, 69]

$$t_a(l) = \exp[-g(l) R] \qquad (11.4)$$

where

g = extinction coefficient or power attenuation coefficient in nepers (Np)/km,

and

R = range or path length in km.

In (11.4) R is in km since g is expressed in units of Np/km. Multiplying the attenuation coefficient in dB/km by 0.23 converts it into Np/km.

The extinction coefficient $g(l)$ is the sum of the absorption and scattering coefficients $k_a(l)$ and $k_s(l)$, respectively, and can be written as

$$g(l) = k_a(l) + k_s(l). \tag{11.5}$$

Absorption and scattering coefficients, in turn, are sums of molecular and aerosol components denoted by the subscripts *m* and *a*, respectively, such that

$$k_a(l) = k_{am}(l) + k_{aa}(l) \tag{11.6}$$

and

$$k_s(l) = k_{sm}(l) + k_{sa}(l). \tag{11.7}$$

An expression for the average value of the transmission $\bar{t}_a$ over a wavelength band l_1 to l_2 is given by

$$\bar{t}_a = \frac{1}{l_2 - l_1}\int_{l_1}^{l_2} \exp[-g(l)R]\,dl \tag{11.8}$$

Typically, atmospheric computer models (such as LOWTRAN and MODTRAN) are used to evaluate expressions such as (11.8).

Having derived the relations between the absorption and scattering coefficients, we now define the spectrum-independent metric for determining the visibility in fog. This metric is of potential value to drivers and traffic management personnel. The metric t_V is given by

$$t_V = \frac{\int_{l_{s1}}^{l_{s2}} (t_a t_s)\,dl}{l_{s2} - l_{s1}} - \frac{\int_{l_{i1}}^{l_{i2}} (t_a t_B)\,dl}{l_{h2} - l_{h1}} \tag{11.9}$$

where

$t_a(l)$ = transmittance due to absorption of visual image presented to the driver in a following vehicle

$= \exp[-k_a(l)R]$, (11.10)

$t_s(l)$ = transmittance due to forward scattering of visual image presented to the driver in a following vehicle

$= \exp[-k_s(l)R]$, (11.11)

$t_B(l)$ = transmittance due to backscattering of light from the following driver's own headlights

$$= \exp [-k_B(l\ ) A_c R], \qquad (11.12)$$

A_c = cross-sectional area represented by the field of view of the driver or measuring sensor instrument,

l_{s0} = lower spectral limit of human or sensor instrument response,

l_{s1} = upper spectral limit of human or sensor instrument response,

l_{h0} = lower spectral limit of vehicle headlight illumination, and

l_{h1} = upper spectral limit of vehicle headlight illumination.

Scattering coefficient values are shown in Table 11.1 [70]. They were either empirically determined or calculated by quantum effects simulation.

Table 11.1 Scattering coefficients $k_s(l\ )$ in the visible and infrared

Applicable Wavelength	Value*
0.55 μm	3.91
3 to 5 μm	2.24
8 to 12 μm	0.85

* $k_B(l\ )$ is typically 0.25 to 0.75 of $k_s(l\ )$

When a sensor instrument that measures visibility in fog is not present and the leading vehicle is illuminated by the headlights from the following vehicle, the visibility metric becomes

$$t_V = \frac{\int_{l_1}^{l_2} t_a \left(t_s - t_B\right) dl}{l_2 - l_1}, \qquad (11.13)$$

where l_2 is the max (l_{s2}, l_{h2}), l_1 is the min (l_{s1}, l_{h1}), and *s2 and s1* represent the upper and lower spectral response limits of the human eye.

Under some circumstances, it may be possible to solve for one of the scattering coefficients in terms of another. By conservation of energy, the sum of the transmitted t_a, absorbed a (equal to the emitted energy), and scattered s energies equals unity. Thus,

$$1 = t_a + t_a + t_s \qquad (11.14)$$

If the absorbed (emitted) energy is negligible as it may be if the path length is sufficiently small or the emissivity of the intervening atmosphere is small (e.g., a low water content fog), then

$$t_s\ (l\ ) = 1 - t_a(l\ ). \qquad (11.15)$$

12 Development of Image Information Metrics for Highway Surveillance and Detection

12.1 Assessment of TMC Surveillance Needs

The performance of imaging sensors is of interest both for the needs of human observers and machine vision-based detectors. With respect to the first set of requirements (human observation), we sought to learn as much as possible about the surveillance needs and preferences of traffic management on the “front line”, i.e., TMC operators. A survey was created and administered to traffic management personnel in Caltrans District 12 and the Anaheim TMC. Its purpose was to translate verbal observations and preferences into quantifiable components of a standard metric that could be consistently applied using machine vision techniques to our field-acquired image data. We generally sought to determine factors that are important to TMC operators or law enforcement personnel, such as ability to identify individual vehicles, vehicle separation, speed determination, following distance, traffic density, traffic shock wave characteristics. From these observations, we hope to gain a better sense of emphasis in the formulation of one or more analysis metrics for video imagery that we would later apply to all camera field data.

Survey Questions:

1. To do your job, what do you need to see in the image presented by a video camera to detect, classify, identify, and determine vehicle interactions such as incidents? Quantify each item listed on a scale of 2 to 5, 2=minmal importance, 3=moderate importance, 4=very important, 5=cannot function without it. (1=no importance or not used.) Examples of what needs to be seen in the image are: side view of vehicle, front view, rear view, tail lights on, headlights on, truck bed, number of tires, movement of vehicle, and vehicles side by side. This list is not meant to be complete.

   Detect (vehicle is present):

   Classify (the class to which the vehicle belongs, e.g., sedan, pickup truck, minivan):

   Identify (vehicle description up to the limit of the observer's knowledge, e.g., Chevy Camero, Plymouth Voyager, Toyota Tacoma):

   Vehicle interactions:

   Vehicle separation:

   Speed:

   Traffic density:

   Traffic shock wave:

2. What are the visual clues for each, such as color, resolution, close up vs. wide field of view imagery, contrast between vehicle body and its lights or street lighting? Quantify each clue listed on a scale of 2 to 5, 2=minmal importance, 3=moderate importance, 4=very important, 5=cannot function without it. (1=no importance or not used.)

   Detect:

   Classify:

   Identify:

   Vehicle interactions:

   Vehicle separation:

   Speed:

   Traffic density:

   Traffic shock wave:

3. Do the visual clues change with weather or lighting conditions such as fog, rain, night? Quantify each clue listed on a scale of 2 to 5, 2=minmal importance, 3=moderate importance, 4=very important, 5=cannot function without it. (1=no importance or not used.)

   Detect:

   Classify:

   Identify:

   Vehicle interactions:

   Vehicle separation:

   Speed:

   Traffic density:

   Traffic shock wave:

4. Do the visual clues change with low and high traffic volume? Quantify each clue listed on a scale of 2 to 5, 2=minmal importance, 3=moderate importance, 4=very important, 5=cannot function without it. (1=no importance or not used.)

   Detect:

   Classify:

   Identify:

   Vehicle interactions:

   Vehicle separation:

   Speed:

   Traffic density:

   Traffic shock wave:

5. Other features and factors that impact recognition of features used to determine traffic flow parameters in inclement weather. Quantify each item listed on a scale of 2 to 5, 2=minmal importance, 3=moderate importance, 4=very important, 5=cannot function without it. (1=no importance or not used.)

12.2 Results of TMC Operators' Surveillance Survey

The survey was reviewed with the TMC supervisor and one of his personnel. The other personnel were not available to receive a first-hand explanation of the survey. Assurances were received that the survey questions were understood and that they would be explained and given to others to complete.

The most prevalent general comment was that color information was important in identifying vehicles involved in an incident (both the vehicles contributing to the incident, debris, and vehicles and personnel dispatched to clear the incident) and in distinguishing vehicles from the roadway or the environment in which they were operating during inclement weather (i.e., rain, fog, dust, etc.). The TMC personnel could not place a number or value on the color benefit, however, nor could they quantify the relative benefit of color compared to black and white imagery. This is not meant to be a criticism of the survey participants. Understanding and quantifying human perception of color is a very complex subject as will be discussed further in Section 12.5.5.

There were three TMC personnel who did provide qualitative responses to the questionnaire of Section 12.1. The results are given in Table 12.1. It appears that the respondents rated the importance of visual imagery in determining the traffic characteristics listed across the first row of the table, although the intent of the survey was to elicit other information. In the future, a questionnaire such as this will have to be modified to include additional examples to better illustrate the information that is sought.

Table 12.1 Relative importance of imagery for performing various traffic management functions.

Question	Detect	Classify	Identify	Vehicle Interactions	Vehicle Separation	Speed	Traffic Density	Traffic Shock Wave
1: Image	5, 5, 5	2, 4, 2	2, 2, 1	3, 3	3, 2, 3	1, 1, 3	5, 5, 5	2, 3
2: Clues	5, 5, 5	2, 4, 2	4, 3, 3	3, 2	3, 3, 3	2, 1, 3	4, 5, 4	2, 3,
3: Changes with weather	4, 5, 5	4, 4, 3	4, 4, 2	4, 3	2, 2, 3	2, 1, 3	5, 5, 4	2, 3
4:Changes with traffic volume	3, 5, 5	2, 2, 3	2, 2, 2	3, 3	3, 3, 3	3, 1, 3	2, 5, 4	2, 3
5: Other factors important in inclement weather	No responses							

There appears to be a great interest (at least among the three respondents) in using imagery to aid in vehicle detection and to estimate traffic density. The least impact of the imagery appears to be in determining speed.

When these results were received, plans were discussed to repeat the exercise at other TMCs. However, in view of the poor response due to the time required by TMC personnel to participate in the survey, we elected to not repeat this data collection exercise.

12.3 Formulation of Image Information Metrics

We learned from the limited survey and interview results and from our prior work, that useful information was most often based upon contrast, either in intensity or color, between a target and its background. The greater the contrast of the target, the greater its detectability. Thus, a well-delineated car on a dark roadway surface had rich information content, while a less-delineated image of the car (for example, in low contrast IR) would contain less useful information. Noise in the image, which manifests as false variations in pixel intensity or color, is considered “false” information. Ultimately, what a TMC operator needs to see (or classify, identify, assess) in a traffic scene are objects (vehicles, pedestrians, signage, equipment or debris on the roadway). This general observation leads to the concept of measuring the average variation in pixel intensity levels in a sizable target window encasing an object in the image, and dividing this by the average variation in pixel intensity levels over many frames of this window when no object is present, that is, just observing the background. The result is a noise-normalized metric of image information in the scene. Averaged over many frames containing many different types of objects, this metric may be used for comparisons, on a frame-by-frame basis, of two completely different types of imaging systems that simultaneously view and transduce the same scene.

The final pair of image analysis metrics that was developed is based on a signal-to-noise ratio calculation. This type of metric was selected because it is commonly used in scientific and military applications as the measure of effectiveness of a sensor when the sensor is used to detect an object. In this case, one is concerned with the relative signature of the object to be detected with respect to the background in which it is found. When passive infrared or millimeter-wave sensors are used, the signatures of the desired object and the background are given in terms of emitted temperature in degrees Kelvin. When a visible spectrum imager is used, the signatures are in terms of luminance. The minimum temperature difference between the object and the background that can be detected by the sensor is a function of the noise-equivalent temperature difference or NE∆T of the sensor.

Other measures of effectiveness are known to exist for other sensor applications, but were considered to be of limited applicability in traffic surveillance. For example, when the internal structure of objects located in the field of view of the sensor are important, minimum resolvable temperature difference (MRTD) is often used as the measure of sensor performance. The MRTD is a measure of the signal-to-noise limited thermal sensitivity as a function of spatial frequency (the rate of change of light-to-dark features with respect to a distance measure) [71]. MRTD is measured as a function of spatial frequency for FLIR sensors that obtain imagery often used to classify and identify objects in military applications.

Still other metrics have been employed to measure the chromatic (color) information in an image when human interpretation of color imagery is a part of the object detection or classification process. In this case, the psychophysical or color perception capability of humans is modeled by using color spaces based on the Commission Internationale de l'Eclairage (CIE) L*u*v*, CIE L*a*b*, or CIECAM specifications [72].

12.4 Characteristics of Human Perception

The threshold for the human response for detection, classification, and discrimination (as defined below) is the value that elicits a 0.5 likelihood of response (corrected for guessing). This threshold has the following properties [73]:

- Statistical quantity
- Varies with measurement technique
- Varies with form of the data analysis
- Varies with the instructions or criteria level set by the observer
- Results vary from lab to lab and observer to observer.

The human responses for detection, classification, area classification, and discrimination are defined as:

♦ Detection:	observer correctly decides that an object of interest exists in the field of view (FOV).
♦ Classification:	observer correctly indicates to which class of objects the detected object belongs.
♦ Area classification:	observer correctly indicates that the location of the object is in the FOV.
♦ Discrimination:	observer correctly indicates that the singular object of interest is in the FOV, i.e., observer correctly separates the singular object of interest from the class of classified objects.

When the observer looks for a particular pre-selected object among many other objects and only one such example of that object is possible on the display, the tasks of detection, classification, and discrimination are considered by many researchers to be at least non-independent, if not equivalent. The percent or the probability of a correct response is a function of range to object, time object is in FOV, number of trials, and object-to-background contrast.

At small values of target angular size (a) and effective exposure time (t), signal dispersion occurs spatially and temporally, respectively. This causes the retina to be excited by a signal spread out in area and lengthened in duration as compared to the case when the imaging device has a point spread function and impulse response function in space and time, respectively.

As a and t increase, the effects of dispersion on signal-to-noise ratio decrease. When a and t are large (i.e., negligible dispersion), the signal-to-noise ratio again decreases due to the failure of the human visual system to function as a perfect integrator of excitations of the retina. This occurs because the area of the image of the object on the retina and the flash duration become too large.

The human visual system functions similarly to an ideal noise-limited photon counter with a variable signal threshold set by the background luminance at 2 to 4 times the standard deviation of the background.

Objects moving at rates up to 20 deg/sec are nearly as detectable as stationary objects. At 120 deg/sec, small objects can still be detected, but must be increased in size threefold over their threshold size at a given light level when stationary.

The threshold value for the signal-to-noise ratio $(S/N)_{th}$ can be written as

$$(S/N)_{th} = 1.7\, m\, D_E \left(\mathrm{h}_E\, \mathrm{t}_E\, \bar{E}\right)^{1/2} \text{ x } 10^3 \qquad (12.1)$$

where

$m = c_{IN} / (1/\mathrm{a})$,

c_{IN} = input contrast,

a = angular size of a disk in mrad,

D_E = diameter of the eye aperture in cm (approximately 0.7 cm),

t_E = effective integration time of the eye (approximately 0.2 sec),

$\bar{E}$ = background luminance in ft-Lamberts (10^{-5} to 10^{-2} or greater), and

h_E = quantum efficiency of the eye (approximately 0.08).

One lumen of white light is equivalent to 1.4×10^{16} quanta/sec emitted by a blackbody at 5400K in the 0.4 to 0.73 µm band.

Typical values for $(S/N)_{th}$ are 2.8 to 4.4.

Since we are interested in the automated detection of automobiles in fog or other inclement weather environments, a measure of effectiveness related to the image signal-to-noise ratio (S/N) was chosen for analyzing the video imagery gathered during the course of this project. Since computer detection of vehicles is used, factors that relate to human visual response have not been considered further.

The classical image signal-to-noise ratio is defined as

$$(S/N)_I = [2t_i(\mathrm{D}F)(a/A)]^{1/2}(S/N)_V \qquad (12.2)$$

where

t_i = eye integration for a given display brightness (the default value is 0.2 sec),

$\mathrm{D}F$ = video noise bandwidth in Hz (this is normally obtained from the video monitor specifications),

a = area of the detected image,

A = total area of the display,

$(S/N)_V$ = video signal-to-noise ratio = $\mathrm{D}T / NE\mathrm{D}T$, (12.3)

$\mathrm{D}T$ = object-to-background contrast temperature for IR sensors or object-to-background visible contrast for visible spectrum sensors, and

*NE*D*T* = noise-equivalent temperature difference for IR sensors or noise-equivalent visible contrast for visible spectrum sensors.

*NE*D*T* is a function of the spectral band, video noise bandwidth, instantaneous field of view of the sensor, atmospheric and optical transmission coefficients, detector detectivity, and the spectral integral of the derivative of the thermal emittance of the background [14].

Values for the optical and atmospheric transmission coefficients can be estimated (perhaps 0.9 for the optical coefficient and an appropriate value, based on the fog level, for the atmospheric coefficient). Detectivity can be determined from a measurement of the noise equivalent power of the same detector material found in the sensor or video camera. Typical values are found in the literature. The spectral integral of the derivative of the thermal emittance can be estimated from the literature as well. The values for the other parameters needed to calculate the image signal-to-noise ratio (i.e., focal length, noise bandwidth, optical clear aperture size, and instantaneous field of view) can be obtained from the specifications in the manuals that are supplied with the video cameras.

If the values needed to calculate the absolute value of the image signal-to-noise ratio are not readily available, then a relative image signal-to-noise ratio calculation can be used. This involves declaring the video signal-to-noise ratio constant for a given camera and simply evaluating $[2t_i(\mathrm{D}F)(a/A)]^{1/2}$ for each scene or fog condition. This further simplifies to evaluating only the a/A factor. In fact, a method based on this approach was used to analyze the visible, infrared, and millimeter-wave imagery gathered during the project.

12.5 Mechanization of Metrics using Computer Vision

12.5.1 Algorithm Design Objectives

Our goal was to comparatively measure from a digitized video image the amount of information in video images obtained from cameras of different types. We have developed a method of measuring the amount of noise from a camera as well as the amount of information contained in a picture as a vehicle is passing through the scene. The final metric is obtained by dividing the amount of information by the amount of noise. The result is referred to as an Information to Noise Ratio (INR).

The result (INR) is not sensitive to the resolution of the camera or the field of view because the result is normalized to the number of pixels in the image. While it is desirable to be insensitive to the field of view, there are some situations in which the resolution of the camera is a valid factor as well as the INR. This limitation is overcome by calculating a second metric that multiplies the INR by the camera resolution therefore giving weight to the resolution but retaining independence of the camera's field of view. The metric is also insensitive to the type of infrared image being observed. Both black-hot and white- hot infrared images are judged equally with only the magnitude difference in pixel intensity between the background and foreground images taken into consideration. This also allows for a fair comparison between the intensity based infrared images and black and white (intensity based) visible images as the data is in similar format. The color data from the visible cameras can also be incorporated using similar reasoning as discussed below.

This metric has a specific range of applications and distinct limitations. One consideration is that the metric is sensitive to the size of the window draw over the video (marking the area in which to examine) in relation to the size of the vehicles passing through it. The metric is also sensitive to the environment such as the types and colors of the vehicles and the effects of shadows or other changing light conditions.

The solution to the previous two problems is in the use of the program that implements the metric, and the manner in which the video was recorded. Every filming session was performed with two or more cameras filming simultaneously and recorded with identical video time code. This allows for evaluating the exact same frames of video for every camera in any given set. When selecting the window in which to evaluate, extra care must be taken to size the window over the exact same portion of the image for every tape in the set. This is accomplished by stopping each tape on a specific frame and boxing the same vehicle with the same relative size box for each tape in the session. Then, the same frames for each tape are evaluated to assure a minimal amount of environmental influence in the results. The final results are then normalized to a single camera in the set by dividing all results by one camera's result. The final result (the INR) is now a valid comparison of the performance of each camera in the set.

The solution to the previous problems does however introduce another problem. The results of one session are not directly comparable to the results of another. The solution to this problem involves linking the two sets of cameras through a camera common to both sets. If both sets of cameras results are normalized to the same camera, the results from both sets are now directly comparable.

All the images (3-5 μm, 8-12 μm and visible) all contain an intensity component of the image. The visible images also contain a color component. The intensity components are all treated in the same fashion but the color component requires some modifications. Both sets of equations will be covered with the intensity-based version first.

The metric expects two sets of input. The first set is a series of images that contain only pictures of the scene itself; there should be no pictures of any vehicles in these frames. These will be referred to as background images. The second set should contain pictures that contain vehicles. These will be referred to as foreground images. Both sets of images should be over identical portions of the video.

After the images have been selected, the first task is to calculate a single average background image. This is accomplished by averaging each pixel in the image over all the images in the background set.

The equation to calculate the intensity-based background image is

$$BKG[k] = \frac{\sum_{j=1}^{q} B_j[k]}{q} \quad for\ k = 1,...m \tag{12.4}$$

BKG[k] is an array of pixels that forms the single average background image. $B_j[k]$ is the k^{th} pixel of the j^{th} image in the set of background images. Where *m* is the number of pixels in each image and *q* is the total number of background images.

For color images we get three equations, one for each color

$$BKG[k].red = \frac{\sum_{j=1}^{q} B_j[k] \cdot red}{q} \quad for\ k = 1,...m \tag{12.5}$$

$$BKG[k].green = \frac{\sum_{j=1}^{q} B_j[k] \cdot green}{q} \quad for\ k = 1,...m \tag{12.6}$$

$$BKG[k].blue = \frac{\sum_{j=1}^{q} B_j[k] \cdot blue}{q} \quad for\ k = 1,...m \tag{12.7}$$

For the color case each pixel is split into the three component colors and each color component is averaged separately.

At this point BKG contains a single image that is the average background for the area of the image currently being examined.

12.5.2 Background Noise Calculation

The next step is to calculate the amount of noise in the video. This is accomplished by calculating the average RMS noise from each image in the background set.

$$\text{Background Noise} = \sum_{j=1}^{q} \left[\frac{\sum_{k=1}^{m} \left[B_j[k] - BKG[k] \right]^2}{m} \right]^{1/2} \cdot \frac{1}{q \cdot 255} \qquad (12.8)$$

Again, *m* is the number of pixels in each image and *q* is the total number of background images. Each pixel can range in value from 0-255, therefore the final result is divided by 255 to normalize the result to a range of 0.0 to 1.0.

The pixel difference is handled differently for color images. The intensity pixel difference is just based on the one dimensional magnitude difference between the average background and background image pixels. For color, the two pixels are located in a two dimensional color space. This color space is spanned by the red, green and blue axis. The three axis are all 120 degrees apart and exist in a single two dimensional color plane. The pixel difference is measured as the distance between the two pixels on this two dimensional plane.

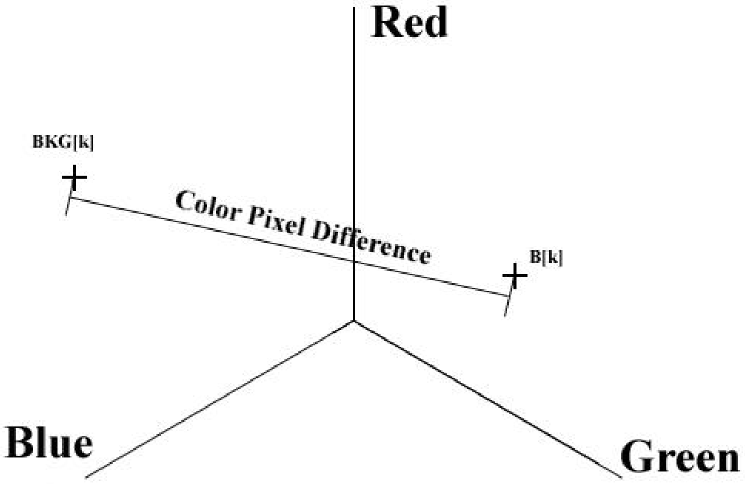

Figure 12.1 Measurement of Color Contrast Information by Magnitude of Vector Difference in Color Phase Plane.

To obtain the color difference, first the difference in each color component is measured:

$$Y_j[k].red = B_j[k].red - BKG_j[k].red \qquad (12.9)$$

$$Y_j[k].green = B_j[k].green - BKG_j[k].green \qquad (12.10)$$

$$Y_j[k].blue = B_j[k].blue - BKG_j[k].blue \qquad (12.11)$$

From the three color components and some trigonometry, the difference is calculated as follows:

$$\begin{aligned} Delta_j[k] = {} & Y_j[k].red^2 + Y_j[k].green^2 + Y_j[k].blue^2 \\ & - Y_j[k].red \cdot Y_j[k].green - Y_j[k].red \cdot Y_j[k].blue - Y_j[k].green \cdot Y_j[k].blue \end{aligned} \qquad (12.12)$$

Once the difference between each pixel is calculated the background noise can be calculated like before:

$$\text{Background Noise} \quad = \sum_{j=1}^{q} \left[\frac{\sum_{k=1}^{m} \left[Delta_j[k] \right]^2}{m} \right]^{1/2} \cdot \frac{1}{q \cdot 255} \tag{12.13}$$

12.5.3 Foreground Information Calculation

The calculations to determine the foreground information content are almost identical to the calculations for noise. For intensity image information content the equation is:

$$\text{Foreground Information} \ = \sum_{j=1}^{q} \left[\frac{\sum_{k=1}^{m} \left[I_j[k] - \text{BKG[k]} \right]^2}{m} \right]^{1/2} \cdot \frac{1}{n \cdot 255} \tag{12.14}$$

Here $I_i[k]$ is the kth pixel of the ith foreground image, and *n* is the total number of foreground images.

The color equations are also nearly identical. The individual color differences are calculated with the following:

$$X_i[k].red = I_i[k].red - BKG_i[k].red \tag{12.15}$$

$$X_i[k].green = I_i[k].green - BKG_i[k].green \tag{12.16}$$

$$X_i[k].blue = I_i[k].blue - BKG_i[k].blue \tag{12.17}$$

The total difference between pixel is then:

$$\begin{aligned} Delta_i[k] = {} & X_i[k].red^2 + X_i[k].green^2 + X_i[k].blue^2 \\ & - X_i[k].red \cdot X_i[k].green - X_i[k].red \cdot X_i[k].blue - X_i[k].green \cdot X_i[k].blue \end{aligned} \tag{12.18}$$

The final foreground information figure then becomes:

$$\text{Foreground information} = \sum_{i=1}^{n} \left[\frac{\sum_{k=1}^{m} \left[Delta_i[k] \right]^2}{m} \right]^{1/2} \cdot \frac{1}{n \cdot 255} \tag{12.19}$$

12.5.4 The Normalized Information-to-Noise Ratio (INR)

Once the background noise and the foreground information are calculated the final INR is calculated:

$$\text{Information/Noise Ratio (INR)} \ = \frac{\text{Foreground Information}}{\text{Background Noise}} \tag{12.20}$$

12.5.5 Factoring in the Value of Color Information for Visible Spectrum Images

Black and White visible cameras as well as all infrared cameras can be easily compared because they all use the same metric. The intensity (or black and white) component of color video can also be directly compared to the infrared cameras. However, we still need a method for determining how the color information from a color visible camera effects the comparison. It is obvious that any additional information contained in the color component of the visible camera should add to the final rating of the visible camera. If the INR of the color component comes out to 1.0 (no color information) then the result should be based entirely off the intensity INR. Careful inspection will reveal that the color and intensity components are orthogonal components that span the two dimensional space of the color image. One axis being intensity the other being color. This infers that the two INR values (intensity and color) should be summed as $\left[I^2 + C^2\right]^{1/2}$. The problem with this equation is that it doesn't take into account that a INR of 1.0 represents an image with no discernable information. If both I and C are 1.0 the final INR should become 1.0. Therefore the equation is modified to be $\left[(I-1)^2 + (C-1)^2\right]^{1/2} + 1$. The one assumption made so far is that the color information content is equally valuable with the intensity information. This is not necessarily true. A modified equation to take this into consideration is $\left[(I-1)^2 + \mathrm{K} \cdot (C-1)^2\right]^{1/2} + 1$. Where the constant K can be used to scale the weight of the color compared to the intensity information. The value of K can not be clearly defined. As a bound, K is a value equal to or greater then 1. In the numerical evaluations made in this report, K was set equal to the conservative value of 1.

An exhaustive review of the literature on human color perception was made to seek out information that could assist in determining K [72, 74, 75, 76, 77]. Although there was abundant information concerning the standards to which human color response was correlated (see Section 12.3), no information was found with which to arrive at a value for K other than unity. This topic certainly appears to be one where further research is needed.

12.5.6 Metric as Applied to Millimeter Wave Images

The TRW multispectral camera was not capable of acquiring video image sequences in real time. Obtaining an image takes approximately 2 minutes. Full-motion images of traffic in motion are not currently possible with this level of technology. Our image information metric is based on measuring the quality of video by analyzing multiple frames of video taken over the same region of the view. With the millimeter images we have only a single frame to develop the background, the background noise and the foreground information figures, therefore a modified metric is needed.

12.5.7 Background Average and Noise

Because there is not a separate image of the object and the environment behind the object, it is impossible to develop an average background image by previous methods. An average background pixel intensity is instead calculated. The user selects a portion of the image where the environment is most similar to the environment behind the object to be inspected. An average pixel value is then calculated from all the pixels within this region. For intensity only, the equation is:

$$BKG = \frac{\sum_{k=1}^{m} B[k]}{m} \tag{12.21}$$

There are three separate equations for color, one for each of the color components of the pixel. Thus

$$BKG.red = \frac{\sum_{k=1}^{m} B[k].red}{m} \quad BKG.green = \frac{\sum_{k=1}^{m} B[k].green}{m} \quad BKG.blue = \frac{\sum_{k=1}^{m} B[k].blue}{m} \tag{12.22}$$

As in the original equations, *m* is the number of pixels in the image.

To calculate the amount of noise the same image is used that was used to calculate the single background pixel. The single pixel is compared to each image pixel and an RMS average noise figure is developed.

For intensity only, the equation is:

$$\text{Background Noise} = \left[\frac{\sum_{I=1}^{m}\left[B[I]-BKG\right]^2}{m}\right]^{1/2} \tag{12.19}$$

The color equations for each color component difference are:

$$Y[I].red = B[I].red - BKG.red \tag{12.23}$$

$$Y[I].green = B[I].green - BKG.green \tag{12.24}$$

$$Y[I].blue = B[I].blue - BKG.blue \tag{12.25}$$

The total pixel difference is calculated as

$$\begin{aligned} Delta[I] &= Y[I].red^2 + Y[I].green^2 + Y[I].blue^2 \\ &\quad - Y[I].red \cdot Y[I].green - Y[I].red \cdot Y[I].blue - Y[I].green \cdot Y[I].blue \end{aligned} \tag{12.26}$$

The background noise can now calculated as before as

$$\text{BackgroundNoise} = \left[\frac{\sum_{I=1}^{m}\left[Delta[I]\right]^2}{m}\right]^{1/2} \tag{12.27}$$

12.5.8 Foreground Information

To calculate the foreground information the user now selects a different portion of the image that contains an object over the normal background of the environment. The same calculation is used again to calculate the foreground information.

For intensity only, the equation is

$$\text{Foreground Information} = \left[\frac{\sum_{I=1}^{m}\left[I[I]-BKG\right]^2}{m}\right]^{1/2} \tag{12.28}$$

The color equations for each color component difference are then

$$X[I].red = B[I].red - BKG.red \tag{12.29}$$

$$X[I].green = B[I].green - BKG.green \tag{12.30}$$

$$X[I].blue = B[I].blue - BKG.blue \tag{12.31}$$

The total pixel difference is calculated as

$$\begin{aligned} Delta[I] = {} & X[I].red^2 + X[I].green^2 + X[I].blue^2 \\ & - X[I].red \cdot X[I].green - X[I].red \cdot X[I].blue - X[I].green \cdot X[I].blue \end{aligned} \tag{12.32}$$

The Foreground information can now be calculated as

$$\text{Foreground Information} = \left[\frac{\sum_{I=1}^{m} \left[Delta[I] \right]^2}{m} \right]^{1/2} \tag{12.33}$$

12.5.9 False-Colored Millimeter-wave Images

Ideally, the application of this metric should not be effected by artificial colorization of the intensity-based images generated by the passive mm-wave camera. Such images have been pre-processed to replace intensity gradients with color gradients in the image. In this sense, additional “information” has been added to the image, although the utility of this information is only to enhance the perception of the otherwise difficult to notice gray-scale changes in the image. In the reduction of our field data from the TRW mm-wave camera, we used intensity-based images only, so that the color perception of the INR contributed nothing. However, in weighting the relative value of color in the INR (described later), we sought a color weighting factor (K) that would yield similar results for either the intensity-based or false colored mm-wave image.

12.5.10 INR Modified for Millimeter-wave Images

Although the method for calculating a INR for millimeter wave images is slightly different then that used for the other types of video, it is directly comparable in both the phenomena it measures and the magnitude of the results it produces. Running the metric designed for the millimeter images on still frames of images from the other camera types does result in figures nearly identical to that obtained with the original metric calculations. The only real ramification is that the margin of variation in readings appears to be greater then that when using the original metric (10% vs. 2%).

Because the millimeter images are not of the same scenes as the images used to analyze the other cameras the results obtained are not directly comparable to those from the other cameras. However the results are good enough to make an estimation of how well millimeter cameras perform when compared to current technology cameras. This is a current limitation of millimeter wave technology and will not be a limitation once the technology reaches the point of being able to obtain images in real time [42, 55].

13 Field Evaluation of Imaging Devices and Systems

A field test plan and procedures were developed to evaluate video imagery from each example of advanced imaging systems described previously. These included nine infrared cameras, one millimeter wave imager, one VNIR-modified CCD camera, and one visible (color) reference camera. We sought to acquire imagery under a wide range of traffic, lighting, and atmospheric conditions. Ideally, test conditions would include combinations of traffic conditions (various levels of service and incidents), atmospheric conditions (clear, convection fog, radiation haze, rain, snow, smoke, dust), lighting conditions (clear mid-day sun, low-incidence angle glare, wet surface glare, snow glare, dusk/dawn low-light, darkness). A field test schedule was developed to implement as many test conditions as possible for the available imaging systems. A detailed listing of the field test procedures and a sample field test itinerary (for one of four field trips conducted) appear in the Appendix.

A test apparatus was constructed comprised of an integrated video data acquisition system with five LTC-synchronized S-VHS video recorders, and a PC-based computer control system. We designed and fabricated a towable mobile surveillance trailer (MST) with a 10-meter collapsible camera tower to provide elevated camera positions in situations when existing platforms such as freeway overcrossings were not available. Figure 13.1 shows the MST deployed during day and night field work in Fresno in December 1994. The MST was used to support both the present project, and our subcontract support work for a PATH project (MOU 83) conducted by Prof. Malik at U.C. Berkeley, on surveillance-based traffic detection.

A high-resolution color visible spectrum camera (Burle TC209) was used to record reference visible video data simultaneously with any or all IR cameras under test. The apparatus supported the simultaneous recording and time-code synchronization of up to four cameras plus the visible reference camera.

Field tests were conducted during the period December 1, 1994 through January 15, 1995. Additional tests followed in March and May, 1995, with the most dense fog encountered in the last tests at Morro Bay, California. The MST was towed to all test sites except Morro Bay using a Ford F350 commercial vehicle, with adequate towing capacity for the trailer and its supplemental ballast weights. The truck with shell also housed the video and related electronic equipment for the field work, including the video data acquisition system and a mobile 110 VAC, 1.5 kW computer-grade DC-AC inverter system for powering all sensitive equipment. This vehicle is shown in Figures 13.2a and b, equipped with a roof-mounted pan-tilt-zoom assembly for three cameras and installed field instrumentation. A 5 kW gasoline generator was used to power non-sensitive field equipment such as the field light arrays and the motor drives for the TRW GOLA unit. A 10,000 lb GVW rental moving van was used to transport the cameras and field apparatus to each test site, which is also shown in Figures 13.1a and b.

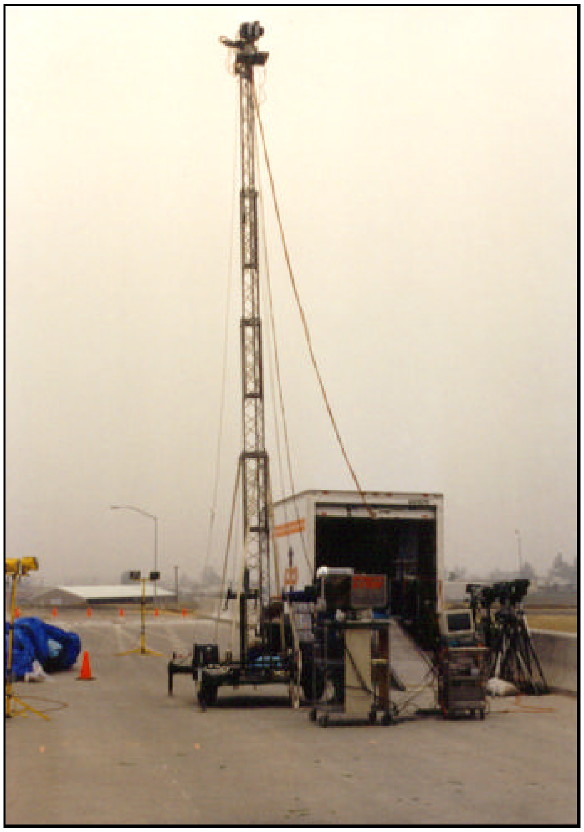

Figure 13.1a Mobile Surveillance Trailer Deployed During Day Field Work, Fresno Area.

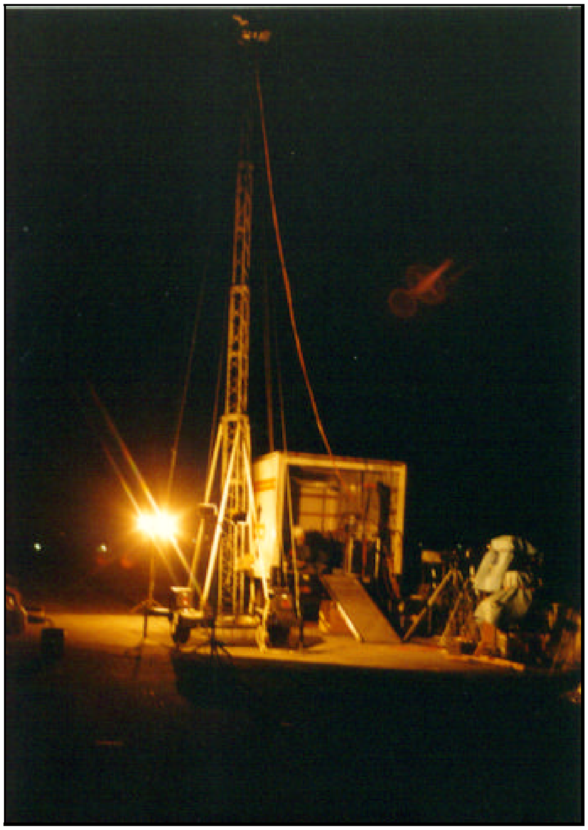

Figure 13.1b Mobile Surveillance Trailer Deployed During Night Field Work, Fresno Area.

Approximately 160 hours of video tape and 100 digitized image files (from the millimeter wave imager) were created at nine field sites in the Los Angeles, Long Beach, Fresno, the Central California Valley, Sierra Nevada Mountains, and San Luis Obispo county coastal areas. Caltrans District 6 permitted us the exclusive use of a new but unopened overcrossing at Fruit Avenue over Hwy 99 in Fresno. The deployment on this overcrossing is shown in Figure 13.3.

Figure 13.2a Exterior View of Mobile Data Collection and Tow Vehicle.

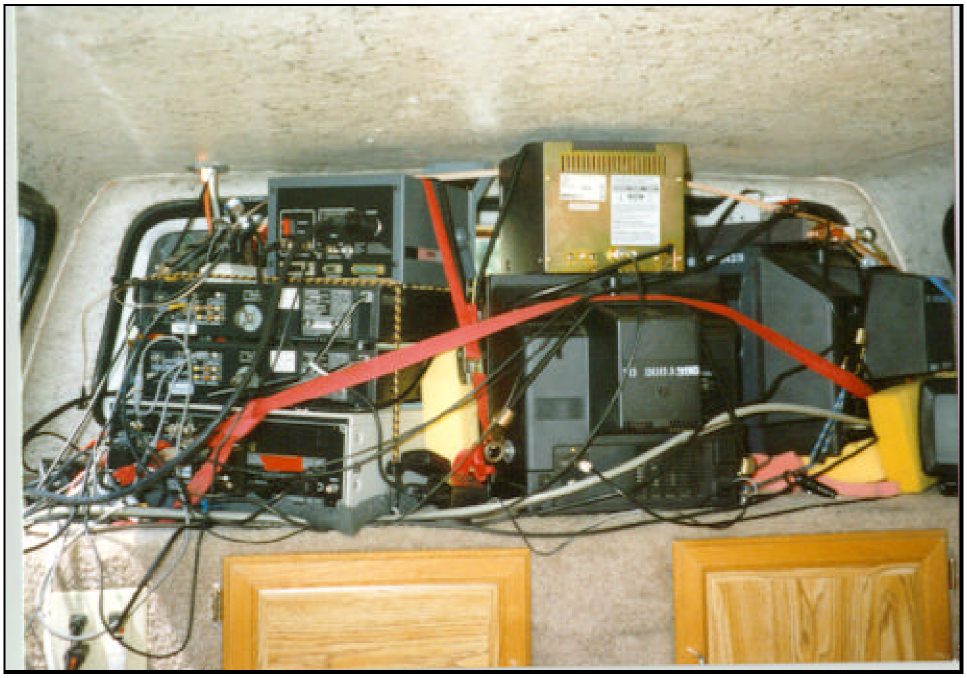

Figure 13.2b Interior View of Mobile Data Collection and Tow Vehicle, Showing Rear Connections To Video and Computer Equipment Accessible from Cab of Vehicle.

Unfortunately, insufficient fog conditions were encountered during the period in which we had nine systems, so that further field work was required in the spring/summer time frame, when reliable coastal fog occurs in the San Luis Obispo area. Additional local tests followed in March and May, 1995, with dense fog encountered in the last tests at Morro Bay, using 3-5 and 8-12 um Inframetrics cameras.

Figure 13.3 Field Test Setup, California Hwy. 99, Fresno.

A typical arrangement of simultaneously tested cameras is shown in Figure 13.4, from field work in the California Central Valley, which is known for seasonal radiative fog.

Figure 13.4 Typical Simultaneous Camera Test Setup, Interstate Hwy 5, near Manteca.

Typical day and night camera views from overcrossing, where most data was acquired, are shown in Figures 13.5a and b.

Figure 13.5a Departing Traffic View, US Hwy 101, Los Angeles County.

Figure 13.5b Approaching Traffic View, US Hwy 101, Los Angeles County.

We attempted to evaluate the performance of infrared imaging systems in snow at Tejachepe, California, elevation approximately 9,000 feet. Of particular interest were the relative susceptibility to glare from snow-covered road surfaces, differences in imaging against a very cold background, and the possibility of reduced dynamic range under the extreme brightness conditions of sunlight on snow. Figure 13.6 shows a resolution test being conducted under snow-glare conditions. For these tests, an infrared resolution chart was designed and fabricated using calibrated progressively closer separations of parallel black metal strips on a highly reflective white background.

Figure 13.6 Resolution Testing Pyroelectric Infrared Camera Under Snow-glare Conditions.

Figure 13.7 Departing Traffic View,Rain Conditions, US 101, Los Angeles County.

The few weatherproof IR cameras (TI NightSight, GEC Marconi, and Agema 1000 with special enclosure) that we had available were tested in rain conditions, from an overcrossing on US Hwy 101 in Los Angeles,. The visible spectrum view from this location is shown in Figure 13.7.

The parallel testing of such a large number of systems on freeways posed a unique set of problems, including direct and indirect safety considerations. Both the size of the operation and the pubic curiosity factor were recognized as potential hazards to drivers and to crew members. Extensive work on road shoulders required particular emphasis on safety, as illustrated in Figure 13.8. Caltrans encroachment

Figure 13.8 Deployment on Road Shoulder, Dusk, US 101, Los Angeles County.

Figure 13.9 View from Inside Truck Next to Camera Test Deployment.

permits were obtained well in advance of field work for every test site. The local office of the California Highway Patrol was alerted of our activities two days in advance of each deployment. Approved safety equipment was used at all times. Whenever the site geometry permitted the locating of the support truck proximate to the camera placements, the recording equipment was operated inside the truck, as shown in Figure 13.9.

The Inframetrics 610 Dual-Band (3-5 um and 8-12 um) IR camera required liquid nitrogen for maintaining the detection elements at operational temperatures. Periodic filling was required approximately every 45 minutes. This innocuous procedure was a particular source of curiosity (and concern in one case) among public observers of our field operations. Transport of liquid nitrogen required special provisions for regulated substances. Figure 13.10 shows the Inframetrics 610 being filled with liquid nitrogen at a field site on US Hwy 101 (Cuesta Grade) near San Luis Obispo, California.

Figure 13.10 Filling the Inframetrics 610 Dual-band IR camera with Liquid Nitrogen.

Due to limited availability of the rented or loaned imaging systems, it was not possible to test all cameras and sensors under all conditions. Although tests were conducted under a range of conditions judged to be typical of light advective and radiation fog, only two infrared cameras (one 3-5 μm and one 8-12 μm) were tested in visibility less than 0.1 km, advection (coastal) fog.

Visibility comparisons were based upon human observation of the recorded images from each camera viewing the same scene, viewed on a reference monitor. When possible, stationary visibility targets (orange traffic cones) were placed in the scene at known distances. However, these were of limited value since the improved imaging capability of IR cameras is related to other factors such as (especially for LWIR) the surface temperature of the targets of interest, in this case automobiles. Subject to the experimental limitations, our field observations appeared to support the trends predicted by MODTRAN for the visible, SWIR, LWIR and 94 GHz millimeter-wave bands. However, lacking precision visibility measurement instruments, it was not possible to quantitatively correlate these conditions with those simulated in our MODTRAN atmospheric models. We also could not clearly test the distinction between advection and radiation fog which showed significant difference in the MODTRAN simulation results.

The 94 GHz Multispectral Scanner (shown in the foreground of Figure 13.3) was capable of producing only still images, of such poor resolution as to be of no surveillance value, despite the exceptional fog-penetrating characteristics of this spectral band. Digitized images are formed on a PC connected to the sensor, using a non-standard image format that can only be interpreted using experimental software provided by TRW. The poor imaging performance is a function of antenna-theoretic considerations[4] as well as the experimental nature of the mechanically-scanned apparatus. The resolutions of monolithic microwave integrated circuit (MMIC)[5] focal plane arrays presently under development are expected to be greatly improved over this single-detector heterodyne system.

Many additional factors were found to influence the quality and information content of the IR, millimeter-wave and visible video images. These factors are related to the fact that the information content of images in the IR and millimeter-wave bands differs significantly from familiar visible perception. As related to traffic surveillance objectives, these factors are discussed later in this report.

14 Analysis of Field Data for Image Information Content

The two metrics previously derived were used to analyze the imagery obtained from the infrared, visible, and millimeter-wave cameras evaluated during this project. The first metric, the normalized information-to-noise ratio (INR), describes the difference in information content of an image that contains a vehicle as compared to an image that consists of only background pixels, relative to the average noise level of the images. This metric is independent of camera resolution since the metric is normalized with respect to the number of pixels contained in the vehicle image. The normalization removes the effect of the differences in the focal lengths of the cameras. The metric is based only on the information content of the image and does not take into account human perception. It simply describes how well a computer can differentiate objects in a camera's field of view from the background.

The second metric accounts for the differing resolution of the cameras. This metric is calculated by multiplying the INR with a factor that is proportional to the number of picture elements (pixels) on a camera's focal plane. This gives appropriate credit to higher resolution cameras, while still removing the effects of any focal length differences between the cameras. The pixel-based factor is calculated by dividing the number of pixels in a camera's focal plane by the number of pixels in the lowest resolution camera used in the project. Thus, the lowest resolution camera has a multiplier of unity and all other cameras a larger multiplier. These values are shown later in Table 14.2.

14.1 Raw data

Table 14.1 contains the raw data from each test, reference numbers, and notes on the test environment and cameras. The color and intensity data obtained from the color camera are shown separately and then totaled. The intensity and color components are weighted equally ($k = 1$) in this table. Raw INR represents the raw information-to-noise ratio that is calculated by dividing the FG (the foreground information content) by the BKG (the background noise). FG and BKG are derived directly from the video image using the equations in Section 12.

Table 14.2 lists all the cameras evaluated during this project. Columns 2 and 3 contain the horizontal and vertical resolutions and Column 4 the total number of pixels on the camera's focal plane. This is a relative measure of the information content of a camera's image assuming the field of view of each camera is identical. The fourth column contains the "resolution multiplier" or pixel-based factor that converts the INR into the second metric that accounts for camera resolution. In this project, the factor is calculated by dividing the number of pixels on a camera's focal plane by the number in the StarSight 8-14 μm camera, namely 15,394.

---

[4] For explanation of beamwidth relationship to antenna configuration see PATH report "Advanced Image Sensing for Roadway Surveillance and Traffic Safety, First Year Progress Report" by this author, December 1995.

[5] Monolithic Microwave Integrated Circuits - gallium arsenide detector arrays operating at 94 GHz.

Table 14.1 Raw data for the traffic conditions encountered during the tests.

ID	Conditions	Session	Raw INR	FG	BKG	Camera
1	Approaching Dusk	1	11.889	0.095	0.008	Cincinnati Elect. 3-5 µm
2	Approaching Dusk	1	4.308	0.106	0.025	FSI Prism 3-5 µm
3	Approaching Dusk	1	6.425	0.067	0.010	TI NightSight 8-14 µm
4	Approaching Dusk	1	8.247	0.086	0.010	AGEMA 8-12 µm
5	Approaching Night	2	1.894	0.169	0.089	StarSight 8-14 µm
6	Approaching Night	2	5.518	0.105	0.019	Inframetrics 600 8-12 µm
7	Approaching Night	2	5.648	0.114	0.020	Marconi 8-14 µm
9	Approaching Night	2	14.350	0.208	0.015	Mitisubishi M300 3-5 µm
8	Approaching Night	2	1.178	0.024	0.020	Inframetrics 600 3-5 µm
10	Departing night	3	17.257	0.105	0.006	Cincinnati Elect. 3-5 µm
11	Departing night	3	6.131	0.112	0.018	FSI Prism 3-5 µm
12	Departing night	3	8.533	0.174	0.020	TI NightSight 8-14 µm
13	Departing night	3	77.810	0.229	0.003	AGEMA 8-12 µm
14	Departing night	4	5.820	0.062	0.011	Infra 600 8-12 µm
15	Departing night	4	6.089	0.185	0.030	Marconi 8-14 µm
16	Departing night	4	14.428	0.284	0.020	Mitisubishi M300 3-5 µm
17	Approaching Day	5	11.526	0.124	0.0101	Cincinnati Elect. 3-5 µm
18	Approaching Day	5	6.569	0.095	0.014	FSI Prism 3-5 µm
19	Approaching Day	5	8.625	0.078	0.009	TI NightSight 8-14 µm
20	Approaching Day	5	9.237	0.090	0.010	AGEMA 8-12 µm
21	Approaching Day	6	11.849	0.194	0.016	Inframetrics 600 8-12 µm
22	Approaching Day	6	5.363	0.085	0.016	Marconi 8-14 µm
23	Approaching Day	6	15.306	0.123	0.008	Mitisubishi M300 3-5 µm
33	Approaching Day	10	14.931	0.083	0.006	Cincinnati Elect. 3-5 µm
34	Approaching Day	10	4.416	0.087	0.020	FSI Prism 3-5 µm
35	Approaching Day	10	6.588	0.120	0.018	TI NightSight 8-14 µm
36	Approaching Day	10	5.619	0.074	0.013	AGEMA 8-12 µm
37	Approaching Day	11	7.693	0.111	0.014	AGEMA 8-12 µm
38	Approaching Day	11	3.391	0.071	0.021	Inframetrics 600 8-12 µm
39	Approaching Day	11	3.886	0.099	0.026	Marconi 8-14 µm
40	Approaching Day	11	10.427	0.119	0.011	Mitisubishi M300 3-5 µm
41	App. Dusk (Intensity)	12	17.385	0.339	0.020	Burle Security Visible
41	App. Dusk (Color)	12	5.757	0.114	0.020	Burle Security Visible
41	App. Dusk (Total)	12	18.061	NA	NA	Burle Security Visible
42	Approaching Dusk	12	4.478	0.067	0.015	AGEMA 8-12 µm
81	App. Dawn Close (Intensity)	25	11.746	0.111	0.009	Burle Security Visible
81	App. Dawn Close (Color)	25	3.928	0.070	0.018	Burle Security Visible

Table 14.1 Raw data for the traffic conditions encountered during the tests (continued).

ID	Conditions	Session	Raw INR	FG	BKG	Camera
81	App. Dawn Close (Total)	25	12.138	NA	NA	Burle Security Visible
83	App. Dawn Close	25	2.243	0.072	0.032	Inframetrics 760 8-12 µm
82	App. Dawn Close	25	19.128	0.132	0.007	Infracam 3-5 µm
81	App. Dawn Far (Intensity)	25	2.355	0.032	0.014	Burle Security Visible
81	App. Dawn Far (Color)	25	1.627	0.039	0.024	Burle Security Visible
81	App. Dawn Far (Total)	25	2.493	NA	NA	Burle Security Visible
83	App. Dawn Far	25	1.136	0.037	0.033	Inframetrics 760 8-12 µm
82	App. Dawn Far	25	1.371	0.007	0.005	Infracam 3-5 µm
81	Dep. Dawn Far (Intensity)	25	2.268	0.017	0.008	Burle Security Visible
81	Dep. Dawn Far (Color)	25	1.105	0.019	0.017	Burle Security Visible
81	Dep. Dawn Far (Total)	25	2.272	NA	NA	Burle Security Visible
83	Dep. Dawn Far	25	1.098	0.036	0.033	Inframetrics 760 8-12 µm
82	Dep. Dawn Far	25	4.768	0.025	0.005	Infracam 3-5 µm
NA	as b/w (the only b/w image)	9DE94R3B	5.089	0.151	0.030	TRW Multispectral Camera
NA	as color	9DE94R3B	1.125	0.026	0.023	TRW Multispectral Camera
NA	as b/w (false colored)	18DE9402	1.346	0.135	0.101	TRW Multispectral Camera
NA	as color	18DE9402	2.753	0.347	0.126	TRW Multispectral Camera
NA	as b/w (false colored)	12DE9401	0.979	0.126	0.128	TRW Multispectral Camera
NA	as color	12DE9401	2.220	0.242	0.109	TRW Multispectral Camera
NA	as b/w (false colored)	18DE9401	1.071	0.148	0.138	TRW Multispectral Camera
NA	as color	18DE9401	2.786	0.352	0.126	TRW Multispectral Camera
NA	as b/w (false colored)	10DEC9401	0.977	0.118	0.121	TRW Multispectral Camera
NA	as color	10DEC9401	2.404	0.291	0.121	TRW Multispectral Camera

NA = not applicable, b/w = black and white

Table 14.2 Individual camera resolution and resolution multipliers.

Camera	Horiz.	Vert.	H x V	Resolution Multiplier
Cincinnati Elect. 3-5 µm	256	256	65536	4.26
FSI Prism 3-5 µm	320	244	78080	5.07
TI NightSight 8-14 µm	320	164	52480	3.41
AGEMA 8-12 µm	320	240	76800	4.99
Burle Security Visible	768	494	379392	24.65
StarSight 8-14 µm (round)	140	140	15394	1.00
Inframetrics 600 8-12 µm	194	240	46560	3.02
Inframetrics 600 3-5 µm	194	240	46560	3.02
M300 3-5 µm	256	256	65536	4.26
Marconi 8-14 µm	200	200	40000	2.60
Inframetrics 760 8-12 µm	194	240	46560	3.02
Infracam 3-5 µm	256	256	65536	4.26
TRW Imager	NA	NA	NA	NA

NA = not applicable

Camera performance is dependent on the lighting and weather conditions. There were three categories of lighting conditions used in these tests, night (very low light), day (good lighting), and dusk/dawn (low-to-medium light). Fog scenes have two designations, close and far. Close data refer to vehicles approximately 60 ft from the camera. These scenes describe the ability of a camera to image a vehicle in close proximity. The far data are divided into two categories, approaching vehicles and departing vehicles. The far approaching vehicles were approximately 1320 ft or ¼ mi from the camera. These data describe the ability of the camera to image a vehicle just as it leaves the fog and becomes visible to the human observer. The far departing vehicles were approximately 660 ft or 1/8 mi from the camera.

In order to compare the performance of each camera to the best performing camera in a session, a ratio is formed by normalizing the raw INR values of the other cameras to that of the best performing camera. If data from more than one session are to be compared, then there must be a common reference camera across all sessions. In this case, a two-step procedure is followed. First the INR values from the sessions are normalized to the INR of the reference camera. Now the normalized INR values can now be treated as a single data set. The second step is to renormalize the combined INR values with respect to the largest normalized value in the combined set. The result is a performance rating as before in terms of a ratio to the best performing camera.

Unfortunately, a common reference camera was not available across all sessions. In these situations, a relationship between two cameras found in a third session was derived to relate the INR values across the sessions. In order to facilitate this procedure, the cameras were grouped into three distinct sets. Figure 14.1 illustrates these relationships. Group A contains the GEC/Marconi Sentry, Insight StarSight, Inframetrics 600, and Mitsubishi M300. Group B contains the Cincinnati Electronics Irris, FSI Prism, Texas Instruments NightSight, and the AGEMA Thermovision 1000. The Group C cameras consist of the Inframetrics Infracam, Inframetrics 760, and the Burle TC291. The AGEMA camera was sometimes deployed with Group A cameras and the Burle camera of Group C. Thus, the AGEMA connected Group B cameras with both Groups A and C and thus established a second-order relationship between Groups A and C through the AGEMA. To obtain the final normalized INR values, the INRs are normalized to that of the reference camera for that group (the shaded camera shown in each group). Then the normalized value is multiplied by the group's reference camera's relative performance compared to the AGEMA. This gives a set of comparable values all normalized to the AGEMA camera. This latter set can now be divided by the high performer in the set to give the desired percent of best rating across all sessions in the set.

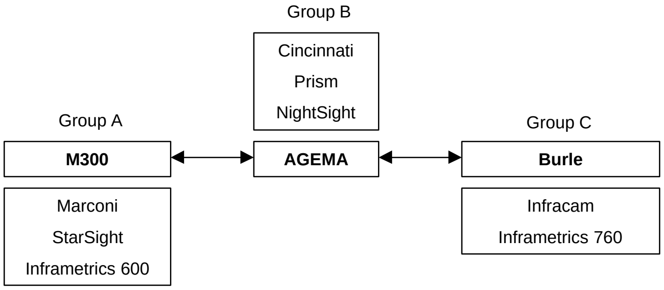

Figure 14.1 Camera relationship tree.

14.2 Night / Approaching

The raw information-to-noise ratio for each camera in the night approaching data set is shown in Table 14.3. The Mitsubishi M300 3-5 µm camera was the highest performing camera of the session and was therefore used as the INR normalization standard.

The 3-5 µm output of the Inframetrics 600 was not functioning properly during the above tests and was not used in any of the future camera data sets. The StarSight was functioning during this test, but performed much worse than the other 8-12 µm cameras. The StartSight stopped functioning soon after this video was taken and its poor performance was likely due to a malfunction. Eliminating the 3-5 µm output of the Inframetrics 600 and the StarSight camera data shows that the 3-5 µm Mitsubishi M300 performed better than the two 8-12 µm cameras.

Table 14.3 Raw and normalized values of camera performance for the night approaching condition.

Session	Raw INR	Camera	INR Normalized to Best in Set	INR x Res. Multiplier	INR-Res. Ratio
2	1.894	StarSight 8-14 µm	0.132	0.132	0.031
2	5.518	Inframetrics 600 8-12 µm	0.384	1.163	0.273
2	5.648	Marconi 8-14 µm	0.394	1.023	0.240
2	14.350	Mitsubishi M300 3-5 µm	1.000	4.257	1.000
2	1.178	Inframetrics 600 3-5 µm	0.082	0.248	0.058

Table 14.4 shows the average performance, by spectral band, for the cameras in Session 2. As in the previous table, the Startsight and Inframetrics 600 results are not included in this result. The 8-12 µm figures are naturally expressed as ratio to best as they are compared with the 3-5 µm results which earned an Average Normalized INR of 1.0.

Table 14.4 INR averages by spectral band for the night approaching condition.

1 INR	3-5 µm	8-12 µm
Average of Normalized INR	1.000	0.389
Average of INR-Res. Ratio	1.000	0.257

Figures 14.1, 14.3, and 14.4 demonstrate why the Mitsubishi M300 scored so well. The higher resolution of the M300 is not the reason for its better performance since the information-to-noise ratio metric is not sensitive to camera resolution. Rather it is the ability of the 3-5 µm cameras to detect the strong front infrared reflection of the vehicle off the pavement that greatly enhances the contrast of the vehicle with the background. The ability of the 3-5 µm camera to detect the light from the vehicle's headlights also adds to the performance of the 3-5 µm cameras over the 8-12 µm cameras. The additional consideration of camera resolution only improved the 3-5 µm relative performance due to the higher resolution of the M300 over the two 8-12 µm cameras.

Figure 14.2 Inframetrics 600 8-12 µm Approaching Night, Session 2.

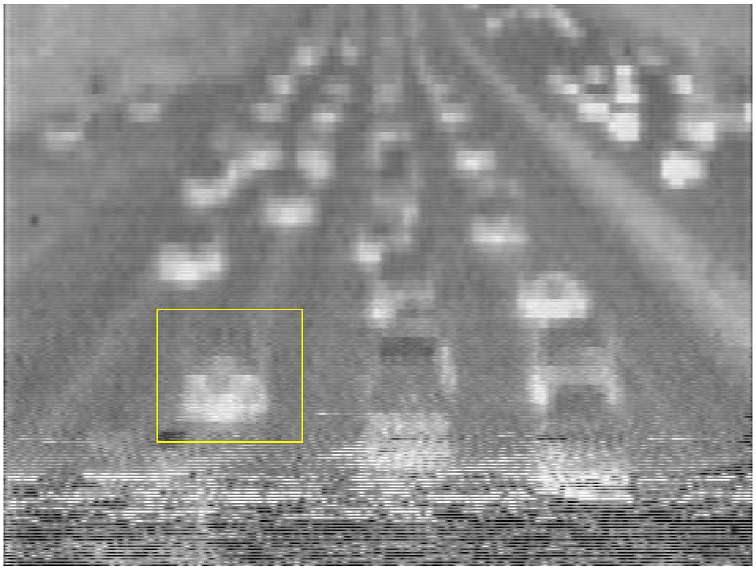

Figure 14.3 GEC/Marconi Sentry 8-12 µm Approaching Night, Session 2.

Figure 14.4 Mitsubishi M300 3-5 µm Approaching Night, Session 2.

14.3 Night / Departing

The information-to-noise ratio data for each camera in the night departing data set is shown in Table 14.5. The Session 3 raw INR values are first normalized with respect to the AGEMA; Session 4 raw INR values are first normalized with respect to the Mitsubishi M300 as shown in the column labeled “Normalized to Best in Session.” The relationship between the M300 and the AGEMA calculated in Session 11 (discussed in the day approaching section below) is used to perform the “Best in Set” calculations that link Sessions 3 and 4 as shown in Column 5. The INR x Res. Multiplier values in Column 6 are computed by multiplying the Column 5 entries by the Resolution Multiplier from Table 14.2. Finally, the INR-Res.

Ratio values in Column 7 are found by dividing the Column 6 entries by the largest entry in Column 6, namely the 4.257 associated with the M300.

Table 14.5 Raw and normalized values of camera performance for the night departing condition.

Session	Raw INR	Camera	INR Normalized to Best in Session	INR Normalized to Best in Set	INR x Res. Multiplier	INR-Res. Ratio
3	17.257	Cincinnati Elect. 3-5 µm	0.222	0.164	0.697	0.163
3	6.131	FSI Prism 3-5 µm	0.079	0.058	0.295	0.069
3	8.533	TI NightSight 8-14 µm	0.110	0.081	0.276	0.065
3	77.810	AGEMA 8-12 µm	1.000	0.738	3.681	0.865
4	5.820	Inframetrics 600 8-12 µm	0.403	0.131	0.397	0.093
4	6.089	Marconi 8-14 µm	0.422	0.157	0.409	0.096
4	14.428	Mitsubishi M300 3-5 µm	1.000	1.000	4.257	1.000

The first row of data in Table 14.6 contains the average of the normalized INRs by spectral band. The second row of data displays the average INR value as a ratio based on the larger of the two values that corresponds to the spectral band averages from Sessions 3 and 4. The third row of data is the average of the INR-Resolution values, while the fourth row of data is the INR-Resolution value expressed as a ratio with respect to the highest spectral band INR-Resolution value.

Table 14.6 INR averages by spectral band for the night departing condition.

2 INR	3-5 µm	8-12 µm
Average of Normalized INR	0.407	0.277
Average INR (ratio wrt best)	1.000	0.680
Average of INR-Res.	0.411	0.280
Average INR-Res. (ratio wrt best)	1.000	0.680

wrt = with respect to

The normalized results for the night departing condition show that the 3-5 µm cameras outperformed the 8-12 µm cameras by 32 percent. However, the performance difference is not as great as in the night approaching case of Table 14.4. In the night departing case, 3-5 µm cameras do not have the advantage of significant ground reflection of the infrared radiation. The prominent feature in the night departing images is the glow from the vehicle exhaust in the 3-5 µm and 8-12 µm images. The high INR of the AGEMA camera is largely due to the very black pavement behind the vehicles (perhaps even saturated at the low end) as contrasted against the bright white exhaust of the vehicle.

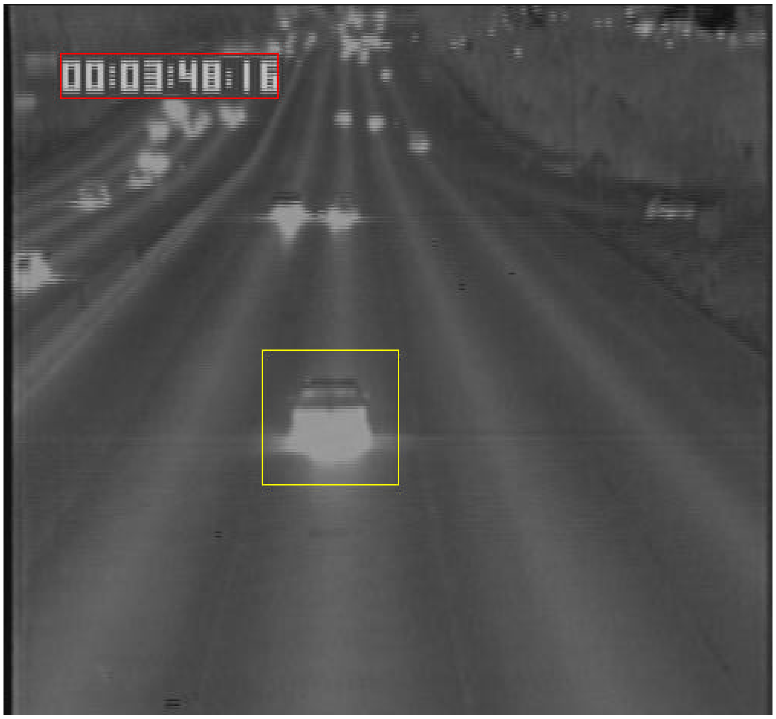

Figure 14.5 Cincinnati Electronics Irris 3-5um Departing Night, Session 3.

Figure 14.6 Agema Thermovision 1000 8-12um Departing Night, Session 3.

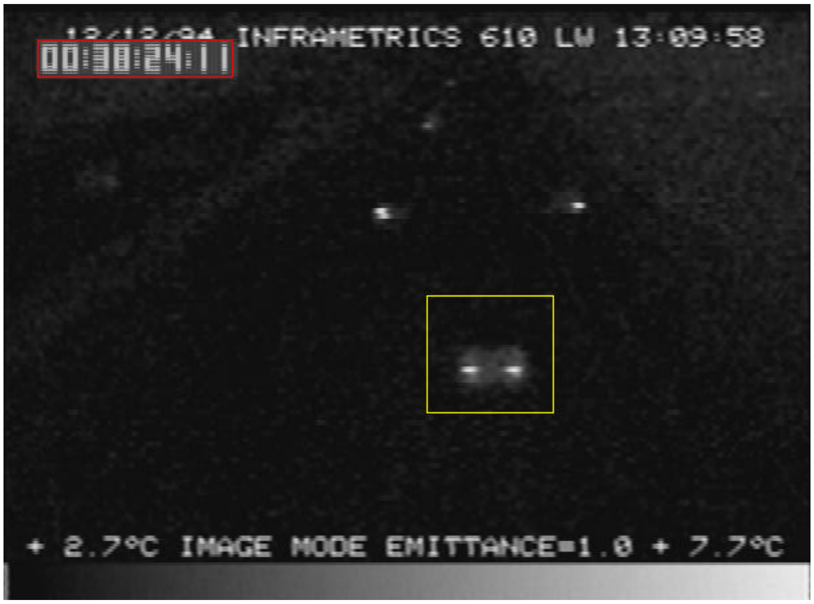

Figure 14.7 Inframetrics 600 8-12um Departing Night, Session 4.

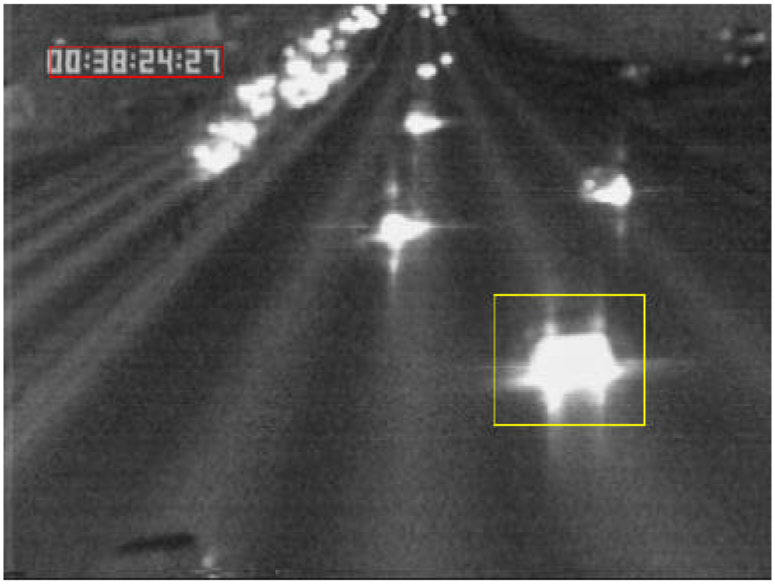

Figure 14.8 Mitsubishi M300 3-5um Departing Night, Session 4.

14.4 Approaching / Day

The information-to-noise ratio data for each camera in the day approaching data set is shown in Table 14.7. The Session 5, 10, and 11 raw INR values are first normalized with respect to the AGEMA; Session 6 raw INR values are first normalized with respect to the Mitsubishi M300 as shown in the column labeled "Normalized to Best in Session." Then the "Normalized to Best in Session" values normalized to the AGEMA are related to the session that was normalized to the M300 using the AGEMA-M300 1:1.355 relationship in Session 11. These results are consequently divided by the highest normalized INR (the Cincinnati Electronics value from Session 10) to obtain the final best in set value.

Table 14.7 Raw and normalized values of camera performance for the day approaching condition.

Session	Raw INR	Camera	Normalized to Best in Session	INR Normalized to Best in Set	INR x Res. Multiplier	INR-Res. Ratio
5	11.526	Cincinnati Elect. 3-5μm	1.248	0.470	2.000	0.470
5	6.569	FSI Prism 3-5μm	0.711	0.268	1.357	0.319
5	8.625	TI NightSight 8-14μm	0.934	0.351	1.198	0.281
5	9.237	AGEMA 8-12μm	1.000	0.376	1.88	0.441
6	11.849	Inframetrics 600 8-12μm	0.774	0.395	1.194	0.280
6	5.363	Marconi 8-14μm	0.350	0.179	0.464	0.109
6	15.306	Mitisubishi M300 3-5μm	1.000	0.510	2.171	0.510
10	14.931	Cincinnati Elect. 3-5μm	2.657	1.000	4.257	1.000
10	4.416	FSI Prism 3-5μm	0.786	0.296	1.500	0.352
10	6.588	TI NightSight 8-14μm	1.173	0.441	1.504	0.353
10	5.619	AGEMA 8-12μm	1.000	0.376	1.877	0.441
11	7.693	AGEMA 8-12μm	1.000	0.376	1.877	0.441
11	3.391	Inframetrics 600 8-12μm	0.441	0.166	0.502	0.118
11	3.886	Marconi 8-14μm	0.505	0.190	0.494	0.116
11	10.427	Mitisubishi M300 3-5μm	1.355	0.510	2.171	0.510

Table 14.8 contains the average of the normalized INRs per camera for the day approaching condition.

Table 14.8 Camera averages for the day approaching condition.

Camera	Average INR[1]	Average INR x Res. Multiplier
Cincinnati Elect. 3-5μm	0.735	0.735
FSI Prism 3-5μm	0.282	0.223
TI NightSight 8-14μm	0.396	0.205
AGEMA 8-12μm	0.376	0.254
Inframetrics 600 8-12 μm	0.280	0.162
Marconi 8-14 μm	0.184	0.076
Mitsubishi M300 3-5μm	0.510	0.347

1. Average of Normalized Best in Set values

Table 14.9 compares the average of the normalized INRs from Table 14.7 and the average INR value as a ratio based on the larger of the two values that corresponds to the 3-5 μm or the 8-12 μm spectral band for the day approaching case. Here the 3-5 μm cameras performed approximately 39 percent better than the 8-12 μm cameras.

Table 14.9 INR averages by spectral band for the day approaching condition.

INR	3-5 μm	8-12 μm
Average of Normalized INR	0.509	0.309
Average INR (ratio wrt best)	1.000	0.608
Average of INR-Res.	0.435	0.183
Average INR-Res. (ratio wrt best)	1.000	0.420

wrt = with respect to

The performance benefit of the 3-5 μm over the 8-12 μm for the day approaching condition is approximately the same as in the night departing sessions summarized in Table 14.6. Adding the resolution multiplier improves the relative performance of the 3-5 μm cameras because of their higher average resolution. The ability of the 3-5 μm cameras to detect the reflection of infrared energy from the front of the vehicle enhances the discrimination of cars from pavement as in the night approaching case. The Table 14.8 day approaching data show an average improvement in the 8-12 μm cameras relative to the 3-5 μm cameras when compared with the night approaching data of Table 14.3. This is contrary to what is expected for two reasons. First, the addition of a large amount of sunlight during the day causes the average level of heat (noise) radiating from all surfaces to rise. Since the 8-12 μm band is more sensitive to thermal energy, one would anticipate this band to be effected more by the added thermal noise. Second, there is higher thermal contrast at night between the hotter signature of a vehicle and the cool road in the 8-12 μm wavelength band. Therefore, the performance of the 8-12 μm cameras should be better than the performance of the 3-5 μm cameras at night, rather than during the day. The reason for this apparent discrepancy is that additional 8-12 μm cameras (AGEMA and the NightSight) were added to the camera set for the day approaching measurements. The added cameras increased the average performance of the 8-12 μm camera set. Using the same three cameras as in the night approaching case (Mitsubishi M300, Inframetrics 600, and the Marconi) gives the averages shown in Table 14.10. Now the 3-5 μm band cameras show about a 54 percent improvement over the 8-12 μm cameras as compared with an approximately 61 percent advantage for the night approaching case shown in Table 14.4.

Table 14.10 INR averages by spectral band for the day approaching condition using only the Mitsubishi M300, Inframetrics 600, and the Marconi data.

INR	**3-5 μm**	**8-12 μm**
Average of Normalized INR	0.510	0.232
Average INR (ratio wrt best)	1.000	0.456
Average of INR-Res.	0.347	0.119
Average INR-Res. (ratio wrt best)	1.000	0.341

wrt = with respect to

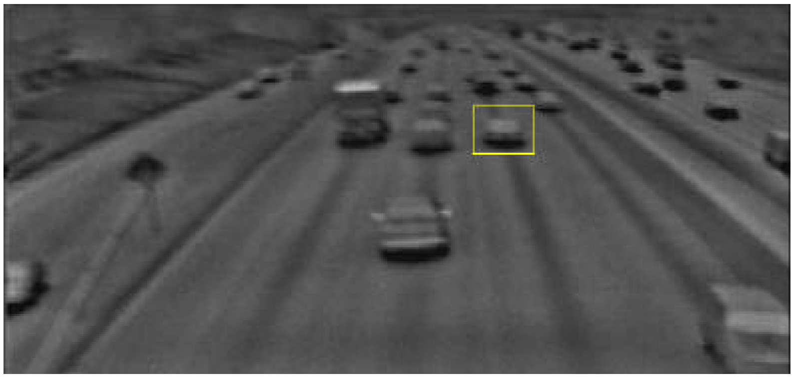

Figure 14.9 T.I. NightSight 8-14 um Approaching Day, Session 5.

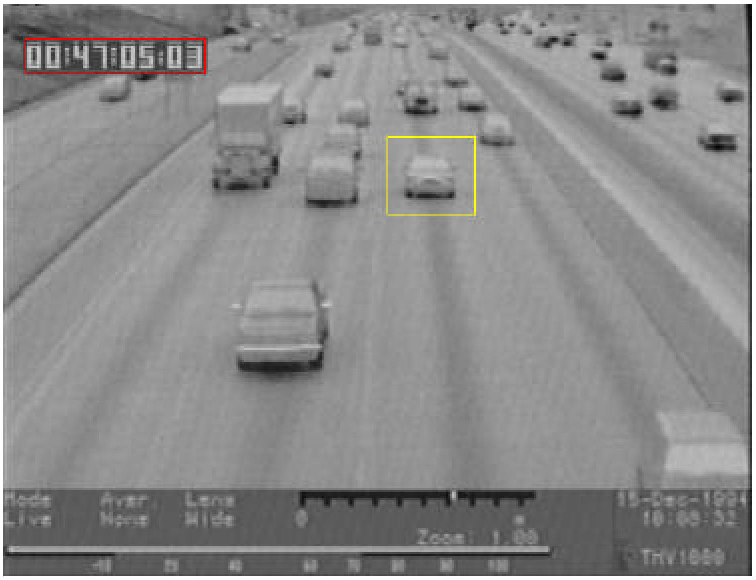

Figure 14.10 Agema Thermovision 1000 8-12 um Approaching Day, Session 5.

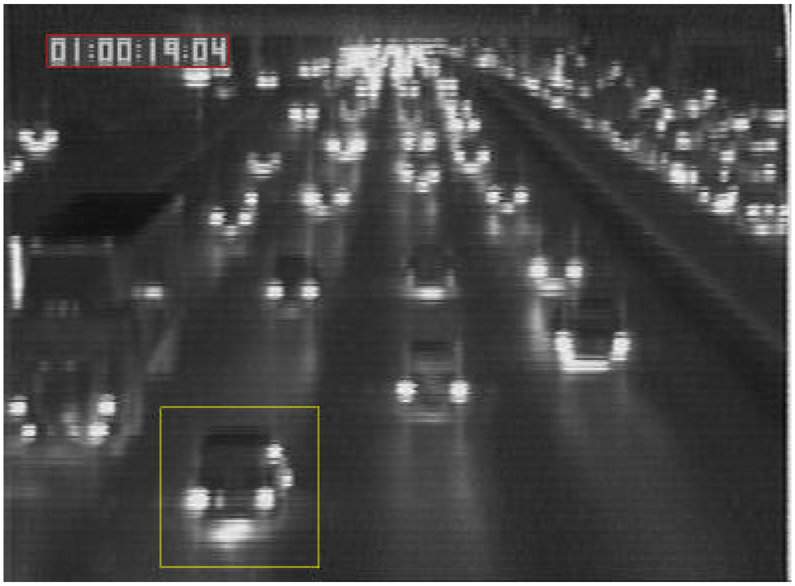

Figure 14.11 Mitsubishi M300 3-5 um Approaching Day, Session 6.

Figure 14.12 Cincinnati Electronics Irris 3-5 um Approaching Day, Session 10.

14.5 Day / Departing

Due to time limitations, we decided to standardize on one condition and selected approaching traffic for that purpose. Therefore, no video was taken in daylight of departing traffic.

14.6 Dawn-Dusk / Approaching

Table 14.11 contains the information-to-noise ratio data for each camera in the dawn/dusk approaching data set. The raw INR values for Sessions 1 and 12 are "Normalized to Best in Session" by dividing them by the corresponding raw value of the AGEMA 8-12 μm camera. Now that the two sessions can be directly compared, the entire set is referenced to the Burle camera to achieve the normalized to best in set values. The INR x Resolution Multiplier and the INR-Resolution Ratio are found as before.

Table 14.11 Raw and normalized values of camera performance for the dawn/dusk approaching condition.

Session	Raw INR	Camera	Normalized to Best in Session	INR Normalized to Best in Set	INR x Res. Multiplier	INR-Res. Ratio
1	11.889	Cincinnati Elect. 3-5μm	1.442	0.357	1.522	0.062
1	4.308	FSI Prism 3-5μm	0.522	0.130	0.657	0.027
1	6.425	TI NightSight 8-14μm	0.779	0.193	0.659	0.027
1	8.247	AGEMA 8-12μm	1.000	0.248	1.237	0.050
12	18.061	Burle Security Visible	4.033	1.000	24.646	1.000
12	4.478	AGEMA 8-12μm	1.000	0.248	1.237	0.050

Table 14.12 contains the average of the normalized best in set INRs and the INR-Resolution Ratio for each camera for the dawn/dusk approaching condition from Sessions 1 and 12.

Table 14.12 Camera performance averages for the dawn/dusk approaching condition.

Camera	**Average INR Normalized to Best in Set**	**INR-Res. Ratio**
Cincinnati Elect. 3-5 μm	0.227	0.062
FSI Prism 3-5 μm	0.082	0.027
TI NightSight 8-14 μm	0.123	0.027
AGEMA 8-12 μm	0.157	0.050
Burle Security Visible	0.635	1.000

Table 14.13 compares the average of the normalized INR values and their ratio values for the 3-5 μm, 8-12 μm, and visible spectral bands for the dawn/dusk approaching case. The Burle Security visible spectrum camera was used as the standard to obtain the INR-Resolution ratio values. The performance of the 3-5 μm and 8-12 μm cameras was approximately the same for the dawn/dusk approaching condition. The visible spectrum camera gave the best performance in this case, outperforming the infrared cameras by a factor of approximately 4.3. Under the dawn/dusk condition, there was enough light for the visible spectrum camera to easily discriminate objects. Furthermore, the lights from the cars were very apparent for the visible camera to detect. These conditions made for ideal visible camera performance as shown in the averaged results. The high resolution of the Burle visible spectrum camera causes the INR-Resolution ratio results to favor the visible spectrum camera very heavily.

Table 14.13 INR averages by spectral band for the dawn/dusk approaching condition.

INR	**3-5 μm**	**8-12 μm**	**Visible**
Average of Normalized INR	0.155	0.140	0.635
Average INR (ratio wrt best)	0.243	0.221	1.000
Average of INR-Res.	0.044	0.042	1.000
Average INR-Res. (ratio wrt best)	0.044	0.042	1.000

wrt = with respect to

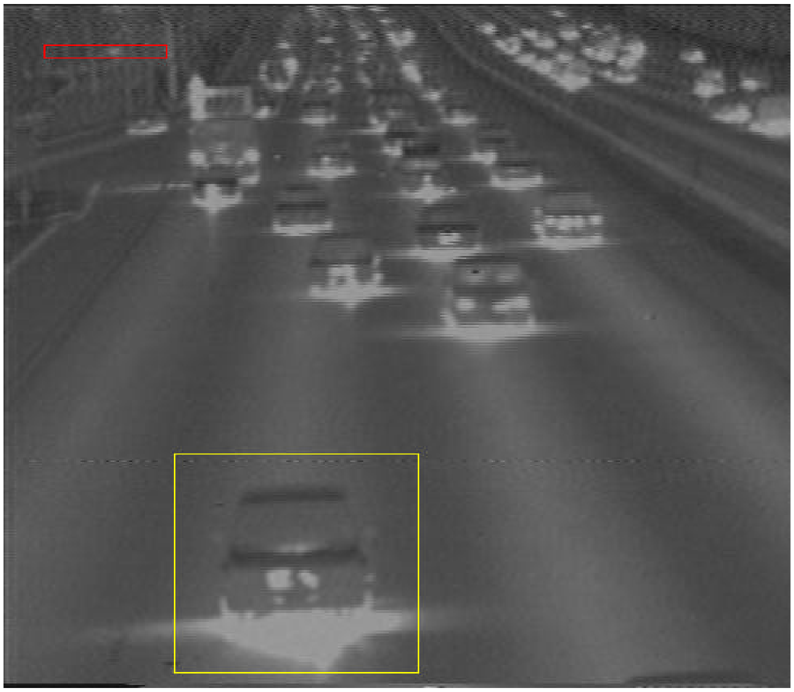

Figure 14.13 Cincinnati Electronics Irris 3-5um Approaching Dusk/Dawn, Session 1.

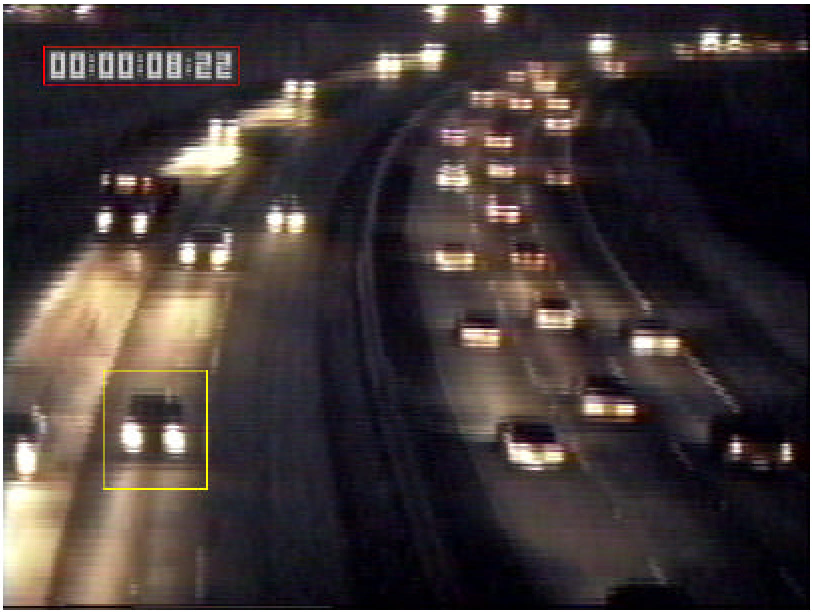

Figure 14.14 Burle Security Visible Approaching Dusk/Dawn, Session 12.

Figure 14.15 AGEMA Thermovision 1000 8-12um Approaching Dusk/Dawn, Session 12.

14.7 Dawn-Dusk / Approaching, Fog, 60 Feet to Vehicle

Table 14.14 contains the information-to-noise ratio data for each camera in the dawn/dusk approaching close to camera in fog data set. The raw INR values are “Normalized to Best in Set” by dividing the raw values by the raw value of the Infracam 3-5 μm camera.

Table 14.14 Raw and normalized values of camera performance for the dawn/dusk approaching close to camera condition in fog.

Session	Raw INR	Camera	Normalized to Best in Set	INR x Res. Multiplier	INR-Res. Ratio
25 Close	12.138	Burle Security Visible	0.635	99.402	1.000
25 Close	2.243	Inframetrics 760 8-12 μm	0.117	2.255	0.023
25 Close	19.128	Infracam 3-5 μm	1.000	27.060	0.272

This is an interesting data set in that a 3-5 μm camera outperforms the visible camera in terms of INR and produces a raw INR that exceeds the values obtained by all other cameras in most of the other sessions. The Infracam is not high resolution, nor is the picture as high in contract as one might expect from the camera that averages the highest overall rating. The Infracam derives its performance from an exceptionally low noise figure. This produces a stable picture and, therefore, makes it easier to select an object moving through the scene. If the scene itself has little noise, almost all pixels that are not part of the background are apportioned to the object. The Burle becomes the highest performer once the additional factor of camera resolution is considered. The high resolution of the Burle camera provides many more pixels of information over a given object.

The fog plays a minor role in this session. The raw INR of the Burle visible camera is lower than the value from Session 12 (18.061) by about 33 percent. The fog had no perceivable effect on the performance of either of the infrared cameras during the "close to camera" evaluation.

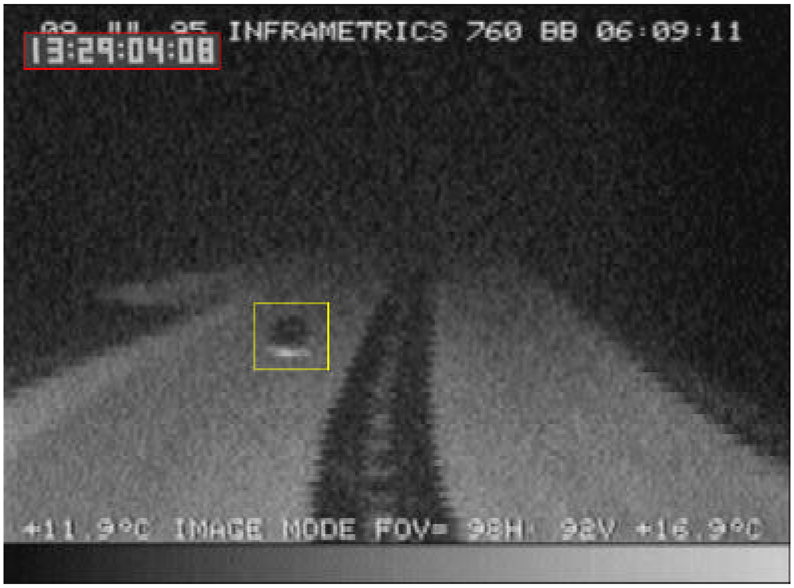

Figure 14.16 Inframetrics 760 8-12um Approaching Dusk/Dawn close in fog, Session 25.

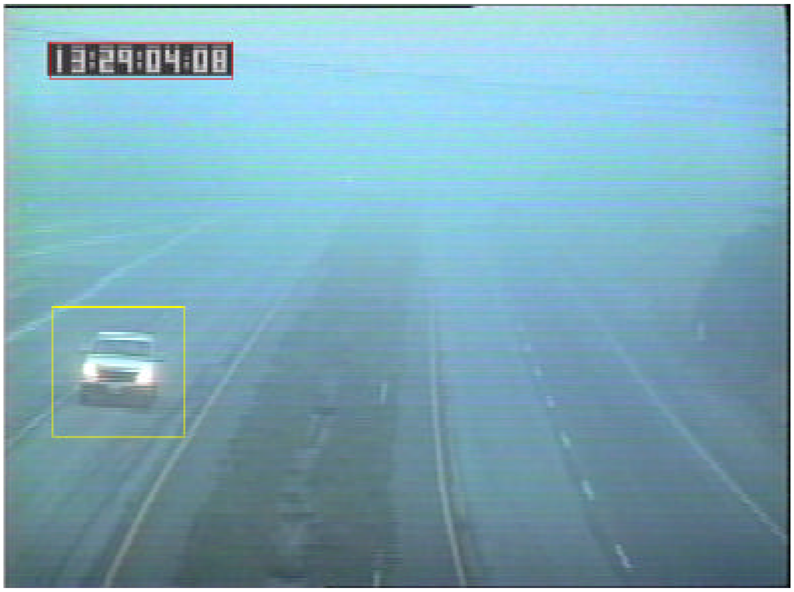

Figure 14.17 Burle Security Visible Approaching Dusk/Dawn Close-in Fog, Session 25.

Figure 14.18 Infracam 3-5um Approaching Dusk/Dawn close in fog, Session 25.

14.8 Dawn-Dusk / Departing, Fog, 1/8 Mile to Vehicle

Table 14.15 contains the information-to-noise ratio data for each camera in the dawn/dusk departing far away from camera in fog data set. The raw INR values are “Normalized to Best in Set” by dividing the raw INR values by the raw value of the Infracam 3-5 μm camera.

Table 14.15 Raw and normalized values of camera performance for the dawn/dusk departing far away from camera condition in fog.

Session	Raw INR	Camera	Normalized to Best in Set	INR x Res. Multiplier	INR-Res. Ratio
25 Far	2.272	Burle Security Visible	0.476	11.743	1.000
25 Far	1.098	Inframetrics 760 8-12 μm	0.230	0.696	0.059
25 Far	4.768	Infracam 3-5 μm	1.000	4.257	0.363

Fog does play a significant role once the window of interest is moved toward vehicles further away. At the 1/8-mile viewing distance used in this session, it is more difficult to distinguish the outline of the vehicles. While the fog effects are more significant here than during the close (60 feet) approaching session, the fog can still not be classified as heavy. This case can at worst be considered medium density fog.

The raw INR of the Burle visible camera is decreased by a factor of approximately 5.3 times as compared to its performance in the close-to-camera fog scene. From these results and the results from the approaching/far fog section below, it is apparent that visible cameras suffer significant performance degradation in fog, while infrared cameras incur less of a penalty. In the images from the 8-12 μm Inframetrics 760, it is difficult to detect a vehicle in a still image. The added motion present in running video adds extra information to aid in vehicle recognition by a human eye. The Infracam is able to track vehicles well into the fog because of its ability to clearly detect the exhaust from the rear of the vehicles. However, the advantage of highest camera resolution gives the Burle the best rating under the conditions reported in Table 14.15.

Figure 14.19 Inframetrics 760 8-12um Departing Dusk/Dawn far in fog, Session 25.

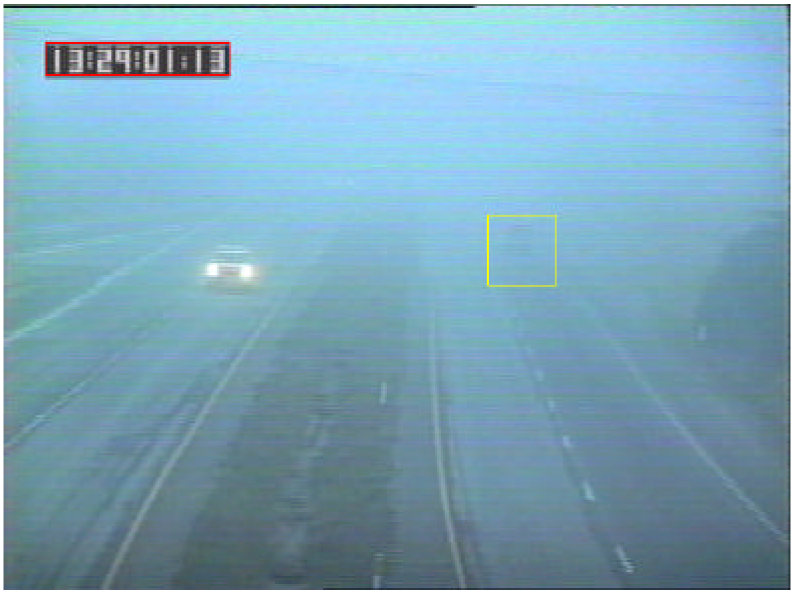

Figure 14.20 Burle Security Visible Departing Dusk/Dawn far in fog, Session 25.

Figure 14.21 Infracam 3-5um Approaching Departing Dusk/Dawn far in fog, Session 25.

14.9 Dawn-Dusk / Approaching, Fog, 1/4 Mile to Vehicle

Table 14.16 contains the information-to-noise ratio data for each camera in the dawn/dusk approaching far away from camera in fog data set. The raw INR values are "Normalized to Best in Set" by dividing the raw values by the raw INR value of the Infracam 3-5 μm camera.

Table 14.16 Raw and normalized values of camera performance for the dawn/dusk approaching far away from camera condition in fog.

Session	Raw INR	Camera	Normalized to Best in Set	INR x Res. Multiplier	INR-Res. Ratio
25 Far	2.493	Burle Security Visible	1.000	99.402	1.000
25 Far	1.136	Inframetrics 760 8-12 μm	0.456	5.559	0.056
25 Far	1.371	Infracam 3-5 μm	0.550	9.440	0.095

In this fog scene, the visible camera performs best followed by the 3-5 μm camera. This scene is differentiated from the other fog scenes in that the only clearly identifiable feature is the vehicle's lights. The visible camera does a good job of detecting the headlights of the oncoming traffic. The 3-5 μm camera is also able to detect the headlights, but at a much attenuated level. Examining the raw INR column reveals ratios slightly larger than 1.0 for both the Infracam and the Inframetrics 760. Therefore, the only camera in the set able to clearly discriminate between vehicles and the fog is the visible camera. The Infracam does, however, detect enough of the headlights to crudely discern an approaching object. As shown in the departing case, when headlights are not present, the 3-5 μm camera outperforms the visible. However, as long as the headlights are available, the visible camera detects vehicles in light-to-medium fog at a greater distance than do the infrared cameras.

Figure 14.22 Inframetrics 760 8-12um Approaching Dusk/Dawn far in fog, Session 25.

Figure 14.23 Burle Security Visible Approaching Dusk/Dawn far in fog, Session 25.

Figure 14.24 Infracam 3-5um Approaching Dusk/Dawn far in fog, Session 25.

14.10 Results Across All Data Sets

Tables 14.17, 14.18, 14.19, and 14.20 contain averages of the performance for each camera across all data sets. The AGEMA camera's performance was used to link the data sets. Sets with fog have been separated from the others in order to obtain a more equal comparison. These summary results may be biased when a camera is used under other environmental conditions as a favorable condition may increase its overall performance, while an unfavorable one may reduce it. In viewing these tables, recall that the visible camera was not used in any night scenes. Assuming poorer performance under low light conditions, its rating may be biased toward the high side due to an absence of night sessions during this project.

The Marconi camera used a PAL-format video signal. Because a PAL video tape recorder (VTR) was not available to play back the Marconi tapes, a NTSC VTR was used out of necessity. The result was video that oscillated from side to side and lost tracking every few seconds. Running the video output through a time-base corrector cleaned up much of the side-to-side movement, but some tracking noise could not be eliminated. While care was taken in selecting stable portions of the video to analyze, the tracking noise that could not be removed likely resulted in a lower score for the Marconi than would be achieved if a PAL VTR was available.

The TRW Multispectral Imager is included in the no-fog camera set. However, the images from this millimeter-wave camera were not equivalent to the images from the other cameras. Images of people were used to analyze the performance of the millimeter-wave camera and, because the images were all still shots, the performance measurements necessarily had to be made differently. This modification to the metric is fully detailed in Section 12. While not directly equivalent, the millimeter-wave results describe how this technology relates to the other types of video. Articles that appeared in *Military and Aerospace Electronics* and *OE Reports* describe an improved version of the Multispectral Imager [42, 55].

Table 14.17 Normalized INR camera performance averages in the absence of fog.

Camera	**Average INR Normalized with respect to AGEMA**	**Average INR Normalized with respect to best performing camera**	**Rank**
Cincinnati Elect. 3-5µm	1.39	0.345	2
FSI Prism 3-5µm	0.525	0.130	7
TI NightSight 8-14µm	0.749	0.186	5
AGEMA 8-12µm	1.000	0.248	4
Burle Security Visible	4.033	1.000	1
StarSight 8-14µm	0.179	0.044	10
Inframetrics 600 8-12µm	0.547	0.136	6
Inframetrics 600 3-5 µm	0.111	0.028	11
Mitsubishi M300 3-5µm	1.355	0.336	3
Marconi 8-14µm	0.432	0.107	8
TRW Mulispectral Imager	0.338	0.084	9

Table 14.18 Normalized INR x resolution multiplier averages in the absence of fog.

Camera	**Average INR Normalized with respect to AGEMA x Resolution Multiplier**	**Average INR Normalized with respect to best performing camera x Resolution Multiplier**	**Rank**
Cincinnati Elect. 3-5 µm	5.927	0.060	2
FSI Prism 3-5 µm	2.661	0.027	5
TI NightSight 8-14 µm	2.553	0.026	6
AGEMA 8-12 µm	4.989	0.050	4
Burle Security Visible	99.402	1.000	1
StarSight 8-14 µm	0.179	0.002	10
Inframetrics 600 8-12 µm	1.655	0.017	7
Inframetrics 600 3-5 µm	0.336	0.003	9
Mitsubishi M300 3-5 µm	5.770	0.058	3
Marconi 8-14 µm	1.122	0.011	8
TRW Mulispectral Imager	NA	NA	NA

NA = not applicable

Table 14.19 Normalized INR camera performance averages in the presence of fog.

Camera	**Average INR Normalized with respect to AGEMA**	**Average INR Normalized with respect to best performing camera**	**Rank**
Burle Security Visible	4.033	0.710	2
Inframetrics 760 8-12 µm	1.511	0.266	3
Infracam 3-5 µm	5.680	1.000	1

Table 14.20 Normalized INR x resolution multiplier averages in the presence of fog.

Camera	**Average INR Normalized with respect to AGEMA x Resolution Multiplier**	**Average INR Normalized with respect to best performing camera x Resolution Multiplier**	**Rank**
Burle Security Visible	99.402	1.000	1
Inframetrics 760 8-12 µm	4.569	0.046	3
Infracam 3-5 µm	24.179	0.243	2

14.11 Results by Spectral Band, All Data Sets

Tables 14.21, 14.22, 14.23, and 14.24 illustrate the average performance of each camera spectral band. In order to weigh each camera's performance equally, the values shown in the table are averages of each camera's average performance over all sessions in which the camera was evaluated. The results have been separated into sets with fog and without fog.

Table 14.21 Normalized INR spectral band performance averages in the absence of fog.

Spectral band & focal plane temperature	Average INR Normalized with respect to AGEMA	Average INR Normalized with respect to best performing camera	Rank
Visible (color & B/W)	4.033	1.00	1
3-5 μm	0.846	0.210	2
8-12 μm cooled	0.774	0.192	3
8-12 μm uncooled	0.453	0.112	5
Millimeter-wave (94 GHz)	0.338	0.084	6
All 8-12 μm	0.581	0.144	4

Table 14.22 Normalized INR x resolution multiplier spectral band performance averages in the absence of fog.

Spectral band & focal plane temperature	Average INR Normalized with respect to AGEMA x Resolution Multiplier	Average INR Normalized with respect to best performing camera x Resolution Multiplier	Rank
Visible (color & B/W)	99.402	1.000	1
3-5 μm	3.674	0.037	2
8-12 μm cooled	3.322	0.033	3
8-12 μm uncooled	1.284	0.013	5
Millimeter-wave (94 GHz)	NA	NA	NA
All 8-12 μm	2.099	0.021	4

NA = not applicable

The AGEMA, Inframetrics 760, and Inframetrics 600 are contained in the set of cooled 8-12 μm cameras. The TI Nightsight, Starsight, and Marconi cameras comprise the set of uncooled 8-12 μm cameras.

Table 14.23 Normalized INR spectral band performance averages in the presence of fog.

Spectral band	Average INR Normalized with respect to AGEMA	Average INR Normalized with respect to best performing camera	Rank
Visible (color & B/W)	4.03	0.710	2
3-5 μm	5.680	1.000	1
8-12 μm cooled	1.511	0.266	3

Table 14.24 Normalized INR x resolution multiplier spectral band performance averages in the presence of fog.

Spectral band	Average INR Normalized with respect to AGEMA x Resolution Multiplier	Average INR Normalized with respect to best performing camera x Resolution Multiplier	Rank
Visible (color & B/W)	99.402	1.000	1
3-5 μm	24.179	0.243	2
8-12 μm cooled	4.569	0.046	3

15 Observations Interpreted in Terms of Traffic Surveillance Requirements

The combination of darkness and fog presents a unique set of visibility problems, not necessarily predicted by atmospheric transmissivity or camera performance metrics. Backscatter of headlight, street light or sunlight illumination appears to be the dominant visibility-reducing factor as fog density increases. Backscatter tends to follow forward diffusion (a transmissivity-reducing factor), so that useful information content in the image declines in an approximate square-law manner with fog density. In view of this, it is not surprising that many of the most serious fog-related traffic accidents have occurred in conditions of darkness or twilight.

The LWIR (8-12 μm infrared) and millimeter wave (94 GHz) bands have some intrinsic advantage under combined conditions of darkness and fog, not only due to improved transmissivity, but since images formed in these bands are based almost exclusively upon the product of the blackbody temperatures and surface emissivities of objects in the field of view. Thus, illumination backscatter is no longer a factor. LWIR images appear to be virtually immune to headlight or streetlight backscatter effects. With shorter wavelengths, specular effects begin to dominate, and this advantage is gradually lost. For example, SWIR daylight images often contain infrared shadows, similar to visible spectrum shadows. The characteristics or VNIR images are so close to those of monochromatic visible spectrum images, that there appears to be no identifiable advantage for traffic monitoring, other than possibly covert surveillance with artificial VNIR illumination. Chromatic (frequency-specific) information is available only in the visible band - made possible by the highly developed human eye. In prior studies, we found that color surveillance information is of significant value in traffic management operations.

The 94 GHz Multispectral Scanner produced only still images of such poor resolution as to be of no surveillance value despite the exceptional fog-penetrating characteristics of this spectral band. The poor performance was attributed to the antenna design and the experimental nature of the mechanically-scanned antenna array.

The camera rankings shown in the tables of the previous section can, in most cases, be anticipated from human observation of the video imagery on a monitor. Our reduced visibility field data was limited to light-radiative fog and light-to-moderate advective fog conditions. We did not acquire enough comparative imagery in dense fog conditions to thoroughly evaluate the relative performance of the different spectral bands under these conditions. For scenes without fog, the visible camera performs best followed by the 3-5 μm cameras. Under conditions of light advective or radiative fog, the 3-5 μm camera performs best, with the visible still giving a strong relative performance. Under all the conditions studied, which did not include heavy fog, the 8-12 μm cameras evaluated provided the poorest vehicle detection (ignoring the millimeter-wave imaging results). Subjectively, we anticipate that this observation would be different in very dense fog, in which extreme dispersion and absorption of radiation from vehicular objects would make detection nearly impossible in all bands except possibly the 8-12 μm band. The relatively poor INR performance of long wave IR we initially found surprising in view of the significantly greater atmospheric transmission of long wave IR radiation compared with visible. On close inspection, however, we observed that the chromatic information available in the visible spectrum, and the headlight information available in the visible, VNIR and 3-5 μm IR bands contributed substantially to detectability of vehicles in fog, more than compensating for the reduced transmissivity in these bands.

We observed that the information content of the infrared images was significantly different than that of the visible spectrum imagery we are accustomed to. These differences generally effected our sense of the quality of the imagery, especially if special consideration is not given to the unique value of the additiaon information available in the IR bands we tested. These differences are llustrated in the three comparitive drawings of Figure 15.1.

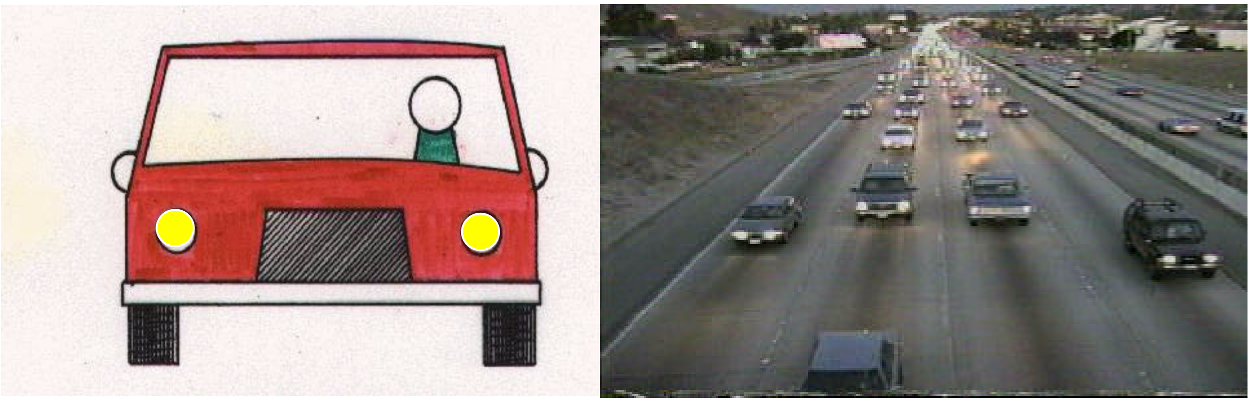

Figure 15.1a Characteristics of Visible or Very Near Infrared Traffic Images.

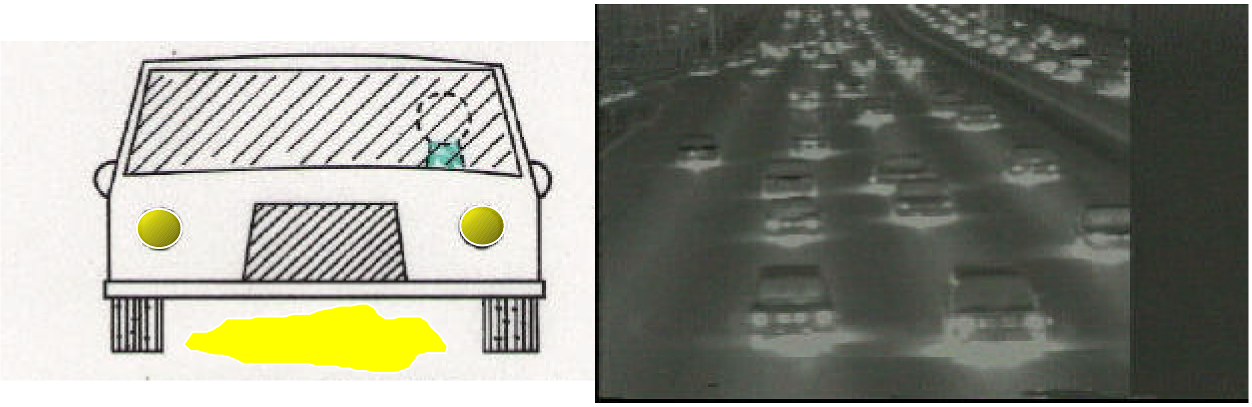

Figure 15.1b Characteristics of 3-5 µm Medium Wavelength Infrared Images.

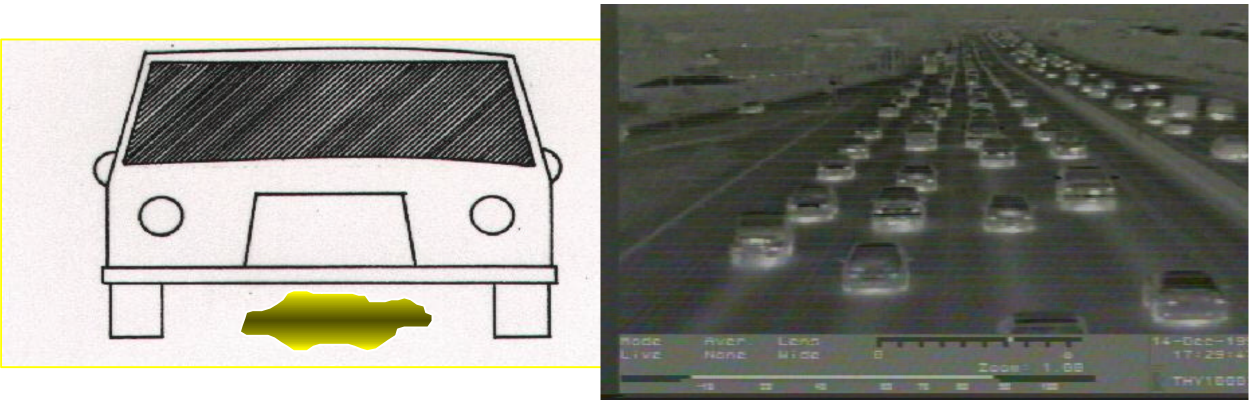

Figure 15.1c Characteristics of 8-12 µm Long Wavelength Infrared Images.

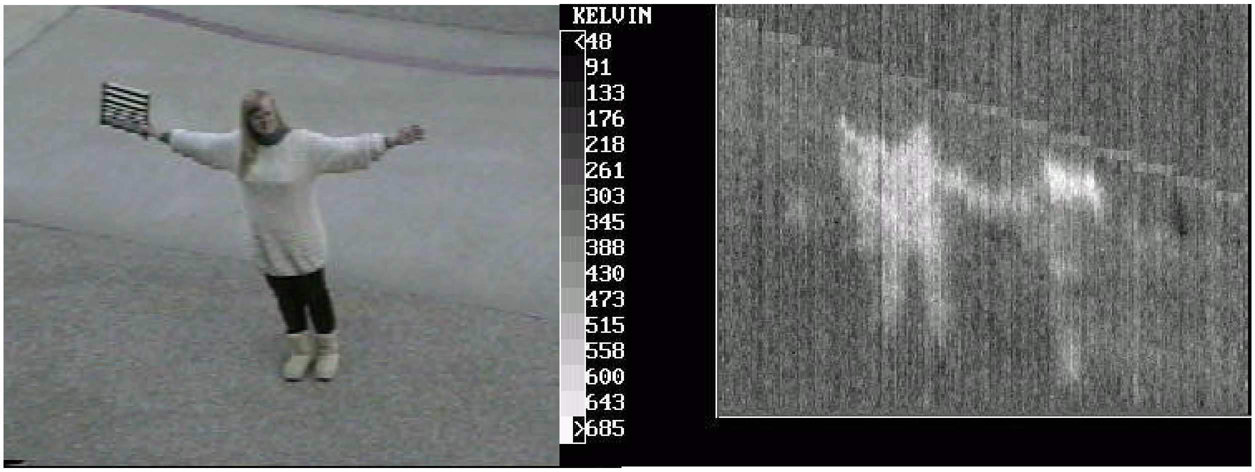

Figure 15.1d Characteristics of 94 GHz Millimeter-Wave Images.

Figure 15.1 Visual image characteristics in the visible and medium- and long-wavelength infrared bands and 94 GHz millimeter-wave band.

Figure 15.1a depicts the visible band, 15.1b the medium-wavelength infrared band, and part 15.1c the long-wavelength infrared band. In the visible spectrum, the windshield is transparent and the image is the customary one observed by the human eye. In the 3-5 μm medium wavelength band, the windshield begins to become opaque and some signature from the hot engine and warm tires becomes apparent. Strongly reflections of IR radiation can be seen on the pavement from the hot engine. Solar IR shadows can be seen. In the 8-12 μm long wavelength band, the windshield is opaque and the engine, tire, and exhaust signatures appear more prominent, as detection in this band responds almost exclusively to black-body heat emissions. Pavement reflections are present, but appear weaker than in the 3-5 μm images. Headlight energy is greatly diminished. Solar IR shadows cannot be seen.

The characteristics of the near infrared wavelength band images are similar to those of monochromatic visible spectrum images. Therefore, there appears to be no discernable advantage to using the near infrared band for traffic monitoring, except perhaps covert surveillance with artificial near infrared illumination. Chromatic (frequency-specific) information is available only in the visible band as interpreted by the human eye. In earlier studies, we found that color surveillance information is of significant value in traffic management operations.

As previously mentioned, the TRW passive 94 GHz Multispectral Scanner provided still images of very poor resolution and noise quality. It was therefore very difficult to separate the intrinsic limitation of imagery in this band from the limitation of the particular example of the technology that we tested. An example of a 94 Ghz image is compared with a visible image of the same scene in Figure 15.1 d. In general, we observed that warm bodies (human, vehicular or other) were detectable against a cold background or sky. Smooth metallic surfaces “reflected” the cold sky, giving them a dark appearance for a white-hot type of image. Resolution is very poor; adequate for crude presence detection, but insufficient for any form of object identification or delineation. Newer versions of the 94 GHz Scanner are expected to yield better imagery by using improved detection arrays that incorporate MMIC focal plane arrays.

Human observations generally correlated with MODTRAN transmissivity predictions for clear weather and fog. We did not deploy precision visibility measurement equipment, which was beyond the scope and funding limits of this study. It was also not possible to differentiate between advective and radiative fog conditions in the field tests.

16 Internet-Accessible Traffic Video Image Database

16.1 Making Our Video Data Available to Other Researchers

In order to assist other researchers whose work may require video imagery of traffic in visible or infrared, we have cataloged the entire library of video tapes created in the course of this study, and created a context-searchable database that is accessible over the World Wide Web. This database includes a 5-second real-time video sample of each entry in the database, covering every traffic scene shot with every type of camera. This database is public-accessible without restriction. A link is also provided for requesting via email the full videotape containing the scene of interest.
Upon approval of PATH, we are willing to provide copies of any video tape in the database upon request. Tapes will be shipped by US mail. A nominal copying fee (TBD) will be charged, via check made out the Transportation Electronics Laboratory, c/o the Electrical Engineering Department, Cal Poly, San Luis Obispo CA 93407.

16.2 Using the Video Database

This section discusses access to and interaction with the video database. It assumes minimal knowledge of the World Wide Web (www) and www browsers such as Netscape, for Internet connection to the Transportation Electronics Laboratory URL.

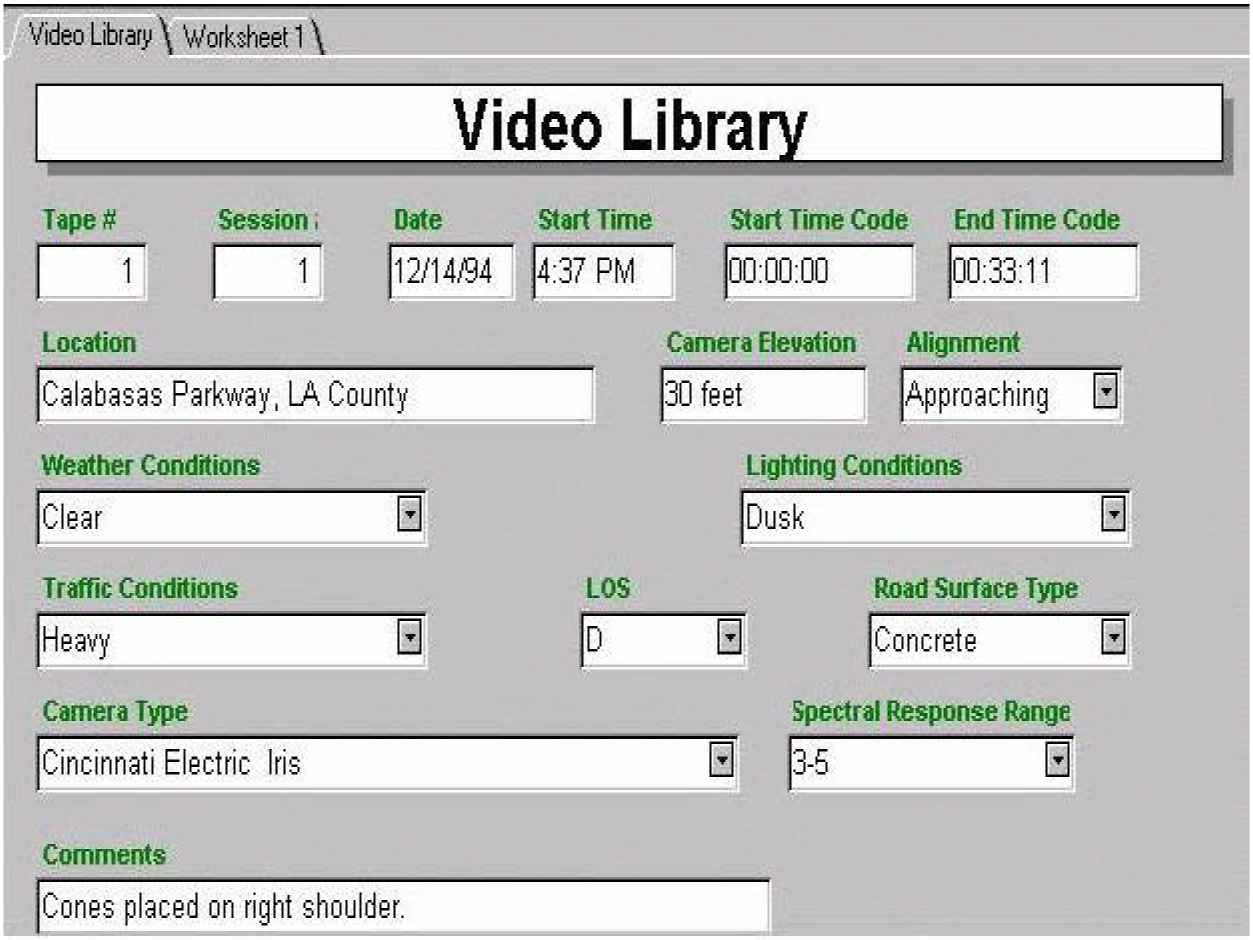

Video Library

Tape #: 1
Session: 1
Date: 12/14/94
Start Time: 4:37 PM
Start Time Code: 00:00:00
End Time Code: 00:33:11
Location: Calabasas Parkway, LA County
Camera Elevation: 30 feet
Alignment: Approaching
Weather Conditions: Clear
Lighting Conditions: Dusk
Traffic Conditions: Heavy
LOS: D
Road Surface Type: Concrete
Camera Type: Cincinnati Electric Iris
Spectral Response Range: 3-5
Comments: Cones placed on right shoulder.

Figure 16.1 Web Site User Interface for Video Database Search Engine.

How to connect to video database over the World Wide Web:

From the main Transportation Electronics Lab web page located at

http://www.ee.calpoly.edu/research/telab/

There is a hyperlink located toward the bottom of the page that activates the database search engine. Simply click this hyperlink to visit the database.

Figure 16.1 shows a typical screen view of the user interface, which is based upon Lotus Approach.

How to use the database:

Once in the database, there are two options: Browse all database entries at once or perform a search through the database. Simply click on the hyperlink which corresponds to the action desired.

There is one entry in the database per session/camera combination. Each entry is separated into the following fields:

1. ID - A unique number for each session/camera combination.
2. Tape # - Multiple sessions were recorded on each video tape. This is why the ID number is used to unambiguously specify each session/camera combination.
3. Alignment - How the cars are aligned relative to the camera. This is either Approaching, Departing, Roaming, or Transverse.
4. Location - Where the session was recorded
5. LOS (Level of Service) - Measure of traffic density
6. Lighting Conditions
7. Weather Conditions
8. Date - The date the tape was filmed
9. Length - The length of the scene
10. Notes - Any notes regarding the scene
11. Camera Model - Which camera was used for that particular entry
12. Session Number - Every scene was recorded with multiple cameras. Each scene has a unique session number
13. Spectral Response - What radiation spectrum the camera used. This is either visible, 3-5 μm, or 8-12 μm.
14. Time of day - Time of day the session was recorded
15. Road Surface - This is concrete for every session currently in the data base
16. Camera Elevation

For each session/camera combination there is a short video clip. To see it, click on the "View Video" button.

Performing a search:

The database search is performed with the following six parameters:

1. Time of Day
2. Traffic Conditions
3. Camera Model
4. Alignment
5. Lighting Conditions
6. Weather Conditions

As many parameters can be set as desired. To have the search ignore a specific perimeter, leave that selection at the default "All". For example, to find all video scenes that use the AGEMA infrared camera, click on the drop down camera menu, and choose the AGEMA camera. All other drop down boxes should contain "All". Clicking the "Search" button will load a page that has every available entry based on the defined search parameters. From this page it is possible to view a short video clip of each session/camera combination encoded for viewing using a public-domain “QuickTime” viewer, which should launch automatically from a web browser upon double licking the link to the video clip.

We are currently in the process of porting the database from Lotus Approach to Microsoft Access. This is required due to compatibility problems with the Windows NT 4.0 Operating System that is now running on the Transportation Electronics Lab web server. The user interface shown in Figure 16.1 will change, but all functionality will be retained.

17 Documentary Video Report

The video technology focus of the project suggests that the written presentation of results might be supplemented by a documentary video production. As and adjunct to this report, a 30-minute documentary video presentation was created which presents all research accomplishments, results, and discussion for viewing on a standard VHS video cassette player. This video report includes a summary of the advantages and limitations of all imaging technologies tested, as well as videotaped sequences from all cameras tested, demonstrating the image type and quality. This videotape presentation was designed to be a multi-media supplement to this report. In addition, a three-minute digitized video “preview” is included on the distribution CD for this report, or is downloadable (along with this document) from the Transportation Electronics Web site at www.ee.calpoly.edu/research/telab. The preview video is playable using the public domain Apple QuickTime video viewer, which runs under all popular web browsers.

18 Overall Conclusions and Recommendations

The ability to detect the formation of traffic patterns which, in conjunction with the reduced visibility, are high-probability accident precursors, requires that the image sensor have improved ability to see flowing traffic through the fog or dust. Other situations in which enhanced imaging methods might be called for are those requiring improved "night vision", specifically the ability to see complete vehicles in darkness, rather than just the headlight spots. Conventional visible-spectrum cameras see only the headlights or tail lights of a vehicle at night. No information is available in the image on the physical shape, size or exact orientation of the vehicle. A pair of head light spots could be created by a 100-foot long tractor-trailer rig, or a compact car. A single headlight could be a motorcycle, or an automobile with only one working headlight.

Headlight information alone is inadequate for assessment of impending traffic hazards, or detection of impaired or otherwise unsafe drivers. Video surveillance or computer image processing for these purposes requires information on the entire shape, type and orientation of the vehicle. Advanced imaging methods such as long wave IR cameras or imaging radar have the capability to see complete objects in the darkness, without the image being "washed out" by the brightness of the headlights. In specialized traffic monitoring situations such as these, advanced technology imaging systems may be required to provide TOC operators with sufficient information to make critical decisions.

IR radiation in either the medium wavelength (3-5 um) or long wavelength (10-12 um) bands has improved ability to penetrate water fog, relative to visible spectrum radiation. This is especially true for the 8-12 um band. The fog characteristics (droplet size distribution and density) have a first order effect on specific visibility results as predicted by computer simulation.

Current low-noise IR imaging technologies, both long and medium wavelength, require cooling systems to maintain the imaging chip at near cryogenic temperatures, typically 77 Kelvin. Two approaches to providing this cooling are in use: cryogenic (usually gaseous or liquid nitrogen) cooling for short-term installations, or closed refrigeration systems, typically using helium as the working fluid, for continuous operation systems. Neither of these systems is intended for the type of 24-hour remote service required in traffic detection. Room temperature infrared imaging technologies are available (pyroelectric and microbolometer) but have reduced performance compared with cooled sensors. The advantage, however, is that cryogenic cooling is not necessary, which translates into significantly lower cost and greater reliability.

In the millimeter range, atmospheric transmissivity is excellent in bands centered about 35, 94, and 140 GHz (and higher frequencies). Best image resolution favors higher frequencies, while solid state amplification and discrimination technologies are practically limited to less than 100 GHz at the present time. These constraints bracket the 94 GHz spectral band, which makes it the frequency of choice for passive radio frequency range imaging. Radiation in the millimeter range is far more effective at penetrating either fog or dust than electro-optical sensors. However, the resolution of the millimeter wave imager we tested was extremely poor. This is an intrinsic limitation of the method, following from the longer bandwidth and practical limitations of reasonably-sized antennas. Creating images at the desired frame rates (e.g., 10 Hz) requires a high azimuth scan rate to cover the region of interest with the narrow beam required for high resolution. Recent developments in microwave integrated circuits offer the potential of lower costs and improved resolution, although image quality and definition will probably never be comparable with that of optical imaging devices.

In the visible range, chromatic (color) information provides some advantage in obscured atmospheric conditions, since color can be used to distinguish vehicles despite considerable diffusion of the scene. Image processing systems can take advantage of color using appropriate image enhancement algorithms.

In the IR range, only room-temperature imaging appears feasible for unattended highway installations. Image information for traffic surveillance applications is, according to our analysis, greater in the 3-5 um IR band, but atmospheric penetration (based upon computer simulation) is superior in the 8-12 um IR band. Room temperature IR cameras are currently being improved, but presently are less sensitive than cooled cameras.

Millimeter wave passive or active imaging has exceptional fog and dust penetrating capabilities. Cost is varied, primarily dependent upon the image scanning method. Real beam phased-array systems are probably most practical for traffic imaging, but are very costly and possibly resolution-limited.

Color cameras might be of some benefit in low-visibility conditions, if image processing algorithms are designed to take advantage of chromatic information in the scene. Computer image enhancement based upon color information is possible.

Slight modifications to existing CCD monochrome video cameras to extend their IR response might provide additional image information in fog or dust conditions at low cost. Their usefulness in this mode is hypothetical at this point.

The intrinsic information content in IR or mm-wave images is substantially different that visible spectrum information. We have observed a number of practical applications. The surface temperature of exposed wheel surfaces on commercial trucks was correlated closely with the recent operation of the service brakes. Lack of brake operation on an individual wheel is indicated a reduced surface temperature compared with adjacent wheels on the same vehicle which with properly operating brakes. The IR image, especially in the 8-12 um band, clear shows relative brake operation for the wheels on one side of a passing truck, in a completely non-evasive manner.

Our evaluation considerations included intrinsic image information content, resolution, atmospheric penetration, and practical deployment considerations. While not a factor of consideration in this technical assessment, we cannot ignore the relative cost of advanced imaging technologies, which greatly exceed the costs of conventional visible-spectrum video cameras. Furthermore, the duration of this study did not permit an experimental assessment of system reliability, serviceability or maintainability.

While offering the potential for improved surveillance capability and enhanced information content, the inferior resolution, loss of chromatic information, inferior reliability (for cooled detectors), and exorbitant cost of most state-of-the-art advanced imagers remain significant obstacles to practical implementation at this time. We conclude that these factors will limit the justification for the deployment of these technologies to situations involving recurrent obscured atmospheric or adverse illumination (e.g., glare) conditions. Exceptions may be found in applications of machine vision, whereby the immunity to shadows and consistent day/night IR image permit more robust image processing algorithms.

There appears to be a limited number of situation for which non-visible spectrum imaging appears to be justified. Based on information-to-noise measurements of a large sample of imaging systems, we conclude that that current infrared and millimeter-wave imaging technologies provide marginal or no net advantage compared with conventional color CCD video cameras for typical surveillance needs. Situations that may warrant the use of IR or millimeter-wave imaging seem to be constrained to the following:

1. Roadway situations characterized by frequent dense fog, smoke or dust, in combination with recurrent hazardous traffic patterns, where surveillance and intervention by TMC personnel could reduce traffic incidents or loss.

2. Situations in which temperature information in the scene is useful, such as for detection of overheated truck brakes or tire for HOV inspection.

3. Machine vision applications in which the shadow and glare rejection features of infrared imaging are required for proper detection or measurement.

It is important to note the immature state of these technologies. Since the present high costs of uncooled LWIR focal plane arrays are primarily related to engineering and process considerations, significant reductions in cost and improvements in performance can reasonably be expected if adequate market potential is perceived by manufacturers. Since the highway surveillance market is potentially significant for these technologies, market volume and cost/performance are interrelated.

19 Uncited Related Literature

Blosseville, J. M. "TITAN, New Traffic measurements by Image Processing." Control, Computers, Communications in Transportation. Pergamon Press, New York, 1990:35-42.

Haralick, R. M. and L. G. Shapiro "Glossary of Computer Vision Terms" Pattern Recognition 24.1 (1991): 69.

Hughes Aircraft Co. "Task D Report for \fIDetection Technology for IVHS\fR, Select and Obtain Vehicle Detectors" DOT/FHWA Contract No. DTFH61-91-C-00076, September 1992.

Judycki, D. C. and R. L. Rupert "Advances in Traffic Control Systems in the United States to Facilitate Urban Mobility." International Conference on Road Traffic Control (3rd : 1990): 163-167.

Keen, K. and N. Hoose "INVAID. Integration of Computer Vision Techniques for Automatic Incident Detection" IEE Colloquium (Digest) 20 (1990): 9/1-9/3.

Kelly, David "Results of a Field Trial of the IMPACTS Image Processing System for Traffic Monitoring." Vehicle Navigation & Information Systems Conference Proceedings. (1991): 151-167.

Lakshmanan, Sridhar, Thomas Meitzler, Euijung Sohn, and Grant Gerhart "Simulation and Comparison of Infra-Red Sensors for Automotive Collision Avoidence" IVHS and Advanced Transportation Systems, SP-1076, SAE International Congress and Exhibition, Feb 27, 1995.

Rourke, A. and M. Bell "Application of Low Cost Image Processing Technology in Transport." World Conference on Transport Research (5th : 1989 : Tokohama-shi, Japan). Transport Policy, Management & Technology Towards 2001. Vol. 2 (1989): 169-183.

"Queue Detection and Congestion Monitoring using Image Processing" Traffic Engineering & Control. 32.9 (1991): 412.

Sethi, Ishwar K. and Wayne L. Brillhart "Traffic Analysis Including Non-conforming Behavior via Image Processing." Vehicle Navigation & Information Systems Conference Proceedings. (1991): 193-201.

Shimizu, K and N. Shigehara "Image Processing System used Cameras for Vehicle Surveillance" IEE Conference Publication

Versavel, J. et al. "Camera and Computer-aided Traffic Sensor." IEE Conference Publication. 299 (1989): 66-70.

Wan, C. L. and K. W. Dickinson "Road Traffic Monitoring using Image Processing : A Survey of Systems, Techniques And Applications." Control, Computers, Communications in Transportation. (1990): 27-34.

Wigan, M. R. "Image Processing Techniques Applied to Road Problems." Journal of Transportation Engineering 118.1 (1992): 62-83.

Yoshino, Kenichi "In-tunnel Traffic Flow Measuring System Using ITV Cameras." Vehicle Navigation & Information Systems Conference Proceedings (1991):311-320.

20 Cited References

---

1. Falcone, Jr., V.J., Abreu, L.W., Shettle, E.P., “Atmospheric attenuation of millimeter and submillimeter waves: models and computer code,” AFGL-TR-79-0253 (AD A084485), Air Force Geophysics Laboratory, Hanscom AFB, MA, October 1979.
2. B. W. Golding, "A Study of the Influence of Terrain on Fog Development," Am. Meteorological Soc., Sept. 1993, pp. 2529-2541.
3. F. D. Shepard, Synthesis of Highway Practice 228: Reduced Visibility Due to Fog on the Highway, Transportation Research Board, National Academy Press, Washington, D.C., 1996.
4. N.L. Ingraham and R.A. Matthews, "A Stable Isotropic Study of Fog: The Point Reyes Peninsula, California, U.S.A.," Chemical Geology (Isotope Geoscience Section), 80, 1990, pp. 281-290.
5. W.R. Juergens, Detectors for Automatic Fog-Warning Signs, Final Research Report CA-DOT-TR-1115-1-73-02, California Department of Transportation, Nov. 1973.
6. G.R. Bemis, K.O. Pinkerman, E.C. Shirley, and J.B. Skog, Detectors for Automatic Fog-Warning Signs, Interim Report CA-DOT-TL-7121-1-73-22, California Department of Transportation, July 1973.
7. B. Waller, “Death in the Fog,” Emergency, June 1991, p. 35.
8. M. Chacanaca, "Horror in the Fog," Emergency, August 1995, pp. 61-65.

9. J.H. Hogema and R. van der Horst, "An Evaluation of the A16 Fog-Signaling System With Respect to Driving Behavior," TRB 76th Annual Meeting, Jan. 12-16, 1997, Washington, D.C., Paper No. 97-0227.

10. M.J. Koornstra, An Analysis of Traffic Safety Effects by Changes in Driving Speeds: A Mathematical-Theoretical Analysis (in Dutch), Inst. For Road Safety Research SWOV, Leidschendam, 1990.

11. K.A. French and E.M. Wilson, "Remote Sensing Rural Road and Travel Conditions," Univ. Of Wyoming, presented at Improving Rural Transportation through Advanced Transportation Technology, Redding, CA, Sept. 28-29, 1992.

12. 1997 TRB Freeway Operations Committee Annual Meeting, Report from FHWA Field Offices, Compiled by Jeff Lindley, U.S. DOT ITS Joint Program Office, Jan. 1997.

13. Fog Detector Warns Drivers, "Front and Center," Weatherwise, Vol. 48, No. 1, Feb-Mar 1995.

14. Klein, L.A., Millimeter-Wave and Infrared Multisensor Design and Signal Processing, Artech House, Norwood, MA, 1997.

15. Hudson, R.D., Infrared System Engineering, John Wiley and Sons, NY, 1969.

16. Wu, Z.S., K.F. Ren, and Y.P. Wang, "10.6 Micron Wave Propagation in Cloud, Fog, and Haze," International Jrnl of Infrared and Millimeter Waves, Vol. II, No. 4, 1990, pp. 499-504.

17. Kneizys, F.X., Shettle, E.P., Gallery, W.O, Chetwynd, Jr., J.H., Abreu, L.W., Selby, J.E.A., Fenn, R.W., and McClatchey, R.A., Atmospheric Transmittance/Radiance: Computer Code: LOWTRAN 5, AFGL-TR-80-0067, AFGL, Hanscom AFB, MA 01731, 1980.

18. Kneizys, F.X., Shettle, E.P., Gallery, W.O, Chetwynd, Jr., J.H., Abreu, L.W., Selby, J.E.A., Clough, S.A., and Fenn, R.W., Atmospheric Transmittance/Radiance: Computer Code LOWTRAN 6, AFGL-TR-83-0187, AFGL, Hanscom AFB, MA 01731, 1983.

19. Kneizys, F.X., Shettle, E.P., Abreu, L.W., Chetwynd, Jr., J.H., Anderson, G.P., Gallery, W.O., Selby, J.E.A., and Clough, S.A., Users Guide to LOWTRAN 7, AFGL-TR-88-0177, AFGL, Hanscom AFB, MA 01731, 1983.

20. Watkins, W.R., Kantrowitz, F.T., and Crow, S.B., “Optical, Infrared, and Millimeter Wave Propagation Engineering,” Proc. SPIE 926, 1988, pp. 69-84.

21. Fenn, R.W., Clough, S.A., Gallery, W.O., Good, R.E., Kneizys, F.X., Mill, J.D., Rothman, L.S., Shettle, E.P. and Volz, F.E., "Optical and Infrared Properties of the Atmosphere," Chapter 18 in Handbook of Geophysics and the Space Environment, Jursa, A.S., Ed., AFGL-TR-85-0315 (AD A167000), USAF. Geophysics Laboratory, Hascom AFB, MA, 1985.

22. Berk, A., Bernstein, L.S., and Robertson, D.C., MODTRAN: A Moderate Resolution Model for LOWTRAN 7, GL-TR-89-0122, USAF Geophysics Laboratory, Hascom AFB, MA, 1989.

23. Rothman, L.S., et al., "The HITRAN Molecular Database: Editions of 1991 and 1992," J. Quant. Spectrosc. Radiat. Transfer, Vol. 48, 1992, p. 469.

24. Anderson, G.P., Chetwynd, J.H., Theriault, J.-M., Acharya, P., Berk, A, Robertson, D.C., Kneizys, F.X., Hoke, M.L., Abreu, L.W., and Shettle, E.P., "MODTRAN 2: Suitability for Remote Sensing," SPIE Vol. 1968: Atmospheric Propagation and Remote Sensing II, 1993, pp. 514-525.

25. Chetwynd, J.H., Wang, J., and Anderson, G.P., "FASCODE: An Update and Applications in Atmospheric Remote Sensing," SPIE Vol. 2266, 1994, pp. 613-623.

26. Wang, J., Anderson, G.P., Revercomb, H.E., and Knuteson, R.O., "Validation of FASCODE 3 and MODTRAN 3: Comparison of Model Calculations with Ground-Based and Airborne Interferometer Observations Under Clear-Sky Conditions," Applied Optics, Vol. 35, No. 30, Oct. 1996, pp. 6028-6040.

---

27. Shirkey, R.C., "Effects of atmospheric and man-made obscurants on visual contrast," SPIE Vol. 305 Atmospheric Effects on Systems Performance, 1981, pp. 37-44.
28. Shirkey, R.C., Duncan, L.D., and Niles, F.E., EOSAEL 87, Vol. 1, Executive Summary, Report TR-0221-1, U.S. Army Laboratory Command, Atmospheric Sciences Laboratory, White Sands Missile Range, NM 88002-5501, Oct. 1987.
29. Smoke and Natural Aerosol Parameters (SNAP) Manual, Joint Technical Coordinating Group for Munitions Effectiveness, Smoke and Aerosol Working Group, Report 61, JTCG/ME-85-2, April 26, 1985.
30. MacCarley, C.A., "Advanced Imaging Techniques for Traffic Surveillance and Hazard Detection," Intellimotion, Vol. 6, No. 2, 1997, pp. 6-9.
31. MacCarley, C.A., "Evaluation of Closed-Circuit Television Technology for Application in Highway Operation," TR 91-4, Final Report, Rev. 2, California Polytechnic University at San Luis Obispo, CA, June 30, 1992.
32. Benson, Blair K. ed., Television Engineering Handbook, McGraw Hill, New York, 1986.
33. Incident Management: Challenges, Strategies, and Solutions for Advancing Safety and Roadway Efficiency, Executive Summary, Prepared by ATA Foundation for National Incident Management Coalition in association with Cambridge Systematics, Jan. 1997.
34. 1997 Freeway Operations Committee (A3A09) Annual Meeting, TRB, Washington, D.C., Jan. 1997.
35. Reports from June 1997 Freeway Operations Committee (A3A09) Meeting, June 1997.
36. Pinson, L.J., Electro-Optics, Ne3w York, NY, John Wiley & Sons, 1985.
37. Stahl, K.J., “IR-detectors: State-of-the-art, Future trends,” Photonics Spectra, Sept. 1989, pp. 95-98.
38. J. Kreider, P. Howard, C. Li, and T. Fitzgibbons, "Uncooled infrared arrays sense image scenes," Laser Focus World, Aug. 1997, pp. 139-150.
39. Crane, R.K., “Prediction of the Effects of Rain on Satellite Communication Systems,” Proc. IEEE, Vol. 65, 1977, pp. 456-474.
40. Ulaby, F.T., Moore, R.K., and Fung, A.K., Microwave Remote Sensing Active and Passive, Vol. 1: Microwave Remote Sensing Fundamentals and Radiometry, Artech House, Norwood, MA, 1981.
41. MacCarley, C. Arthur, Study of Advanced Image Sensing Methods for Traffic Surveillance and Hazard Detection: First Year Progress Report, MOU 114, California PATH Reports to Caltrans 97-C20, April 1997.
42. McHale, J., “TRW develops weather-piercing camera,” Military & Aerospace Electronics, July 1997, Vol. 8, No. 7, p.1.
43. Bohlander, R.A., McMillan, R.W., Patterson, E.M., Clifford, S.F., Hill, R.J., Priestley, J.T. and Schoenfeld, W.P., “Fluctuations in Millimeter-Wave Signals Propagated Through Inclement Weather,” IEEE Trans. on Geos. and Remote Sensing, Vol. 26, No. 3, May 1988, pp. 343-354.
44. Wallace, H. Bruce, “Millimeter-Wave Propagation Measurements at the Ballistic Research Laboratory,” IEEE Trans. on Geos. and Remote Sensing, Vol. 26, No. 3, May 1988, pp. 253-258.
45. Atlas, D., "Advances in Radar Meteorology," in Advances in Geophysics, Vol. 10, Academic Press, NY, 1964, pp. 317-478.
46. Nemarich, J., Wellman, R.J., and Lacombe, J., "Backscatter and attenuation by falling snow and rain at 96, 140, and 225 GHz," IEEE Trans. on Geos. and Remote Sensing, GE-26(3), 319-329 (1988).

47. Goldstein, H., "Attenuation by Condensed Water," Chapter 8 in Propagation of Short Radio Waves, Editor: Kerr, D.E., McGraw-Hill, NY, 1951.

48. Crane, R.K., Microwave Scattering Parameters for New England Rain, Technical Report 426, Lincoln Laboratory, MIT, Oct. 3, 1966.

49. Bogush, Jr., A.J., Radar and the Atmosphere, Artech House, Norwood, MA, 1989.

50. Crane, R.K., “Prediction of Attenuation by Rain,” IEEE Trans. on Comm., Vol. COM-28, No. 9, Sept. 1980, pp. 1717-1733.

51. Falcone, Jr., V.J., and Abreu, L.W., "Atmospheric Attenuation of Millimeter and Submillimeter Waves," IEEE EASCON-79 Conference Record, Vol. 1, pp. 36-41 and Millimeter Wave Radar, Johnston, S.L., Editor, Artech House, Norwood, MA, 1980.

52. Richard, V.W., Kammerer, J.E., and Reitz, R.G., “140 GHz Attenuation and Optical Visibility Measurements of Fog, Rain, and Snow,” ARBRL-MR-2800, 1977.

53. Richer, K.A., "Environmental Effects on Radar and Radiometric Systems at Millimeter Wavelengths," A72-15610, Proc. Symposium on Submillimeter Waves, Polytechnic Institute of Brooklyn, March 31-April 2, 1970, pp. 533-543.

54. C.V. Gilnes, "Synthetic Vision Will Let Pilots See Through Precipitation," Professional Pilot, Aug. 1990, Vol. 24, No. 8, pp. 62-67.

55. Carts-Powell, Y., “Passive millimeter wave imaging growing fast,” OE Reports, March 1997, p. 2.

56. Johnson, J., "Analysis of Image Forming Systems," Image Intensifier Symposium, Fort Belvoir, VA, Report AD-220160, Oct. 1958, pp. 249-273.

57. Johnson, J. and Lawson, W. “Performance Modeling Methods and Problems,” Proc. IRIS Imaging Systems Group, Jan. 1974.

58. Shumaker, D., “Target Detection and Recognition Revisited,” Technote 95-03, Spectral Reflections, Infrared Information Analysis Center, ERIM, Infrared Information Analysis Center, Ann Arbor, MI, 1995.

59. Shumaker, D.L., Wood, J.T., and Thacker, C.R., Infrared Imaging Systems Analysis, ERIM, Infrared Information Analysis Center, Ann Arbor, MI, 1993.

60. Rosell, F.A. and Willson, R.H., "Recent Psychophysical Experiments and the Display Signal-to-Noise Ratio Concept," Chapter 5 in Perception of Displayed Information, Ed.: Biberman, L.M., Plenum Press, NY, 1973.

61. Schmieder, D.E. and Weathersby, M.R., "Detection Performance in Clutter With Variable Resolution," IEEE Vol. AES-19, No. 4, Jul. 1983, pp. 622-630.

62. Gordon, G.A., R.L. Hartman, and P.W. Kruse, "Imaging-Mode Operation of Active NMMW Systems, " Chapter 7 in Infrared and Millimeter Waves, Vol. 4: Millimeter Systems, Ed.: Button, K.J. and Wiltse, J.C., Academic Press, NY, 1981.

63. Scott, L. and Conduff, L., "CNVEO Advanced FLIR Systems Performance Model," SPIE Vol. 1309, Paper 17, April 1990.

64. Kennedy, H.V., "Modeling Second Generation Thermal Imaging Sensors," SPIE Vol. 1309, Paper 1, April 1990.

65. Kruse, P.W., McGlauchlin, and McQuistan, R.B., Elements of Infrared Technology, John Wiley and Sons, 1962.

66. Kneizys, F.X., Shettle, E.P., Abreu, L.W., Chetwynd, Jr., J.H., Anderson, G.P., Gallery, W.O., Selby, J.E.A., and Clough, S.A., Users Guide to LOWTRAN 7, AFGL-TR-88-0177, AFGL, Hanscom AFB, MA 01731, 1983.

---

67. Boreux, J-J and L. Duckstein, "A Fuzzy Approach to the Definition of Standardized Visibility in Fog," Applied Mathematics and Computation, 61, 1994, pp. 287-299.

68. Weichel, H., Laser Beam Propagation in the Atmosphere, Vol. TT3, SPIE Optical Engineering Press, Bellingham, WA, 1990.

69. LaRocca, A.J., "Methods of Calculating Atmospheric Transmittance and Radiance in the Infrared," Proc. of the IEEE, Vol. 63, No. 1, Jan. 1975, pp. 75-94.

70. Shumaker, D., Wood, J.T., and Thacker, C.R., "Infrared Imaging Systems Analysis," ERIM, Ann Arbor, MI, Infrared Information Analysis Center, 1993.

71. Lloyd, J.M., Thermal Imaging Systems, Plenum Press, New York, 1982.

72. Post, D.L., “Color and human-computer interaction,” Chap. 25 in Handbook of Human-Computer Interaction, 2nd Edition, M. Helander, T.K. Landauer, and P. Prabhu, Editors, Elsevier Science B.V., Amsterdam, 1997.

73. Biberman, L.M. (Ed.), Perception of Displayed Information, Plenum Press, New York, 1973.

74. Snyder, H.L.. and L.J. Trejo, “Research methods,” Chap. 2.1 in Color in Electronic Displays, H. Widdel and D.L. Post, Editors, Plenum Press, New York, 1992.

75. Travis, D., Effective Color Displays: Theory and Practice, Academic Press, London, 1991.

76. Mullen, K.T. and F.A.A. Kingdom, “Colour Contrast in Form Perception,” Chap. 12 in The Perception of Colour, Vol. 6: Vision and Visual Disfunction, P. Gouras, Editor, Macmillan Press, London, 1991.

77. Jacobs, G.H., Comparative Color Vision, Academic Press, New York, 1981.